A Study of Planetary Nebulae Possessing Binary Central Stars

A thesis submitted to The University of Manchester for the degree of
Doctor of Philosophy
in the Faculty of Engineering and Physical Sciences

2014

Amy A. Tyndall
Jodrell Bank Centre for Astrophysics
School of Physics and Astronomy

“All truths are easy to understand once they are discovered; the point is to discover them.”

Galileo Galilei (1564–1642)

Contents

Estimated word count: 49000

List of Figures

List of Tables

Abstract

Thesis submitted by Amy A. Tyndall for the Degree of Doctor of Philosophy at The University of Manchester and entitled: ‘A Study of Planetary Nebulae Possessing Binary Central Stars’, January 2014.

In this thesis, detailed studies of three different types of binary central stars within planetary nebulae (bCSPNe) are presented, with the aim of investigating the effects such a range of binary systems has on the morphology and kinematics of the surrounding nebulae, as well as discussing what the implication is for the interaction between the stars themselves. A close binary, an intermediate period binary, and a compact binary system are examined.

The close binary PN HaTr 4 is the first system to be studied via detailed spatio-kinematical analysis and modelling, and it is one of few known to contain a post-common envelope (CE) central star system. CE evolution is believed to play an important role in the shaping of PNe, but the exact nature of this role is yet to be understood. High spatial and spectral resolution spectroscopy is presented alongside deep narrow-band imagery to derive the three-dimensional morphology of HaTr 4. The nebula is found to display an extended ovoid morphology with an enhanced equatorial region consistent with a toroidal waist - a feature believed to be typical amongst PNe with post-CE central stars. The nebular symmetry axis is found to lie perpendicular to the orbital plane of the central binary, concordant with the idea that the formation and evolution of HaTr 4 has been strongly influenced by its central binary.

Next, PN LoTr 1 is studied using a combination of spectra and photometry, and is thought to contain an intermediate-period binary central star system (P = 100–1500 d). Here, we confirm the binary nature of the central star of LoTr 1, consisting of a K1 III star and a hot white dwarf (WD). The nebula of LoTr 1 presents a very different morphology than that of other seemingly similar bCSPNe possessing barium stars, A70 and WeBo 1 (included in this study for direct comparison), which may be an indication of a difference in their mass-transfer episodes. There is no evidence of barium enhancement in the K1 III companion, but it is shown to have a rotation period of 6.4 d which is most likely a sign of mass accretion. Such a system represents a rare opportunity to further the investigation into the formation of barium stars and intermediate period, post-asymptotic giant branch (AGB) systems.

Finally, the first analysis of an object from the new POPIPlaN catalogue of PNe is presented. Photometry of the central star system of PN G033.8+01.5 showed it to be a compact binary of P = 0.1268 d, consisting of a cool M2 V main sequence star and a hot WD surrounded by a very asymmetric PN. The very short orbital period leads to the possibility of PN G033.8+01.5 being a cataclysmic variable candidate, which in turn leads to the question of whether the visible nebulous material is that of a true PN or if it is the remnant of an outburst.

Declaration

I declare that no portion of the work referred to in the thesis has been submitted in support of an application for another degree or qualification of this or any other university or other institute of learning.

Copyright Statement

(i) The author of this thesis (including any appendices and/or schedules to this thesis) owns certain copyright or related rights in it (the "Copyright") and s/he has given The University of Manchester certain rights to use such Copyright, including for administrative purposes.

(ii) Copies of this thesis, either in full or in extracts and whether in hard or electronic copy, may be made **only** in accordance with the Copyright, Designs and Patents Act 1988 (as amended) and regulations issued under it or, where appropriate, in accordance with licensing agreements which the University has from time to time. This page must form part of any such copies made.

(iii) The ownership of certain Copyright, patents, designs, trade marks and other intellectual property (the "Intellectual Property") and any reproductions of copyright works in the thesis, for example graphs and tables ("Reproductions"), which may be described in this thesis, may not be owned by the author and may be owned by third parties. Such Intellectual Property and Reproductions cannot and must not be made available for use without the prior written permission of the owner(s) of the relevant Intellectual Property and/or Reproductions.

(iv) Further information on the conditions under which disclosure, publication and commercialisation of this thesis, the Copyright and any Intellectual Property and/or Reproductions described in it may take place is available in the University IP Policy [i], in any relevant Thesis restriction declarations deposited in the University Library, The University Library's regulations [ii] and in The University's policy on presentation of Theses.

[i] http://www.campus.manchester.ac.uk/medialibrary/policies/intellectual-property.pdf
[ii] see http://www.manchester.ac.uk/library/aboutus/regulations

Acknowledgements

To my **supervisors** - Myfanwy Lloyd at JBCA and Henri Boffin and Dave Jones at ESO, for their time, expertise, and (most importantly) patience whilst working with me.

To my **ESO** friends - in particular Rebeca Aladro, Rebekka Grellman, Javier Rodón, Anna Sippel and Roger Wesson, with whom I have shared hopes, dreams, problems, coffees, beers and holidays with. Your friendships have been invaluable. To everyone else who made my time there a great one: Bruno, Tina, Dani, Flo, Joachim, Hernan, Christoph, Martha, Catherine, Joanne, JK, Paul, Adrien, Julien, Sergio, Caro, Dimitri, Reuben, Juan Carlos M., Liz and Giacomo. And to Michael West and Claudio Melo, who gracefully accepted my presence even after my studentship ended.

To my other amigos in **Santiago** - the wonderful Valeria and Javier, Shelly, Veronica, Trihnity and Pablo (and of course, Darren at The Shamrock for putting up/joining in with our after-hours antics!).

To the **La Palma** crew - the other Dragettes: Lindsay Magill, Annemieke Janssen and Ilona Busenbender. The NOTties: Julie Lykke, Marjaana Lindborg, Søren Frimann, Martin Bo Nielson and Anders Thygesen. And the 'professionals': Andrew Cardwell, Ricardo Cárdenes, Fiona Riddick, Craige Bevil, Sam Rix and James McCormac.

To those back in the **UK** - my BFF, Emma Hicks, who has been there through every up and down. And to the rest of my 'home team': Mandy Bailey, Rob Barnsley, Julia Grey, Stacey Habergham, Rebekah Hounsell, Emma Small, and Tracy, Michael, Annabelle and Sophie McAiney.

To **Oscar González** - for standing by me during the final year of this rollercoaster and for sharing not only your life with me, but also your passion, your drive, your dedication, and your unique view on the world. You make me a better person - I love you.

And ultimately, to my **family** - Mum, Dad, David, Laura, Nan and the rest. For your unconditional love and support throughout all my crazy ventures. This is for you.

The Author

I graduated from the University of Liverpool with a I-class MPhys degree in Astrophysics in July 2008. Feeling more than a little burnt-out after my final exams, I decided to spend one year working in the "real world" (whatever that may be) to re-energise my mind and re-fill my bank account. It sucked. I missed being challenged, I missed learning new things, and I missed the amazingly flexible schedule. And so I re-entered eternal studentdom to start my PhD in October 2009 at the Jodrell Bank Centre for Astrophysics (JBCA) based at the University of Manchester, UK (which, being a Scouser, goes against all sorts of genetic rules and dispositions) to study planetary nebulae possessing binary central stars. And that's how the rollercoaster started.

After my first year at JBCA, I was offered a Research and Support Studentship for the Isaac Newton Group (ING) on the gorgeous island of La Palma, where, after suspending my funding, I spent the year as a Student Support Astronomer and got to intimately know a great little machine - the Isaac Newton Telescope (INT). During my time there, I was encouraged to apply for a European Southern Observatory (ESO) Studentship to continue my studies based in Santiago, Chile. One of those pivotal moments in my life was when I was offered the place, and I, after a huge internal battle, accepted.

After 4 months back in Liverpool to catch up with family and friends over a decent cup of tea, I was on a plane once more to travel 7,000 miles to start a new life in February 2012 in a new hemisphere, timezone, season, and culture. My ESO studentship officially ended in February 2013, but I stayed on using my STFC funding until July 2013 when I had no choice but to go back to Manchester to start writing my thesis.

Three months and four chapters later, I came back to Santiago and back to ESO to finish up. Who knows where I will be next when this thesis becomes published!

Refereed Publications and Conference Contributions

Photometry of the binary central star of PN G033.8+01.5 - a cataclysmic variable candidate

Tyndall, A. A.; Boffin, H. M. J.; González, O. A.; Jones, D. & Lloyd, M. 2014, MNRAS, in preparation.

The post-common-envelope, binary central star of the planetary nebula Hen 2-11

Jones, D.; Boffin, H. M. J.; Miszalski, B.; Wesson, R.; Corradi, R. L. M. & **Tyndall, A. A.**, 2014, A&A, vol. 562, A89

SALT reveals the barium central star of the planetary nebula Hen 2-39

Miszalski, B.; Boffin, H. M. J.; Jones, D.; Karakas, A. I.; Köppen, J.; **Tyndall, A. A.**; Mohamed, S. S.; Rodríguez-Gil, P. & Santander-García, M., 2013, MNRAS, vol. 436, issue 4, pp. 3068-3081

Two rings but no fellowship: LoTr 1 and its relation to planetary nebulae possessing barium central stars

Tyndall, A. A.; Jones, D.; Boffin, H. M. J.; Miszalski, B.; Faedi, F.; Lloyd, M.; Boumis, P.; López, J. A.; Martell, S.; Pollacco, D. & Santander-García, M., 2013, MNRAS, vol. 436, issue 3, pp. 2082-2095

A Black Hole Nova Obscured by an Inner Disk Torus

Corral-Santana, J. M.; Casares, J.; Muñoz Darias, T.; Rodríguez-Gil, P.; Shahbaz, T.; Torres, M. A. P.; Zurita, C.; **Tyndall, A.A.**, 2013, Science, vol. 339, pp. 1048-1051

739 observed NEAs and new 2-4m survey statistics within the EURONEAR network
Vaduvescu, O.; Birlan, M.; Tudorica, A.; Popescu, M.; Colas, F.; Asher, D. J.; Sonka, A.; Suciu, O.; Lacatus, D.; Paraschiv, A.; Badescu, T.; Tercu, O.; Dumitriu, A.; Chirila, A.; Stecklum, B.; Licandro, J.; Nedelcu, A.; Turcu, E.; Vachier, F.; Beauvalet, L.; Taris, F.; Bouquillon, L.; Pozo Nunez, F.; Colque Saavedra, J.P.; Unda-Sanzana, E.; Karami, M.; Khosroshahi, H.G.; Toma, R.; Ledo, H.; **Tyndall, A.**; Patrick, L.; Fohring, D.; Muelheims, D.; Enzian, G.; Klaes, D.; Lenz, D.; Mahlberg, P.; Ordenes, Y. & Sendlinger, K., 2013, Planetary and Space Sciences, vol. 85, pp. 299-311

Discovery of Two Very Wide Binaries with Ultracool Companions and a New Brown Dwarf at the L/T Transition
Mužić, K.; Radigan, J.; Jayawardhana, R.; Ivanov, V. D.; Faherty, J. K.; Kurtev, R. G.; Núñez A.; Boffin, H. M.J .; Hainaut, O.; Cruz, K.; Jones, D.; Metchev, S.; **Tyndall, A.**; Borissova, J., 2012, Astrophysical Journal, vol. 144, p. 180

A study of the kinematics and binary-induced shaping of the planetary nebula HaTr 4
Tyndall, A. A.; Jones, D.; Lloyd, M.; O'Brien, T. J. & Pollacco, D., 2012, MNRAS, vol. 422, pp. 1804-1811

The influence of binarity on the morpho-kinematics of planetary nebulae
Jones, D.; **Tyndall, A.**; Lloyd, M., & Santander-Garcia, M., 2011, Planetary Nebulae: An Eye to the Future, Proceedings of the International Astronomical Union, IAU Symposium, Volume 283, pp. 402-403

Spatio-kinematic modelling: Testing the link between planetary nebulae and close binaries
Jones, D.; **Tyndall, A.**; Lloyd, M.; Huckvale, L., & Prouse, B., 2011, Evolution of Compact Binaries. Astron. Soc. Pac., San Fran., vol 447, page 165

Tyndall, A.; Jones, D.; Lloyd, M.; O'Brien, T. J.; Pollacco, D. & Mitchell, D. L., 2010, Asymmetric Planetary Nebulae V, published by Ebrary, Zijlstra, Lykou, McDonald, Lagadec, eds., pp 121

List of Abbreviations

α Right Ascension

AAT Anglo-Australian Telescope - 3.9m

(E/TP-)AGB (Early / Thermally Pulsing) Asymptotic Giant Branch

CE Common Envelope

(b)CSPN(e) (binary) Central Star(s) of Planetary Nebula(e)

δ Declination

EFOSC2 ESO Faint Object Spectrograph and Camera v.2

EMMI ESO Multi-Mode Instrument

ESO European Southern Observatory

FORS2 FOcal Reducer and low dispersion Spectrograph v.2

FWHM Full Width at Half Maximum

HJD Heliocentric Julian Date

HR Hertzsprung-Russell

INT Isaac Newton Telescope - 2.4m

IPHAS The INT/WFC Photometric Hα Survey

ISM Interstellar Medium

(G)ISW (Generalised) Interacting Stellar Winds

MES Manchester Echelle Spectrometer

MS Main Sequence

NTT New Technology Telescope - 3.6m

PA Position Angle

PN(e) Planetary Nebula(e)

PSF Point Spread Function

PV Position-Velocity

RG Red Giant

RGB Red Giant Branch

SAAO South African Astronomical Observatory

SHS The AAO/UKST Supercosmos Hα Survey

SN(e) Supernova(e)

ThAr Thorium-Argon

SPM San Pedro Martir - 2.1m

(Super)WASP-N/S (Super) Wide Angle Search for Planets North/South

UCLES University College London Echelle Spectrograph

UVES Ultraviolet and Visual Echelle Spectrograph

VLT Very Large Telescope - 8.2m

WD White Dwarf

Dedication

I dedicate this thesis to the family we have lost along the way...

To Uncle Alan, for his love, warmth and intelligence.

To Grandma, for injecting humour into our lives and giving me my stubborn side.

And to Shaishe, for being our rock and always helping me reach for the stars.

Per Ardua Ad Astra

Through hardship to the stars...

1

Introduction

Planetary nebulae (PNe) are regarded as one of the final stages of evolution for an intermediate mass (0.8–8 $M_{\odot}$) star. The outer layers of a cool giant are ejected into its circumstellar environment as it starts the transition to a hot white dwarf (WD), where the material is ionized to become the optically-visible PN. The study of PNe and their progenitors plays a crucial role towards our understanding of the chemical evolution of our Galaxy, as metal-abundant matter is returned to the interstellar medium (ISM). However, before we are able to discuss the bigger implications there is much still to be learned about how PNe evolve to such a state initially, in terms of formation, enrichment and subsequent morphology by the central star. There is evidence to suggest that binary central stars must exist in a large fraction of PNe, but how the two stars interact with each other at both close and intermediate orbital periods still warrants further investigation in itself.

Since the first appearance of the International Ultraviolet Explorer (IUE) satellite in 1978 and the Infra Red Astronomical Satellite (IRAS) in 1983, such technology has allowed the study of PNe and their stellar progenitors at wavelengths not previously accessible from ground-based telescopes. This has allowed astronomers to look in detail at properties such as gas density, temperature and chemical abundances of both the PN

and its central star system, thereby opening up an entire investigative methodology. By studying the two components in parallel we can begin to infer the fundamental physical mechanisms at play, and thus greatly improve our understanding of the nature of these beautiful objects.

1.1 A History

1.1.1 Planetary nebulae

The first PN to be seen by the human eye was the 'Dumbbell nebula' (also known as M27 or NGC 6853), discovered by Charles Messier in July 1764. It was not until 20 years later that the term 'planetary nebula' was coined by pioneering astronomer William Herschel around 1784, believing they bore a resemblance to his newly discovered planet, Uranus, when viewed through a small optical telescope. Further observations then led him to believe that PNe were actually star clusters. However, in 1790 Herschel's observations of NGC 1514 (shown in Fig. 1.1) prompted him to reassess them as being nebulous objects as it allowed him infer that there must be a direct relationship with the very evident central star at its core (Herschel 1791):

> *"A most singular phenomenon! A star of about 8th magnitude with a faint luminous atmosphere, of circular form, and about 3 minutes in diameter. The star is perfectly in the center and the atmosphere is so delicate, faint and equally throughout that there can be no surmise of its consisting of stars; nor can there be a doubt of the evident connection between the atmosphere and the star. Another star, not much less in brightness and in the same field as the above, was perfectly free from any such appearance."*

In 1864, William Huggins observed the 'Cat's Eye nebula' (NGC 6453) where, instead of seeing a strong stellar continuum spectrum with many absorption lines as with previous observations, he instead viewed only a small number of emission lines. One in

Figure 1.1: Composite image of NGC 1514 taken using ALFOSC on the Nordic Optical Telescope with *B*, *V* and *R* filters. Image credit: Jyri Näränen (University of Helsinki), 2005.

particular appeared much stronger than the others and was found to be at a wavelength not attributed to any known element at the time. As such, he named this mystery element 'Nebulium' (Huggins & Miller 1864). Further laboratory experiments conducted by Russell, Dugan & Stewart (1927) were to indicate that the source of the unknown emission line was not from Nebulium at all, but rather it was the result of *"atoms of known kinds shining under unfamiliar conditions"*, in the very low gas density of space. Bowen (1928) was the first to reach the conclusion that it was this low density environment that allowed familiar elements, such as nitrogen and oxygen, the time required to produce emission lines before they become collisionally de-excited (see Fig. 1.2). In the high density molecular environment of Earth's atmosphere, this de-excitation occurs in too short a timescale for these emission lines to ever be observed. As such, they became known as 'forbidden lines', again pointing to the fact the PNe are mostly made up of rarefied gas and not clusters of stars.

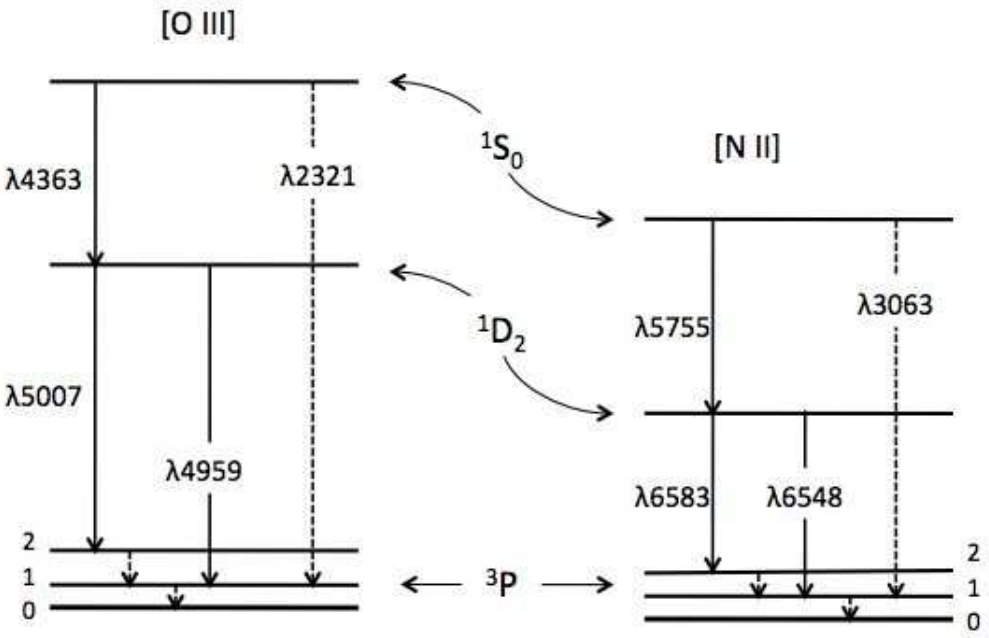

Figure 1.2: Diagram to show the forbidden transitions of [O] and [N]. Image taken from Osterbrock (1989).

1.1.2 Binary stars

Michell (1767) was the first to suggest that double stars - that is, two stars that appear close to each other as viewed from Earth - might be physically attached to each other, by arguing that the probability of a double star appearing as such purely due to chance superposition was small. Having observed and catalogued double stars since 1779, Herschel (1802) first used the term 'binary' in describing two objects that are connected through mutual gravitation:

> *"If, on the contrary, two stars should really be situated very near each other, and at the same time so far insulated as not to be materially affected by the attractions of neighbouring stars, they will then compose a separate system, and remain united by the bond of their own mutual gravitation towards each other. This should be called a real double star; and any two stars that are thus mutually connected, form the binary sidereal system which we are now to consider."*

By noting changes in the relative positions of a number of double stars, Herschel (1803) announced that Castor, first discovered as a double star as far back as 1678, was a true binary system; indeed, it has since been discovered that Castor actually comprises *three* binary pairs, all connected through mutual gravitation. He concluded that some of those he had previously classified must also be binary systems, and so went on to create a new catalogue consisting of 848 binary stars. By the modern definition, the term 'binary star' now refers to stellar pairs that revolve around a common centre of mass, or 'barycentre'.

In a simple two-body case:

$$r = a\frac{m_2}{m_1 + m_2} = \frac{a}{1 + m_1/m_2} \tag{1.1}$$

where r is the distance between the centre of the primary star and the barycentre, m is stellar mass, and a is the total separation between the centres of the stars.

Kepler's third law of planetary motion states:

$$P^2 \propto a^3 \tag{1.2}$$

where P is the planetary orbital period.

A Newtonian refinement to Kepler's third law gives: [i]

$$P^2 = \frac{4\pi^2}{G(m_1 + m_2)}\, a^3 \tag{1.3}$$

where G is the gravitational constant.

[i] Applying Newton's second law of motion (stating that the acceleration of a body is directly proportional to, and in the same direction as, the net force acting on the body and inversely proportional to its mass, $F = ma$), and Gravitational law ($F = -G[m_1 + m_2]/r^2$), states that each star executes an elliptical orbit such that at any instance the two stars are on opposite sides of the centre of mass.

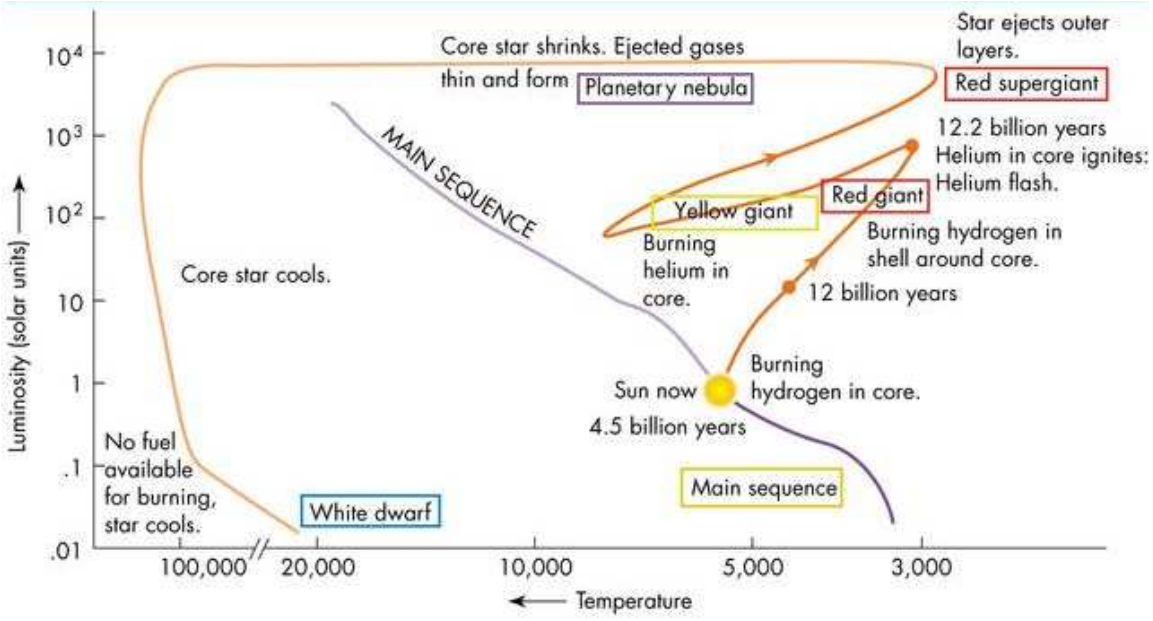

Figure 1.3: Basic Hertzsprung-Russell diagram, showing the evolutionary track for a 1 $M_{\odot}$ star. Image taken from: http://skyserver.sdss.org/dr1/en/astro/stars/stars.asp

1.2 PNe Formation

It was Paczyński (1971) who first identified AGB stars as being the main progenitors of PNe and suggested that they are powered by hydrogen shell burning on a carbon-oxygen (CO) core. The current understanding of the formation of PNe stemming from this work is that they are formed when low-to-intermediate mass stars start to transition from the asymptotic giant branch (AGB) phase to a WD.

1.2.1 The AGB phase

With a single star progenitor, a PN is formed as a 0.8–8 $M_{\odot}$ star ascends the AGB as shown on the Hertzsprung-Russell (HR) diagram in Fig. 1.3, due to a helium (He)-shell burning phase very similar to that found on the red giant branch (RGB). There is a high chance of observing a lower mass star during this phase due to their slower rate of nuclear burning compared to high mass stars. During the early AGB phase,

both the stellar radius and mass increase as He-burning moves to a shell around an inert CO core and moves progressively outwards, which also results in an increase in surface brightness by at least an order of magnitude. Higher mass stars (> 3–5 $M_{\odot}$) go through a second 'dredge-up' phase, whereby the energy produced by the He-burning shell causes the base of the hydrogen (H)-rich envelope to expand and cool, causing H-burning in the shell to 'switch off'. At this moment the outer convective area extends into the H-depleted zone, thereby transporting the resultant products of H-burning to the stellar surface as it reaches the base of the AGB. Lower mass stars do not go through a second dredge-up phase, however, as H-burning remains efficient and prevents the outer convective zone from permeating deeper into the star. Stars less massive than 8 $M_{\odot}$ enter the 'thermally pulsing AGB phase' (TP-AGB), as without the extra pressure generated by the second dredge-up nucleosynthesis, the core contracts to the point where electron degeneracy pressure allows the star to regain hydrostatic equilibrium. Above 8 $M_{\odot}$ at solar metallicity, z = 0.02 (decreasing to 4 $M_{\odot}$ for z = 0.001), the electron degeneracy in the core is no longer sufficient to retain equilibrium and the core begins to collapse. However, neutron degeneracy halts the process and the core material is rebounded in a Type-II supernova (SN) explosion.

After helium burning ceases the TP-AGB phase starts, marked as the point where H-burning alone becomes a sufficient supplier of stellar energy as the star undergoes a contraction. The star then derives its energy from H fusion in a thin shell, inside of which lies the now inactive He. However, for an average CO core mass of ~0.6 $M_{\odot}$ and after a period of quiescence (10 000–100 000 yrs) He-burning switches on again and the H-burning ceases – the point at which the burning alternates is known as a 'thermal pulse', or a 'helium shell flash' (see Fig. 1.4). These strong pulsations, which only last a few thousand years, increase in amplitude and frequency as the star ascends the AGB, causing material created in the He-burning shell to be convectively mixed and transported past the H-burning shell and into the deep convective H envelope. This is known as the 'third dredge-up'. The result is the formation of an extended envelope showing a high abundance of He and ^{12}C.

Following the third dredge-up, H-burning switches on again, and He-burning ceases to repeat the process. This cycle can repeat many times, allowing further nucleosynthesis to occur to produce heavier elements such as ^{14}N, ^{18}O, and ^{22}Ne. In the later thermal pulses of an intermediate mass AGB star, the reaction ^{22}Ne –> ^{25}Mg in the inter shell region between the H- and He-burning shells (where it was synthesied during previous H-burning phases) results in the release of a high flux of neutrons that become utilised in a slow-neutron capture process (s-process) that manufactures elements beyond Fe such as Ba, Zr, Y, Sr and Pb (in the case where $T_{\rm eff}$ ~3.5×10^8 K). For lower mass AGB stars, the required neutrons can be sourced from the reaction ^{13}C –> ^{16}O if $T_{\rm eff}$ ~ 9×10^7 K. The presence of ^{99}Tc in the atmosphere of AGB stars (Little, Little-Marenin & Bauer 1987; Smith & Lambert 1988) provides important evidence that this s-process nucleosynthesis happens intrinsically in the star and that it is not the consequence of pollution during its initial formation, due to its unstable half-life of 2×10^5 yrs.

1.2.2 Envelope ejection

Towards the end of the AGB phase, the star suffers significant mass loss in the form of a stellar wind. In single star models, radiation pressure (with perhaps some contribution from acoustic waves or radial pulsations from the central star; Pijpers & Hearn 1989) on cool, condensed dust grains in the outer regions of the star (Zijlstra 2007) drives away matter from the stellar surface, dragging gas with it due to frictional forces. The result is a total loss of 50%-70% of the initial mass, with a mass loss rate potentially as high as 10^{-5} $M_\odot$ yr^{-1} (Balick & Frank 2002). The composition of the material lost during this process is assumed to be similar to that of the envelope near the termination of the TP-AGB phase. However, the efficiency of such a dust-driven wind has been questioned by Woitke (2006), and indeed it is still not clear what the exact driving mechanism behind this AGB mass loss is. Eventually the mass loss rate exceeds the nuclear burning rate and the stellar envelope becomes completely depleted, leaving

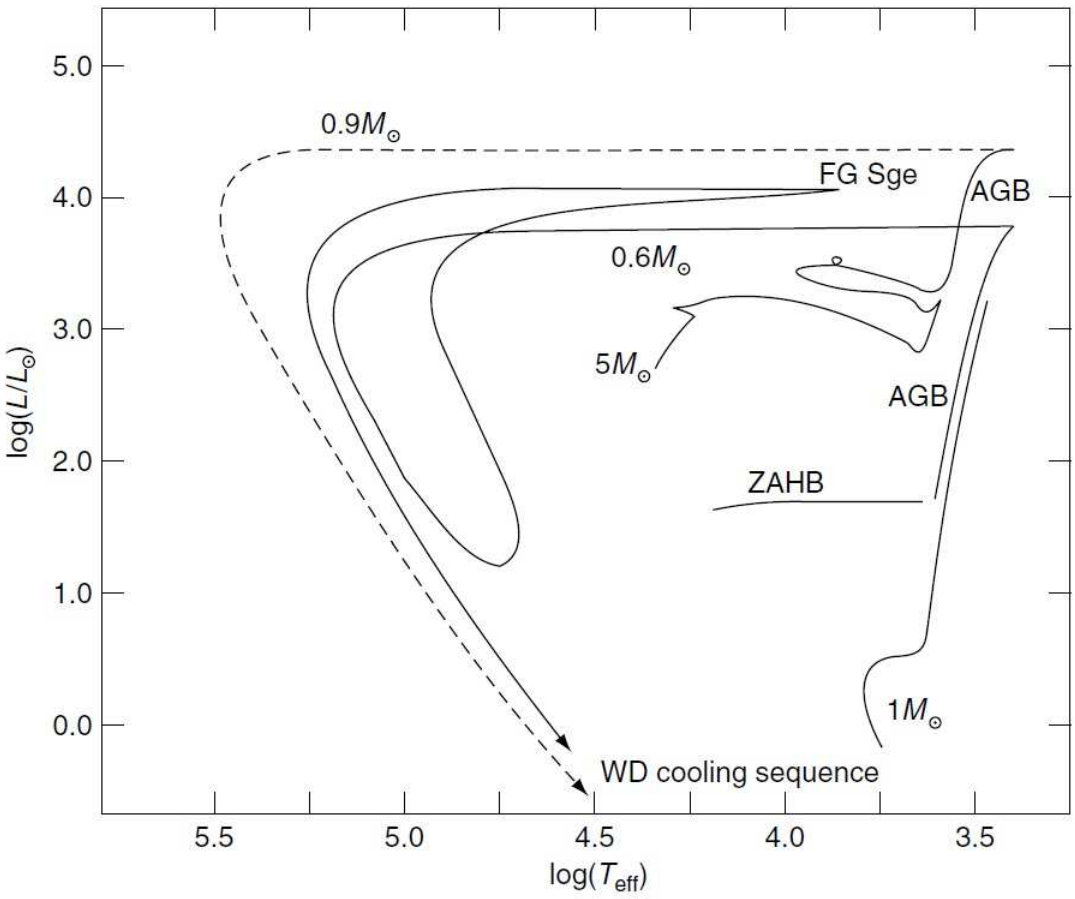

Figure 1.4: Evolutionary tracks from MS to WD phase for stars of initial MS masses 1 $M_\odot$ and 5 $M_\odot$, ending their lives as 0.6 $M_\odot$ and 0.9 $M_\odot$ remnants respectively (shown here from the end of the AGB). The 1 $M_\odot$ star experiences a final He-shell flash before reaching the WD cooling phase. An observed counterpart, FG Sge (0.61 $M_\odot$; Blocker & Schonberner 1996), is also shown. Image taken from Salaris & Cassisi (2005).

behind the remnant CO core. As the star makes this transition, the mass loss rate decreases to around 10^{-8} $M_\odot$ yr^{-1} and wind speeds increase from 10 km s^{-1} to 10^3 km s^{-1}. The hot (> 25 000 K) WD ionizes the stellar ejecta to create a PN that is visible across the entire wavelength range, giving rise to various emission line spectra.

Traditional theories of how the enriched, extended envelope is expelled into the surrounding ISM mostly pointed to some form of sudden-ejection mechanism, including recombination-induced dynamical instabilities (Roxburgh 1967; Lucy 1967),

radiation pressure (Faulkner 1970; Finzi & Wolf 1971), envelope relaxation oscillations due to thermal instabilities in the core (Smith & Rose 1972), pulsational instabilities (Kutter & Sparks 1974; Wood 1974; Tuchman, Sack & Barkat 1979), or thermal pulses (Trimble & Sackmann 1978). However, none of these theories allow for sufficient mass to be expelled to produce such a PN, and, conversely, if too much is ejected then the progenitor will evolve too slowly to reach the temperatures necessary to ionize the PN before it dissipates (Kwok 2002). Even if the PN was created by a sudden-ejection event, a source of additional pressure is required to maintain the expansion of the nebula and prevent material from falling back onto the central star. Soker (1996) calculated that gas pressure is the driving force for expansion and the resultant high-velocity wind would prevent such back-fall of material, but discovered along with it that the PN would disperse very quickly. It therefore becomes apparent that some form of continuous mass loss mechanism is required to replenish the nebula.

1.2.3 Interacting winds

The summary of envelope ejection is that PNe are formed as a result of the interaction between the slow wind initially expelled from AGB progenitor, with a fast wind stemming from the resultant hot central star (Kwok 2002). Kwok, Purton & Fitzgerald (1978) first put forward the 'Interacting Stellar Winds' (ISW) theory of nebular shaping, whereby the PN is shaped by a 'snowplough' process. Here, the slow wind emanating from the remnant AGB stellar envelope is overtaken by faster, more tenuous material, resulting in the compression of the slower material into a thin, dense shell at the leading edge of the fast-wind 'bubble'. This leading edge is then ionized by the central star and gives us the visible PN. In general, all winds in these circumstances are inherently isotropic (Balick & Frank 2002) which in theory would lead to the formation of a spherical nebula around the stellar progenitor. This model is nicely confirmed by such PNe as NGC 3132 and NGC 6826, which show mostly round morphologies.

Despite strong observational evidence for the existence of PNe stemming from a

single star progenitor (e.g. Habing 1996), there was still no clear mechanism that would explain how a lone AGB star would produce the observed ~80% of PNe that actually show non-spherical, highly complex, axisymmetric structures (Parker et al. 2006), as well as microstructures, as the ISW model alone cannot explain how this occurs from what is initially a spherically-symmetric mass loss (Soker & Regev 1998). The most abundant cases of non-spherical PNe are those that are bipolar in shape (e.g. NGC 2346 and NGC 6302), defined as those that possess two axisymmetric lobes on opposing sides of the central star and some form of equatorial 'waist'. Discoveries of proto-planetary nebulae (pPNe) with bipolar structures (e.g. AFGL 2688, Latter et al. 1993; IRAS 17150-3224 and IRAS 17441-2411, Kwok et al. 1996) suggest that the transformation to this bipolar shape occurs soon after the end of the AGB (Kwok et al. 1996; Zhang & Kwok 1998). Balick (1987), Icke (1988), and Mellema & Frank (1995) carried out several observations to confirm the theory of Calvet & Peimbert (1983) that if the circumstellar envelope is initially disc-like (i.e. if there is a dense equatorial enhancement), then the fast and slow winds of the ISW model can be deflected towards a polar axis to form a pair of expanding bubbles; one moving outwards into the surrounding circumstellar material and the other moving inwards towards the slow, diluted stellar wind to give rise to highly bipolar shapes. This then became known as the 'Generalised Interacting Stellar Winds' (GISW) model as the process could be generalised to account for many types of aspherical nebulae. Still, as with the original ISW model, the GISW was proved to be an inadequate mechanism on its own; the origin of the initial discs could not be inferred from it, and higher-order structures (such as multiple, axisymmetric lobe pairs) still could not be predicted either.

Alternative theories put forward to explain the non-homogeneity were:

- **Intrinsic asymmetric density profile / wind instabilities** – these asymmetries in the AGB wind, first discussed by Kahn & West (1985a), have been shown to be *amplified* by the ISW model, but not be responsible for it (Kwok 2002).

- **Rapid rotation** – if the central star is rapidly rotating, then conservation of an-

gular momentum requires the isotropy of the slower stellar wind to break down (Friend & Abbott 1986; Poe & Friend 1986). However, the rotational speeds required for this to be the case would in all likelihood break up the entire system (Bond & Livio 1990).

- **Magnetic fields** – the discovery of the presence of magnetic fields within several AGB stars (e.g. Etoka & Diamond 2004) and even within some PNe themselves (Jordan, Werner & O'Toole 2005) has led some to believe that there is a dynamo effect at play that can create fields strong enough to shape the outflows responsible for the formation of bipolar nebulae (Blackman et al. 2001). However, it has been shown that large magnetic fields carry angular momentum away from the stellar envelope on a timescale much shorter than that due to a stellar wind, with the result being that the star is spun down and the magnetic field, powered by stellar rotation, is drained (Soker 2006; Nordhaus & Blackman 2006).

Many bipolar PNe are also 'point-symmetric', in that for each microstructure a similar one appears on the opposing side of the nebula. Examples include:

- **Knots** – otherwise known as 'Fast, Low Ionization Emission RegionS' (FLIERS), so named as velocities are high compared to the circumstellar material through which it travels (Balick et al. 1993). Often found in pairs on opposing sides of the nebula (see Fig. 1.5).

- **Jets** – found in about half of all PNe (Gonçalves, Corradi & Mampaso 2001), jets 'connect' opposing knot structures pointing to the existence of a collimation effect directly from the central star. They are believed to be formed between the end of the AGB slow wind formation and the beginning of the fast wind phase (Soker & Livio 1994; see Fig. 1.6).

  The most obvious mechanism for such collimated outflows is accretion. Two other possible explanations for why these outflows should have a preferred axis are stellar rotation and/or magnetic fields (Balick & Frank 2002), and indeed

models have been successful in reproducing outflows via these methods for a single star progenitor. However, in reality the angular momentum needed for the rotation is exceedingly great, and the magnetic field theory has been argued against as mentioned earlier in this section. As such, it was decided that another entity was required to supply the excess angular momentum required for rotation to create collimation effects (Zuckerman & Gatley 1988) which in turn lead to the complex and varied structures of PNe.

- **Concentric rings/arcs** – currently, there are 12 PNe that have been observationally shown to possess concentric rings (see Fig. 1.7). Corradi et al. (2004) state that they should not to be treated as separate entities as they are in fact multiple shock edges (discussed in the ISW model) as seen projected in the plane of the sky, i.e. they are density variations that are relatively evenly spaced and surround a structured inner PNe. Since these rings are dimmer and larger than the nucleus it gives rise to the possibility that they were episodically ejected early on in the life of the PN – a result of the slow AGB wind (Bond & Livio 1990). The brighter nucleus could represent rapid mass loss that occurred at the tip of the AGB. This leads to the question as to whether stellar mass loss somehow abruptly changes from something isotropic to something more complex during the AGB phase, in order for the progenitor to go from creating concentric rings to creating the nebula we see today. Possible mechanisms for their formation, as mentioned by Corradi et al. (2004), are magnetic activity cycles (Soker & Rappaport 2000; García-Segura, López & Franco 2001), instabilities in dust-driven winds (Simis, Icke & Dominik 2001), and stellar oscillations (Van Horn et al. 2003; Zijlstra, Bedding & Mattei 2002; Soker 2004). Mastrodemos & Morris (1999) also argue that the rings could originate from spiral wakes produced by binary companions in circular orbits, and the predicted frequency of such companions (Yungelson, Tutukov & Livio 1993), seems in rough accordance with observations.

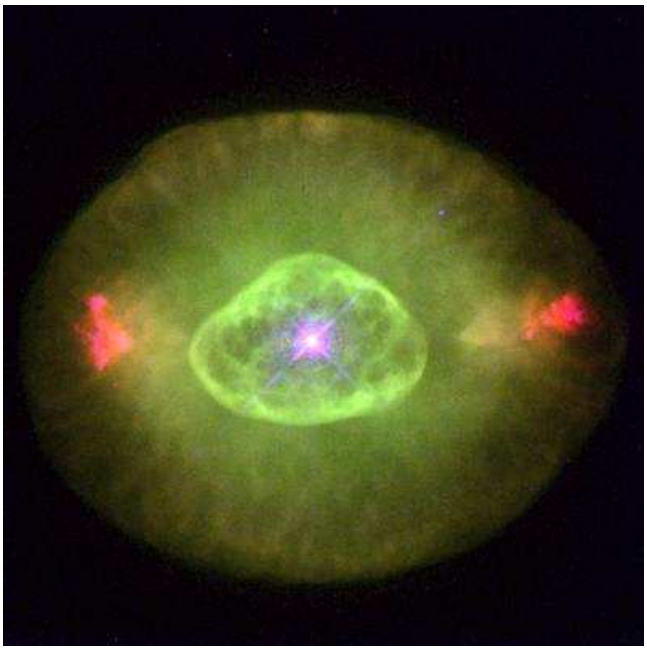

Figure 1.5: HST image of NGC 6826 displaying knot-like structures at opposing ends of the nebula. Image taken from the Hubble archive.

Figure 1.6: VLT-FORS2 image of PN Fleming 1 (Fg 1) displaying jet-like structures. Image credit: Henri Boffin (ESO).

Once again, a new theory was required to account for these microstructures that neither the ISW or the GISW could predict. It was in 1990 that Bond & Livio started to build on the theory that it is in fact binary interactions, and not single star interactions as previously modelled until then, that would help us to get closer to an explanation. What is mainly required is some factor that allows the extraction of angular momentum

Figure 1.7: HST image of the Cat's Eye nebula, NGC 6543, displaying many concentric rings. Image taken from the Hubble archive. Image credit: NASA, ESA, HEIC, and The Hubble Heritage Team (STScI/AURA)

and mass from the system to drive PN formation, and this is in the form of a binary star system.

1.3 Binary star systems within PNe

It is believed that about 30–40% of field stars are members of binary systems (Parker et al. 2006; Jacoby et al. 2010). Such binary stars can form through three possible channels:

1. **During star formation** – either the protostellar disc fragments with an excess of angular momentum and in the absence of a substantial magnetic field (Machida et al. 2008), or the two stars form independently but close together and are then gravitationally bound by one of the two (much less likely) processes below.

2. **Tidal capture** – one star has a close encounter with another, causing a tidal dissipation of energy to form a gravitationally bound pair.

3. **Three-body interaction** – a triple encounter occurs, with one star being ejected and removing excess kinetic energy to allow the other two to remain bound.

1.3.1 Common envelope evolution

Where a PN formed from the model of a single red giant is the result of losing envelope mass into the surrounding ISM as mentioned in Sec. 1.2.2, a close binary core would form a PN by ejection of a 'common envelope' (CE). A close binary system can be defined as such if one of the two stars has or will expand to the point where it fills its 'Roche lobe' and begins to transfer matter onto the companion as a result (Iben & Livio 1993). The Roche lobes are regions of space around each star that define how matter is gravitationally bound to the star. Material within the Roche lobe is gravitationally bound to it, whilst any that falls outside is not and may be transferred to the binary companion.

The effective Roche lobe radius is mainly dependent on the orbital separation and the mass ratio (Eggleton 1983), and this dependency is given by the equation:

$$R_l = \frac{0.49\, q^{2/3}}{0.6\, q^{2/3} + \ln(1 + q^{1/3})} \times a \tag{1.4}$$

where R_l is the Roche lobe radius, q is the mass ratio M_1/M_2, [ii] and a is the orbital separation between the two stars (i.e. the semi-major axis of the system).

As one moves further from the centre of the star, tidal forces from the companion cause the lobes to be elongated parallel to the axis linking the two stellar cores to create a teardrop shape – the greater the percentage of Roche lobe that is filled (also known as the 'Roche lobe filling factor'), the greater the deformation. Once a star has expanded sufficiently to fill its Roche lobe (i.e. it has reached its Roche radius), it begins to transfer mass onto the companion via the inner Lagrangian point, L1 – the point of gravitational equipotential where the two teardrop-shaped Roche lobes meet that allows matter to flow freely from one star to the other (see Fig. 1.3.1). This is known as 'Roche lobe overflow' (RLOF).

When the transfer rate reaches a level beyond what the companion can thermally adjust to, accretion of matter simply cannot happen fast enough and the accreting star

[ii] $R_{l1} => M_1/M_2$, and $R_{l2} => M_2/M_1$

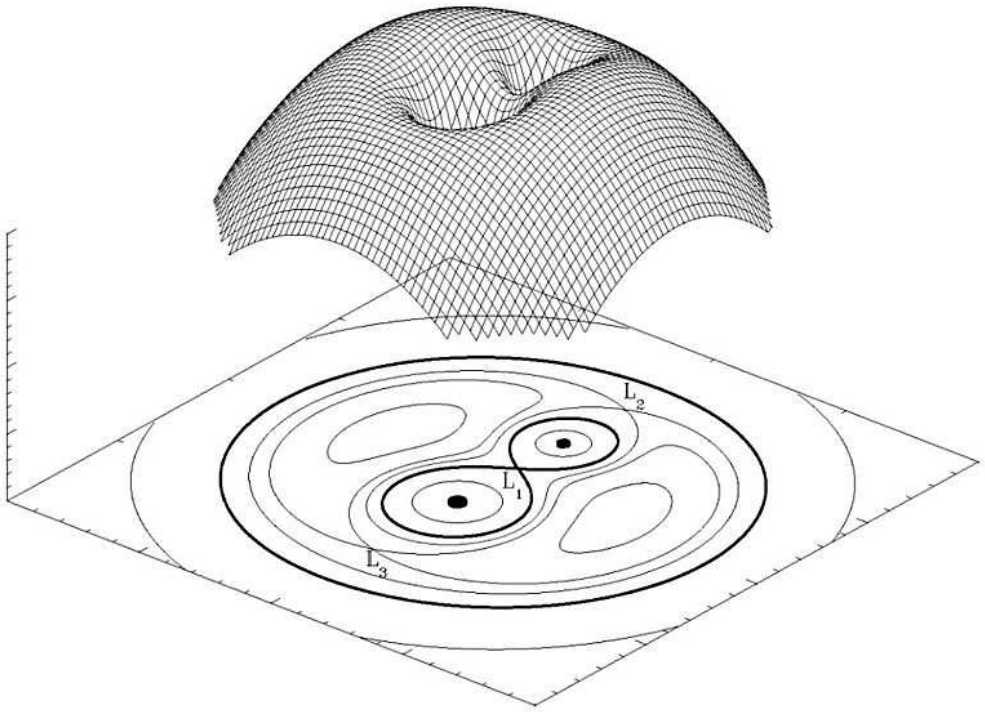

Figure 1.8: Figure to show Roche lobe geometry with Lagrangian points. Both a 3D representation and the resultant 2D map are shown. Image credit: Marc van der Sluys (2006)

deviates from thermal equilibrium, expands and becomes over-luminous. This is referred to as an unstable mass transfer from the donor star, generally resulting in the Roche lobe of the companion filling up and overflowing to create a CE which encompasses both of the stars [iii]. While the relative size of the two Roche lobes is dependent on the mass ratio of the two stars, the absolute size scales with both the stellar separation and the Roche lobe filling factor; for example, if the system has a fixed mass ratio and absolute stellar size in a close system, then the stars may fill their Roche lobes with a high level of deformation to the teardrop shape. If the stars in the binary system are not very massive (given their evolutionary phase at that moment and assuming thermal equilibrium), or if the orbital separation is too wide for the given stellar parameters, it will remain as a 'detached' system as neither star will fill its Roche lobe – that is, no mass transfer between the primary and secondary will occur in the form

[iii] However, there are some exceptions to this as not all interacting binaries go through a CE phase e.g., Algol-type binaries.

of RLOF. However, mass transfer by wind accretion may still occur (see Sec. 1.3.2). If one star fills its Roche lobe and begins to accrete material onto the companion, then it is noted as a 'semi-detached' system. A 'contact' binary system is where both stars fill their Roche lobes and are so close that they actually touch at the L1 point. When both stars fill their Roche lobes to form a CE, this s referred to as an 'over-contact', or 'interacting' binary system.

The difference in angular velocity between the orbital motion of the two stars and the CE cause drag forces which decrease the orbital velocity and results in the two stars spiraling in towards each other, thus greatly reducing their orbit from a period of tens of years (due to initially being a red giant or AGB star with a diameter of hundreds of solar radii, $R_{\odot}$, greatly exceeding the observed orbital separation) to those that only take a couple of days (the diameter of the progenitor, i.e. the resultant WD, is reduced to a few tenths of $R_{\odot}$). Frictional and tidal forces generally cause the binary orbits to circularise – the smaller the orbital separation, the shorter the circularisation timescale. Orbital angular momentum is transferred to the CE, which in turn spins up and is ejected. The result is a close binary system surrounded by the ionized PN (see Fig. 1.3.1).

Bond & Livio (1990) state that if the primary star is a first stage red giant then merging of the two stars is likely, unless the companion is fairly massive. If envelope ejection occurs during the RGB phase it will preferentially be in the binary orbital plane, resulting in a high density contrast of material between the polar and equatorial regions and therefore a brighter nebula. If the primary is an AGB star, however, it is far less likely that the two will merge into a single star and the PN density contrast will be much lower, resulting in a less bright, but larger, nebula (Soker 2006). The shaping is then determined by the ISW/GISW wind theories (see Sec. 1.2.3). In order to fully confirm that a particular nebular morphology is directly related to binarity, it is important that one also gains a complete picture of the central star system as well as the surrounding PN to eliminate any uncertainty. The PN symmetry axis is always perpendicular to the orbital plane of the central binary system in CE models, and if

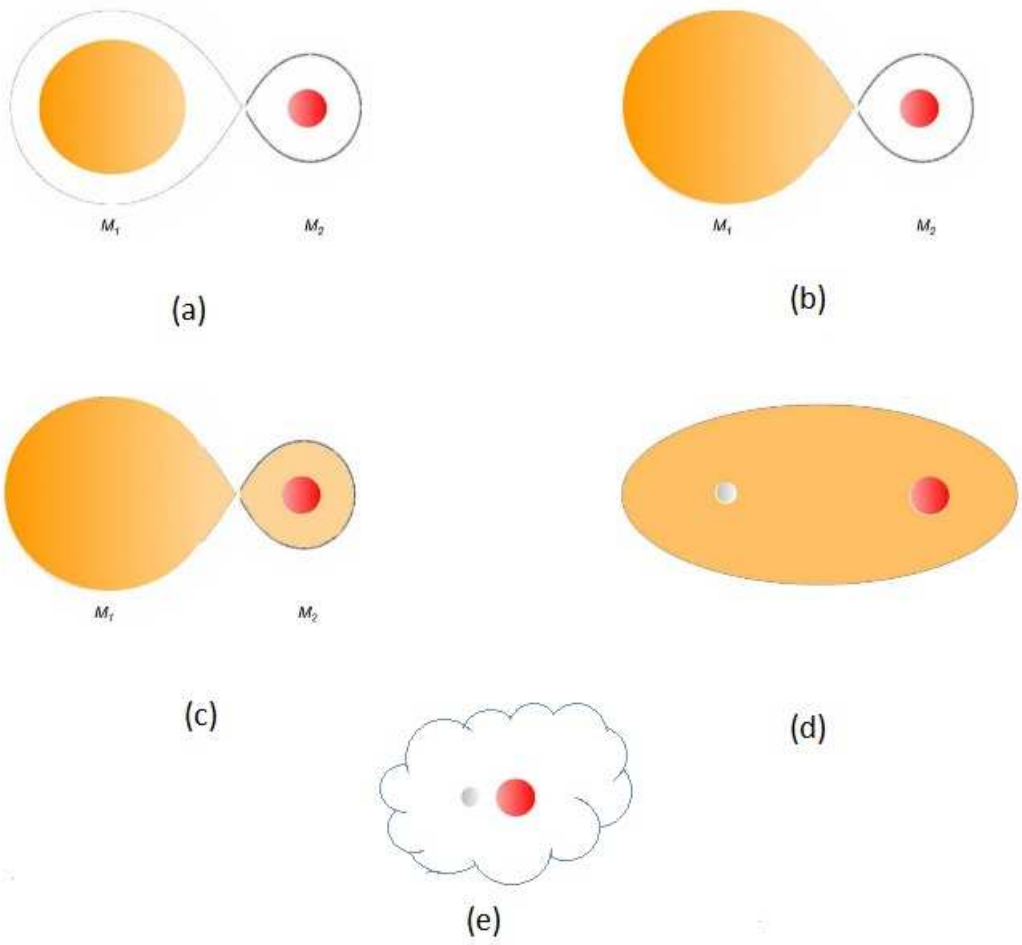

Figure 1.9: Example of CE formation in a close binary system. (a) A giant star and its companion are gravitationally bound. The small mass ratio causes deformation to their Roche lobes. (b) As the PN progenitor ascends the AGB, it fills its Roche lobe. (c) Accretion of matter from the progenitor onto the companion causes the companion to also fill its Roche lobe. (d) The result is the ejection of a CE surrounding the progenitor, now a WD, and its companion. (e) The two stars spiral in towards each other as orbital angular momentum is transferred to the CE, causing the orbital period of the system to decrease. The result is a close binary within a PN. Image credit: Philip Davis (thesis, 2009)

the nebular inclination can be shown to be consistent with the inclination of the binary then it provides strong evidence for binary-induced shaping. However, imaging is insufficient to determine this on its own due to a degeneracy between PN inclination and morphology, e.g. when the symmetry axis of a bipolar nebula is aligned perpendicular to the plane of the sky, it makes the nebula appear spherical (Kwok 2010). If the nebular morphology is classified incorrectly then the fraction of aspherical PNe

possessing a binary core will also end up being inaccurate, and this information is already exceedingly limited for wider binaries due to lack of observations partly as a result of some of the detection biases that will be discussed in Sec. 1.3.4. Longslit spectroscopy focusing on Hα, [N]λ6584 Å and [O]λ5007 Å emission can be used to acquire spatially-resolved velocity maps of the constituent parts of the nebula in order to recover the 'missing' third dimension of the morphology one cannot gain from imagery alone.

To date, there have been 47 PNe detected that possess a close binary central star system (listed in Tab. 1.3.1 below), with almost half of these having been discovered from the Optical Gravitational Lensing Experiment (OGLE) survey (Miszalski et al. 2009a). Of the approximately 3000 known PNe in our Galaxy very few of these have had their central star systems studied in detail to determine if binarity is present (of any orbital separation), and so it is vital that the search for the connection continues. It can be seen in Tab. 1.3.1 that there is quite a wide spread in the detected periods of these systems, e.g. NGC 2346 has a period of 15.99 d, whilst A41 has a period of 0.113 d. Not only are binary detections and analyses hampered by strong selection effects, but the current knowledge of the CE phase is still not complete enough to predict, let alone fully understand, the orbital period distribution for close binary systems. It should be noted that both PHR J1804-2913 (6.66 d) and PHR J1744-3355 (8.2 d) are not fully confirmed as being true close binaries Miszalski et al. (2011b) , with PHR J1804 appearing to show the rotational period of a red giant (inferring that it could possibly still be a binary, but through mass accretion rather than CE evolution), and PHR J1744 may consist of two unrelated stars that have yet to be confirmed as such (B. Miszalski, private communication).

Table 1.1: PNe with known close binary central stars (post-CE systems). Binary class definitions are as follows: E = eclipsing, e = ellipsoidal variation, I = irradiation effects, S1 = single-lined spectroscopic binary, S2 = double-lined spectroscopic binary. Table reproduced in part from De Marco (2006) and B. Miszalski (private communication).

PN G	**Name**	**RA**	**Dec**	**Binary class**	**Period (d)**	**Reference**
136.3+05.5	HFG 1	03 03 47.0	+64 54 35	I, S2	0.582	Grauer et al. (1987), Acker & Stenholm (1990), Exter et al. (2005)
215.6+03.6	NGC 2346	07 09 22.5	-00 48 24	S1	15.99	Méndez & Niemela (1981)
253.5+10.7	K1-2	08 57 45.9	-28 57 36	I, S1	0.676	Kohoutek & Schnur (1982), Exter, Pollacco & Bell (2003)
283.9+09.7	DS 1	10 54 40.6	-48 47 03	I	0.357	Drilling (1985), Kilkenny, Spencer Jones & Marang (1988), Bond (2000)

Table 1.3.1 continued...

144.8+65.8	BE UMa	11 57 44.8	+48 56 19	E	2.29	Liebert et al. (1995), Wood, Robinson & Zhang (1995), Ferguson et al. (1999)
329.0+01.9	Sp 1	15 51 40.9	-51 31 28	I	2.91	Bond & Livio (1990), Méndez et al. (1988)
222.8-04.2	PM 1-23	06 54 13.43	-10 45 38.2	e	0.31	Hajduk, Zijlstra & Gesicki (2010)
341.6+13.7	NGC 6026	16 01 21.1	-34 32 37	E, S1	0.528	Hillwig (2004), Hillwig et al. (2010)
355.2-03.6	HaTr 4	16 45 00.2	-51 12 20	I	1.74	Bond & Livio (1990), Tyndall et al. (2012)
009.6+10.5	A41	17 29 02.0	-15 13 04	e, S2	0.113	Grauer & Bond (1983)
349.3-01.1	NGC 6337	17 22 15.7	-38 29 03	I	0.173	Hillwig (2004), Hillwig et al. (2010)
055.4+16.0	A46	18 31 18.3	+26 56 13	E, I, S2	0.472	Bond (1985) Pollacco & Bell (1994)
005.1-08.9	Hf 2-2	18 31 30.9	-28 43 20	I	0.399	Bond (2000), Lutz et al. (2010)

Table 1.3.1 continued...

053.8-03.0	A63	19 42 10.4	+17 05 14	I, S2	0.456	Bond, Liller & Mannery (1978), Pollacco & Bell (1993)
017.3-21.9	A65	19 46 34.2	-23 08 13	E	~1	Bond (2000), Walsh, J. R. and Walton, N. A. (1996)
359.1-02.3	M 3-16	17 52 46.0	-30 49 34	E, e	0.574	Miszalski et al. (2008a)
357.6-03.3	H 2-29	17 53 16.8	-32 40 39	E	0.244	Miszalski et al. (2008a)
000.2-01.9	M 2-19	17 53 45.6	-29 43 46	e	0.670	Miszalski et al. (2008a)
	M 1-34	18 01 22.2	-33 17 43	E	-	Miszalski et al. (2008b)
003.1-02.1	PHR J1801-2718	18 01 24.4	-27 18 09	I	0.322	Miszalski et al. (2008b)
001.8-03.7	PHR J1804-2913	18 04 28.5	-29 13 57	I	6.660	Miszalski et al. (2008b)
004.0-02.6	PHR J1804-2645	18 04 59.5	-26 45 17	E	0.625	Miszalski et al. (2008b)
355.6-02.3	PHR J1744-3355	17 44 27.9	-33 55 20	I	8.234	Miszalski et al. (2008b)
355.3-03.2	PPA 1747-3435	17 47 08.3	-34 35 43	I	0.225	Miszalski et al. (2009a)
354.5-03.9	Sab 41	17 48 16.3	-35 38 31	I	0.297	Miszalski et al. (2009a)
359.5-01.2	JaST 66	17 49 22.2	-29 59 27	E	0.276	Miszalski et al. (2009a)
000.6-01.3	Bl 3-15	17 52 35.9	-29 06 39	E	0.270	Miszalski et al. (2009a)

Table 1.3.1 continued...

358.7-03.0	K 6-34	17 54 41.1	-31 31 43	E, I	0.393	Miszalski et al. (2009a)
357.0-04.4	PHR 1756-3342	17 56 39.5	-33 42 31	I	0.266	Miszalski et al. (2009a)
001.8-02.0	PHR 1757-2824	17 57 42.2	-28 24 07	E, I	0.799	Miszalski et al. (2009a)
001.2-02.6	PHR 1759-2915	17 59 02.8	-29 15 01	E	1.103	Miszalski et al. (2009a)
000.5-03.1	MPA J1759-3007	17 59 15.6	-30 02 47	E	0.503	Miszalski et al. (2009a)
001.9-02.5	PPA 1759-2834	17 59 52.6	-28 34 47	I	0.305	Miszalski et al. (2009a)
000.9-03.3	PHR 1801-2947	18 01 13.4	-29 47 00	I	0.316	Miszalski et al. (2009a)
005.0+03.0	Pe 1-9	17 45 36.9	-23 02 27	E	0.14	Miszalski et al. (2009a)
355.7-03.0	Hen 2-283	17 47 49.39	-34 08 05	I	1.13	Miszalski et al. (2009a)
357.1-05.3	BMP 1800-3407	18 00 26.5	-34 07 49	E, I	0.14	Miszalski et al. (2009a)
338.1-08.3	NGC 6326	17 20 46.3	-51 45 15	I	0.372	Miszalski et al. (2011c)
034.5-06.7	NGC 6778	19 18 24.9	-01 35 47	I	0.1534	Miszalski et al. (2011c)
054.2-03.4	The Necklace	19 43 59.5	+17 09 00	I	1.161	Corradi et al. (2011), Miszalski et al. (2012)
068.1+11.0	Ethos 1	19 16 31.5	+36 09 47	I	0.535	Miszalski et al. (2011a)

Table 1.3.1 continued...

135.9+55.9	SBS 1150+599A	11 53 24.7	+59 39 57	e, S	0.163	Tovmassian et al. (2004), Tovmassian et al. (2010)
049.4+02.4	Hen 2-428	19 13 05.2	+15 46 39	E, e	0.176	Santander-Garcia et al. (2011)
	Hen 2-11	08 37 08.0	-39 25 05	I	0.610	Jones et al. (2014)
290.5+07.9	Fleming 1	11 28 36.20	-52 56 04	S1	1.19	Boffin et al. (2012b)
N/A	GK Per	03 31 11.8	43 54 17	S1	2	Bode et al. (1987)
N/A	V 458 Vul	03 31 11.8	43 54 17	S1	0.068	Rodríguez-Gil et al. (2010)

1.3.2 Wind accretion scenario

If the mass ratio of the primary and secondary stars is small ($M_2/M_1 < 1$) or their orbital separation is great, a binary system will not undergo CE evolution but instead the mass is transferred from the primary star to the companion via 'wind accretion'. Here, the wind emanating from the AGB star is captured by a MS companion, forming an accretion disc. However, the system always remains detached with both stars avoiding RLOF. By avoiding the CE phase, the stars will not have the loss of angular momentum and so will not spiral into a close binary orbit, resulting in an intermediate period binary system, P = 100–1500 d.

Models involving RLOF were used not only to describe the CE evolution of close binary systems, but also in the formation of barium (Ba) stars. Ba stars are G or K type giants that display an overabundance of s-process elements, first discussed by Bidelman & Keenan (1951) who noted a group of stars with strong spectral lines corresponding in particular to barium at 4554Å, but also Sr as well as CH, CN and C_2 bands. However, there was no viable explanation as to how the observed G and K type giants could be classified as Ba stars when their evolutionary state would not be high enough to undergo the necessary nucleosynthesis to form such elements. It was subsequently identified that all Ba stars are in fact members of binary systems (McClure 1983; McClure & Woodsworth 1990), and Boffin & Jorissen (1988) determined that a wind accretion scenario provides a good explanation as to how these overabundances occurred, alongside why Ba stars were often detected alongside a WD companion. In the wind accretion scenario, the stellar wind emanating from the AGB progenitor is accreted onto its MS companion. The companion becomes 'polluted' by the wind that has been enriched with the s-process elements generated during the third dredge-up phase (see Sec. 1.2.1), the result being a PN with a WD core and a giant companion that has retained the chemical peculiarities it acquired on the MS. This scenario also allows the binary orbit to retain its eccentricity (as is often found with barium stars), which the CE evolution does not. Typically, RLOF is too dynamically unstable for

a MS star to accrete without forming a contact system, and would result in the formation of a degenerate system such as a cataclysmic variable. The fact that Ba stars are not found within such systems provides more evidence to support wind accretion over RLOF and that the process must have occurred before the companion ascended the AGB (Jorissen & Boffin 1992). It has also been shown that the level of pollution is dependent on the orbital separation, with higher abundances of Ba being found in those stars in closer orbits compared to those in wider systems (Boffin & Zacs 1994).

1.3.3 Detecting binary systems

There are four main types of binary system, each requiring its own methods for both detection and subsequent analysis:

- **Visual binaries** – binaries which can be visually resolved into their constituent components. They tend to possess large separations with periods ranging from tens to hundreds of years, and as such their orbital velocities are too small to be measured spectroscopically (therefore neither can the radial velocity be determined). The main survey for spatially resolved binaries in PNe was carried out by Ciardullo et al. (1999).

- **Astrometric binaries** – the presence of a companion star is inferred by precise measurements of change in stellar position over a period of time, detected by a 'wobble' in its proper motion. Here, the companion may have a low surface brightness that is obscured by the higher surface brightness of the observable star, or the companion may be e.g. a neutron star of lower luminosity. Examples of astrometric binaries include GJ 802AB that has a likely brown dwarf companion (Pravdo, Shaklan & Lloyd 2005; Lloyd et al. 2006; Ireland et al. 2008), and Sirius AB (Bessel 1844; van Albada-van Dien 1977; Liebert et al. 2005).

- **Spectroscopic binaries** – detected through a periodic shift in the position of the spectral lines of the two stellar components due to the Doppler effect. Here,

the spectral lines of each component shift towards the blue as they approach the observer, then towards the red as they recede away during their orbits about the common centre of mass. In these systems, the separation between the stars is usually very small (and so are unresolvable visually) and as a result the orbital velocity is very high. Measuring the Doppler shift as a function of time allows us to plot a curve of the radial velocity, and from this the orbital period of the system can be determined. In a circular orbit, the resultant curve is a sine curve; however, since the orbits in a binary are often highly elliptical, the shape of the curve depends on both the eccentricity of the ellipse and the inclination of the binary plane to the line of sight. If the orbit of the system is perpendicular to the line of sight, then no spectroscopic shift or radial velocity can be determined. The inclination of the orbital plane cannot be inferred from spectroscopy, and so only the stellar mass ratio can be determined from double-lined spectroscopic binaries (where spectral lines from both stars can be identified).

- **Eclipsing binaries** – detected through periodic variations in the observed light emanating from the system, as one star passes in front of the other during its orbit - the smaller the orbit, the greater the chance of detecting an eclipse. The inclination of the orbital plane of the binary can be ascertained from the resultant light curve, and must be close to 90° to the line of sight in order for an eclipse to occur. The shape of the light curve, in conjunction with knowing the radial velocity components, allows for the determination of the stellar mass ratio, radii and effective temperatures of the system.

As such, a short summary of the detection methods for these binary types is as follows:

- **Direct CCD imaging** – possible for resolvable binaries in wider orbits. Direct imaging can also reveal photometric variability.

- **Composite spectra** – spectrum contains signatures of two stars. An optically-faint hot star has cooler component (as is the case for LoTr 1 – see Chapter 4).

- **Photometric variability** – periodic light variability due to either one star eclipsing the other, irradiation effects (where the central star heats the companion as it rotates), or ellipsoidal variations (where the companion expands and contracts due to gravitational effects caused by the primary). This method is used for short period binaries, as these effects occur when the two stars are eclipsing and/or when there is a small orbital separation (as is the case for PN G033.8+01.5 – see Chapter 5).

- **Radial velocity variations** – tracing of the orbital motions of the stars about a common centre of mass towards and away from the observer, to detect Doppler shifting through changes in the stellar spectra. Used for long period binaries.

1.3.4 The binary fraction and associated biases

The central stars of PNe tend to be very faint and often only have a few, broad absorption lines that are often contaminated by emission lines from the nebula itself. Surveys based on photometric variability tend to be biased against wide binaries within PNe due to the fact that as orbital separations increase, irradiation effects, ellipsoidal variability and the chances of an eclipse become drastically reduced and therefore detection is much less likely. Bond (2000) believes this to be the reason why all the binaries detected within his survey had periods smaller than ∼3 d, and concludes that the observed binary fraction of 10–15% should in fact be treated as a lower limit due to being inclusive only of close binary systems. Miszalski et al. (2009a) calculated the close binary fraction within PNe to be in the region of 12–21%, not that much higher than what Bond predicted. Miszalski et al. (2009a) observationally confirmed the prediction of De Marco, Hillwig & Smith (2008) from irradiation models that variability surveys should be biased against systems of periods over ∼2 weeks (i.e. systems with periods up to this value should theoretically have been observed), concluding that either the detection bias is large, or that the production of binaries with such periods through CE interaction is truly rare (see Sec. 1.3.1 above). A comparison with MS

stars gives a close binary fraction of 5–7% at similar separations (Duquennoy & Mayor 1991; Raghavan et al. 2010; De Marco et al. 2013).

Radial velocity surveys should show a similar binary fraction to photometric variability surveys. However, wind variability causes a bias in the results as it can give the appearance of a spectroscopic line shift in the spectra that one would normally attribute to radial velocity effects. This is particularly common for those PNe that possess a luminous central star (De Marco et al. 2004; Afšar & Bond 2005). It is therefore exceedingly difficult to detect all but the most extreme CSPNe, and so intrinsically dimmer central stars would have to be targeted to use this method as the wind will have subsided, thus giving rise to a selection bias in the form of stellar luminosity.

The implication from this is that up to 88% of all aspherical PNe have to be explained by a mechanism other than a binary-induced CE interaction (De Marco 2009). Some PN may have been shaped by a CE interaction that resulted in a merger, or from an interaction with a wider binary companion that avoided the CE phase entirely (see Sec. 1.3.2). With regards to the latter, 30% of post-AGB stars are spectroscopic binaries with periods between 100–1500 d, and assuming that all post-AGB stars observed will form a PN, then ~30% of all CSPNe should be binaries with periods in that range. This would mean that the short-to-intermediate period binary fraction is actually at least 42-61% – much higher than the observed fraction.

The detected companions in such surveys are mainly MS stars. Because WDs are optically faint, they are often overlooked unless observations are also taken that would allow the detection of a UV excess that would point to its existence. The WD binary fraction of 30–40% is in line with the assumption that all WDs are derived from an initial mass range of 0.8–8 $M_{\odot}$ and therefore is a true reflection of the MS binary fraction (Douchin et al. 2013). Giant stars in binary systems undergo a more rapid evolution, and so the chances of detecting such a companion compared to a MS star are greatly reduced. The detection of close binaries ideally requires bright central stars and faint nebulae, which could in principle be found in systems where the central star evolves much slower than the surrounding nebula, i.e. the nebula has had time

to expand whilst the star remains relatively cool. This selection favours low mass CSPNe, leading to a bias against those that are more massive. However, if the mass of the remnant is too low, as would be the case if the star evolved too rapidly early on the AGB, it will evolve too slowly to ionize the PN before it has completely dispersed. Indeed, this could explain why some post-AGB binaries are detected without a PN (Zijlstra 2007). If a post-AGB binary is observed within a PN, it is highly likely that it is not the result of a CE interaction, as implied by their eccentric orbits.

In theory, the most effective way to detect companions would be to use near-IR excess surveys since they can be detected at arbitrary distances. However, the bias here lies with the fact that the central AGB stars are very luminous, appear bright across the spectrum and are surrounded by dusty envelopes, making it very difficult to directly detect any fainter, cooler companions (Sahai 2009). Post-AGB binaries in very wide systems also tend to not have detectable companions as their luminosity is too great. De Marco et al. (2013) recently determined a binary fraction of 30% in the I-band for a sample of 27 CSPNe, and 54% in J-band for a sample of 11 CSPNe. This fraction is in line with that of Frew & Parker (2007) who stated 52–58%. However, this fraction cannot account for late M companions as they are too faint to be detected in the near-IR regime, while it might include objects too wide to have influenced PN shaping. The survey also does not account for resolved binaries, which are instead absorbed into the MS binary fraction (Douchin et al. 2013). Taking this into account, De Marco et al. (2013) predict a debiased binary fraction of 70–100% for aspherical CSPNe; however, there is still a large uncertainty on this value due to the use of small number statistics.

1.4 This thesis

For this thesis, I am initially going to be presenting a spectroscopic study of the morphology and kinematics of a known short period bCSPN, HaTr 4, with the aim of confirming that the binary has played a role in its shaping. This will be followed by the spectroscopic analysis of a suspected intermediate period bCSPN, LoTr 1, in comparison to two other known, kinematically similar PNe (Abell 70 and WeBo 1) with the aim of determining whether it possesses a Ba star and how this affects our understanding of mass transfer mechanisms. Finally, the photometric analysis of a PN from the Paranal Observatory Project for Imaging Planetary Nebulae (POPIPlaN) project will be presented, with the aim of determining whether it possesses binarity and if so, what the stellar parameters are and how it relates to the surrounding PN.

By focusing on slightly different areas for each project, an overall view can be gained of how the interaction of stars within a binary system influences both its own evolution, and that of the PN in terms of its the morphology, kinematics and composition.

In Chapter 2, I outline the main techniques of observation, reduction and analyses performed on the data presented in this thesis.

In Chapter 3, I present the spectroscopic data analysis of the close binary CSPN, HaTr 4

In Chapter 4, I present the spectroscopic data analysis of the suspected intermediate period binary CSPN, LoTr 1, alongside two similar PNe, Abell 70 and WeBo 1

In Chapter 5, I present the photometric data analysis of PN G-003.8+01.5.

Finally, a summary of the main conclusions and suggested future work are detailed in Chapter 6.

2

Techniques of Observation, Reduction, and the Analysis of Data

In this chapter, I explain the 'theory behind the practice' of the techniques used to observe and analyse the acquired data, specifically referring to both nebular / stellar spectroscopy and stellar photometry. All of the data presented in this thesis undergo the same basic data reduction processes - here, I outline *why* we reduce the data, what programs are used for this, and how the routines within the program operate.

2.1 Spectroscopy

There are five main spectrographs used in the acquisition of the data presented in this thesis.

- FORS2 – The FOcal Reducer and low dispersion Spectrograph v.2, a multi-mode instrument capable of both imaging and spectroscopy. It is found at the Cassegrain focus of the 8.2m Very Large Telescope (VLT) Unit (UT) 1, based at the ESO-Paranal Observatory, Chile (Appenzeller et al. 1998).

- EMMI – The ESO Multi-Mode Instrument, a now-decommissioned echelle spectrograph that was located at the Nasmyth B focus of the 3.58m New Technology Telescope NTT based at the ESO-La Silla Observatory, Chile (Dekker, Delabre & Dodorico 1986).

- UVES – The Ultraviolet and Visual Echelle Spectrograph, found at the Nasmyth B focus of the VLT-UT2 (Dekker et al. 2000).

- UCLES – The University College London Echelle Spectrograph, a Coudé echelle spectrograph located at the Coudé focus of the 3.9m Anglo-Australian Telescope (AAT; (Ryan & Fish 1995)).

- MES – The Manchester Echelle Spectrograph, currently mounted at the Cassegrain focus of the 2.1m San Pedro Martír (SPM) telescope at the Instituto de Astronomía Universidad Nacional Autónoma de Mexico (Meaburn et al. 2003; see Fig. 2.1).

Spectroscopy, in its most basic form, is the accurate measurement of the intensity of emitted light as a function of wavelength with a spectral resolution that allows us to determine features intrinsic to the astronomical object that one cannot gain from imagery and photometry alone. The aim behind using spectroscopy for observations of PNe is to gain essential kinematical information that requires data to be obtained in two dimensions (2D) in terms of both spatial and spectral positioning of the object in question. Due to the highly extended nature of nebular emission, the use of a long slit is required in order to ensure that emission from features typically found far out from the central star - for example, knots, jets and halos - are not overlooked. For the data presented in this thesis, the long slit lengths are 330 arcsec for NTT-EMMI, 30 arcsec for UVES, 408 arcsec for FORS2, 56 arcsec for UCLES, and 300 arcsec for MES. By placing such a slit along several nebular axes, a three-dimensional (3D) picture can begin to be built up in the form of position-velocity (PV) arrays that allows us to observe both its intrinsic morphology and how it relates to its central star system.

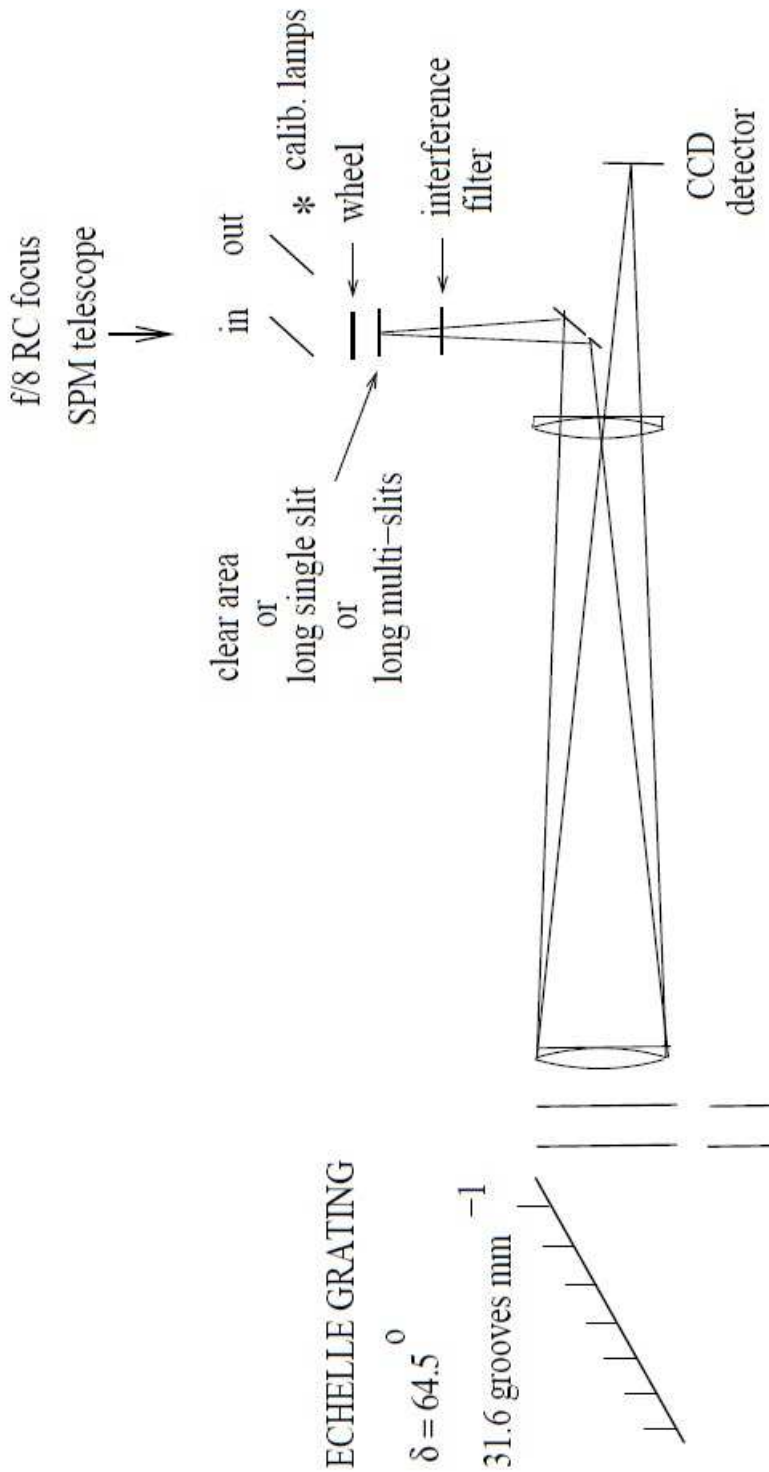

Figure 2.1: The optical setup of the SPM-MES spectrograph. Image taken from Meaburn et al. (2003).

The standard settings for this are to use a high resolution spectrograph utilising a slit width of around 1 arcsec. Stellar spectroscopy differs from spectroscopy performed on a nebulous region due to being a point source, rather than an extended feature. In this case, only one-dimensional (1D) spectral data are required in order to determine stellar parameters such as luminosity (L), effective temperature ($T_{\rm eff}$), and elemental abundances used in classifying the central star.

The basic set-up of a spectrograph is as follows: The incoming light is focused by the telescope of diameter D_{tel}, focal length F_{tel} and focal ratio f_{tel} onto a narrow slit of width ω and height h that sits in the focal plane. After the light passes through the slit, it is guided through an interference filter to remove unwanted orders and the diverging light is tunnelled into a parallel beam by a collimator (a system of lenses or mirrors of diameter d_{col}, focal length F_{col} and focal ratio f_{col}). By having the collimator designed as an off-axis parabaloid, it can simultaneously collimate the beam and direct the light towards a disperser - a 'diffraction grating' that disperses the light (by reflection or transmission) from a parallel beam into its constituent spectral components. Finally, a camera of diameter d_{cam}, focal length F_{cam} and focal ratio f_{cam}, focuses the spectrum onto the CCD detector (Wagner 1992).

Here, I provide a brief description of the main components making up a spectrograph.

Slit

The most important aspects of a spectrograph are its resolution (the ability to differentiate close spectral features) and throughput (how much of the incoming light falls on the detector, i.e. the ability to detect and record spectra of faint objects, or weak spectral features). The purpose of the slit is to isolate the region of interest in the sky whilst limiting contamination from background sources and excess noise, and to provide stable spectral resolution.

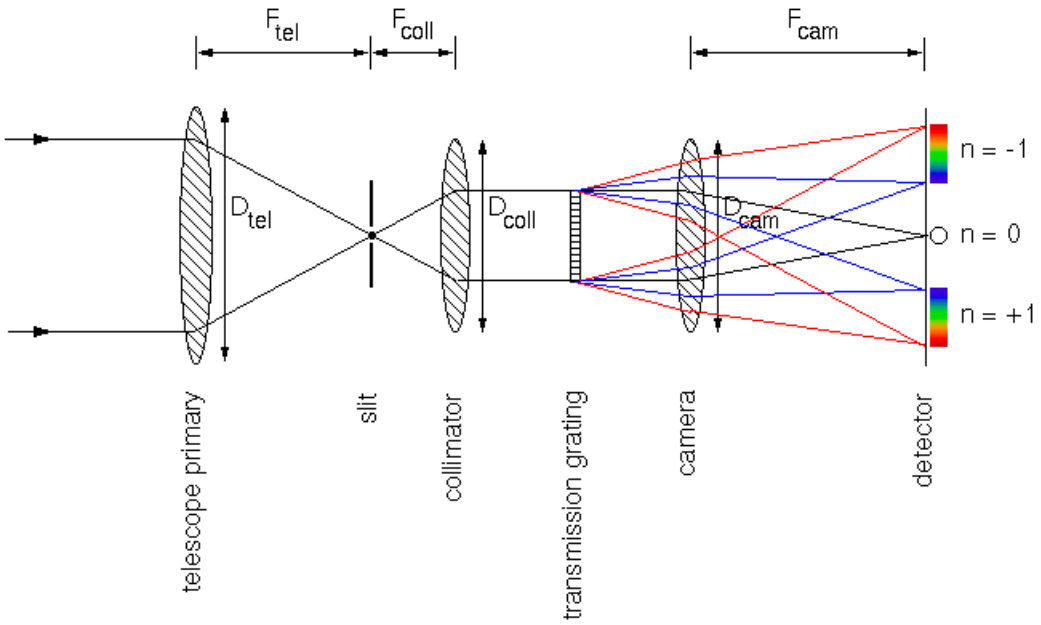

Figure 2.2: Diagram to show a standard spectrograph setup using a transmission grating. Taken from V. Dhillon's (University of Sheffield) 'astronomical techniques' lecture notes.

The spectral resolution is defined as:

$$R = \frac{\lambda}{\Delta\lambda} \tag{2.1}$$

where $\Delta\lambda$ is the difference between two consecutive spectral lines of around wavelength λ. The optimal value for R occurs when the FWHM of an unresolved spectral line covers ~ 2 pixels on the detector.

The slit width subtends an angle of $\theta_\omega = \frac{\omega}{F_{tel}}$ projected on the sky, and so the slit width projected onto the CCD is:

$$\omega' = \omega\, M = \frac{\theta_\omega\, f_{tel}\, D_{tel}\, F_{cam}}{F_{col}} \tag{2.2}$$

where M is magnification, F_{cam}/F_{col} (Howell 2006).

Since the focal length of a collimator is simply product of its diameter and focal

ratio, this equation can be reduced to:

$$\omega' = \frac{\theta_\omega \; f \; D_{tel} \; F_{cam}}{f_{col} \; d_{col}} \tag{2.3}$$

As the camera focal ratio is defined by F_{cam} divided by beam diameter d_{col}, the projected slit width becomes:

$$\omega' = \theta_{omega} \; D_{tel} \; f_{cam} \tag{2.4}$$

In the absence of a slit, the resolution is determined by the seeing disc of the object which can vary considerably over the course of a night. While R increases as ω decreases, the fact that the seeing disc of the object is nearly always considerably wider than the slit means that the smaller ω is, the more limited the light throughput becomes and as a result the smaller the signal-to-noise ratio (S/N) acquired. For objects that are already faint or have weak spectral features, this can seriously limit the ability to gain good measurements. For this reason, there is a trade-off between resolution and throughput that must be taken into consideration when initially choosing a value for ω.

Interference filter

CCDs typically have sensitivity extending from 3000–10 000Å, and so overlapping orders can present a problem with spectrographic data. This is solved by inserting an interference filter after the slit that allows light in a particular spectral range to be transmitted through to the collimator, whilst reflecting the rest. In certain cases, a dichroic filter is used to split the incoming light into two specific, broader wavelength ranges. A dichroic filter is a bandpass filter composed of several different dielectric layers, each with a different refractive index that subsequently only allows desired wavelengths and orders to pass through (‘passband’ frequencies), whilst excluding the rest (‘stopband’ frequencies). For example, light entering UVES is directed into one of two ‘arms’ (UV to Blue, or Visual to Red) within the instrument meaning that these

arms can be utilised separately, or simultaneously with the use of a dichroic beam splitter.

Table 2.1: Table showing the accessible wavelength ranges for different UVES configurations, with and without the dichroic filter.

Instrument mode	**Accessible λ range (nm)**
Blue arm	300-500
Red arm	420-1100
Dichroic # 1	300-400, 500-1100
Dichroic #2	300-500, 600-1100

Since dichroic filters reflect unwanted light rather than absorb it, they tend to be more thermally stable than other filters.

Collimator

The collimator tunnels diverging light into a parallel beam and subsequently directs the beam towards the grating. By the grating equation (see Eq. [2.5]), the diverging light of varying θ_i results in a varying angle of diffraction, θ_{dif}, for a fixed wavelength, and so imaging on the detector would occur at several different positions causing the spectrum to blur. To avoid a great loss of efficiency of the spectrograph, f_{col} should be equal to f_{tel} and be positioned a distance of F_{tel} away from the telescope focal plane.

Grating

A grating is used as the dispersing element in a typical spectrograph, ruled with a number of grooves mm^{-1} (also known as the 'groove density', usually of order 100-1000 grooves mm^{-1}) which is equal to the inverse of the groove spacing, d. The greater the groove density, the higher the dispersion, and as a result the larger the spectral range. The size of d must be of an order comparable to the desired wavelength, and by

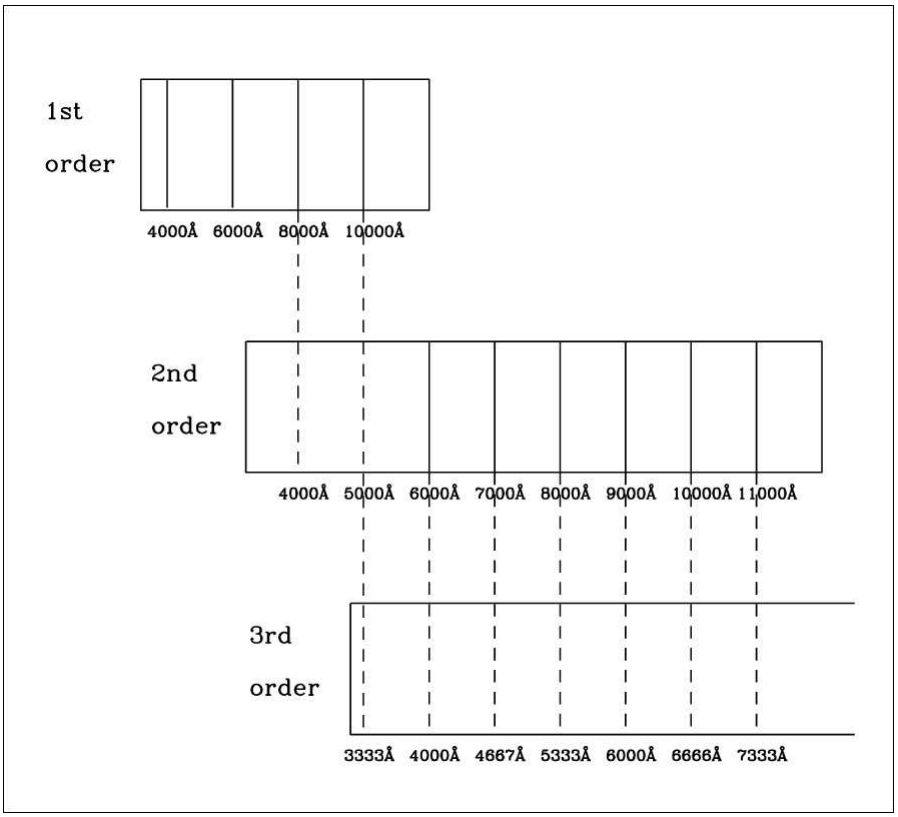

Figure 2.3: Figure to show example of overlapping orders and associated wavelengths. Image taken from Massey et al. (2000).

the grating equation (Eq. [2.5]) the spectral range covered by a grating is dependent on the value of d and the spectral order, n. To obtain dispersion over a wider wavelength range, a prism is used in place of the grating.

The observed wavelength of light seen depends on both θ_i and θ_{dif}, and this relationship is summarised with the grating equation:

$$n\lambda = d(\sin\theta_i + \sin\theta_{dif}) \tag{2.5}$$

where n is the integer spectral order number, and λ is the specified wavelength. The angular dispersion, θ_{disp}, of a given order and wavelength can be found by differentiating the grating equation:

$$\frac{\delta\theta}{\delta\lambda} = \frac{n}{d\cos\theta_{disp}} \tag{2.6}$$

for a given value of θ_i (Massey & Hanson 2013).

A conventional grating spectrograph must be used in low order ($n \sim 1$ or 2) to avoid overlapping wavelengths from different orders. These spectrographs are designed to be used with a small θ_i so that the light both enters and leaves along the grating normal, and the only way of achieving high dispersion is by using a high groove density (i.e. decrease d).

Note from the above that:

$$\frac{m}{d\theta_i} = \frac{2\sin\theta_i}{\lambda} \tag{2.7}$$

in the Littrow condition. The Littrow condition is defined as θ_i for the incoming light being approximate to the grating normal - in this case, the light undergoes auto-collimation, in that the incident and diffracted light follow the same path at a specific wavelength (the blaze wavelength, λ_B) to maximise grating efficiency for a particular order above the zeroth order. This is achieved by setting the grooves within such a 'blaze grating' to a specific blaze angle, θ_B (the angle between the grating surface and the reflecting grooves - see Fig. 2.4).

Therefore, if θ_i is very low:

$$\tan\theta_i \ \sin\theta_i \sim \theta_i \tag{2.8}$$

and the angular dispersion:

$$\frac{\delta\theta}{\delta\lambda} \sim \frac{n}{d} \tag{2.9}$$

Alternatively, if θ_i is very high, one can achieve high dispersion with a lower groove density by operating in a higher order. This is indeed how echelle spectrographs are designed to work, with typically $\tan\theta \sim 2$ or greater. A typical echelle grating might have ~ 80 grooves mm^{-1}, so, $d \sim 25\lambda$ or so for optical light, and n must be of order 50.

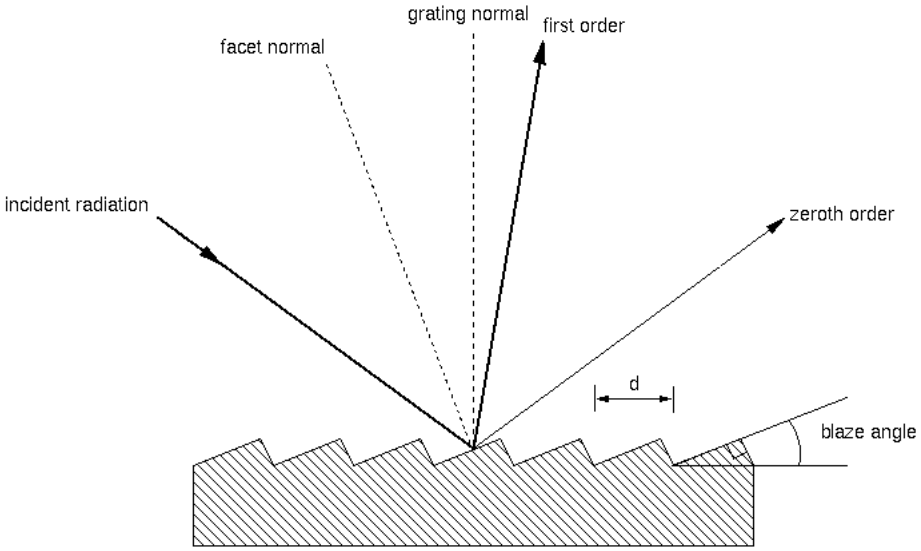

Figure 2.4: Diagram to show a standard blaze grating. Image taken from Palmer, Loewen & Thermo (1994).

2.1.1 Echelle Spectroscopy

In the case of echelle spectroscopy, the basic setup is the same as mentioned above, but a blazed grating, designed to operate in higher orders ($n \sim$ 50-150) with a large θ_i typically greater than 60°, is used as default. With this, high dispersion can be achieved with a lower groove density on the grating. The large blaze angle means that a relatively wide slit can be used, and so provide a better throughput at a given resolution, i.e. echelle spectroscopy provides high resolution spectroscopy whilst maintaining good spectral coverage. As previously mentioned, working in higher orders can cause wavelengths to overlap, with higher orders causing greater overlap (see Fig. 2.3). This can be solved by introducing a second dispersive element in the form of a prism or another grating after the blazed grating to act as a 'cross-disperser' and separate the orders. The resultant spectrum is similar to that shown in Fig. 2.12 (a), consisting of 'stripes' that cover a specific wavelength range that have a slight overlap with adjacent orders.

Overlapping wavelengths in an undispersed echelle spectrum are related by:

$$n_1 W_1 = n_2 W_2 = ... = n_i W_i \tag{2.10}$$

where n_i are the integer order numbers, and W_i are the wavelengths. The wavelengths occupy similar positions in adjacent orders (usually concentrated in one or two other orders), but at different intensities as each order has its own blaze profile (Ryan & Fish 1995).

2.2 Time-Series Aperture Photometry

Time-series photometry is a technique whereby an object is observed over a given period of time in order to search for evidence of variability. The variability is observed simply as a change in the apparent magnitude (derived from the observed flux) of the target. This change can be a result of several different physical effects on the star:

Intrinsic variables

- Pulsating variables – these stars possess intrinsic ellipsoidal variations that cause the star to radially expand and contract, thus affecting the size and therefore luminosity of the object, e.g. Cepheid, RR Lyrae stars, and Delta Scuti stars.
- Cataclysmic variables – an eruption occurs with a dramatic increase in the brightness of the object, after which the apparent magnitude drops again, e.g. novae and dwarf novae (since it is not a recurring event, a supernova (SN) is often classified as a ‘catastrophic variable’).

Extrinsic variables

- Eclipsing binary systems – when the orbital plane of the binary is close to the line of sight of the observer, the apparent magnitude drops as one star eclipses the other.

- Ellipsoidal variation due to binary systems – in a close binary system, distortion of the stellar envelopes can occur due to effects of mutual gravitation during its orbit.

- Irradiation (reflection) effects – in a binary system, a hot star illuminates one surface of a cooler companion, increasing the surface temperature and therefore the luminosity of the companion on the irradiated side.

- Rotation effects – cool spots on the stellar surface cause a slight decrease in magnitude as the surface points towards the observer, and increases again as the star rotates causing the cool surface to point away. Alternatively the star's shape may be naturally ellipsoidal, causing brightness variations as it rotates.

There are two main techniques behind time-series photometry that can be employed to determine what causes the suspected variability of the target:

- Differential photometry – measuring how the apparent magnitude (i.e. the raw flux) of the target changes over time in comparison to another star in the local field of view to create a lightcurve. By simultaneously observing a number of comparison stars alongside the target, it is possible to account for errors largely due to non-photometric conditions.

- Absolute photometry – determining the apparent magnitude of an object on a standard photometric system. The observations of the target are then compared with other absolute photometric measurements obtained with different telescopes and instruments. On top of the standard corrections for atmospheric extinction, etc. mentioned above, for absolute photometry it is also necessary to correct for differences between the effective passband through which the target was observed and that used to define the standard photometric system. This is typically carried out by observing both the target and several photometric standard stars in different filters.

For the work presented in this thesis, we chose to carry out differential photometry to produce the lightcurve and hence determine the periodicity of the target due to the high precision to which it can be measured. This is then followed by performing absolute photometry to put the derived stellar magnitudes of the system in absolute, rather than relative, terms. Differential photometry is performed using a 'stellar aperture' and a 'sky annulus'. Here, observed counts (flux) are summed within a circular aperture centered around the target star on a given image. The radius of the stellar aperture is typically taken to be 1–3 times the full width at half maximum (FWHM) of the stellar point source function (PSF), and usually the same aperture is used for all images to be included in the analysis. However, because noise increases with aperture size as the flux tails off in the 'wings' of the stellar profile, it is important to find an optimum radius that would allow the greatest S/N whilst minimising the background contamination, and subsequently minimising the overall error on the results. Too large an aperture, and there will be too much contamination from the background. Too small an aperture, however, would not allow for image-to-image variations in the stellar PSF due to e.g. changes in the nightly seeing conditions, and flux will be lost. To determine what the optimum aperture radius is, it is possible to plot the radial profile of the star and look at its 'curve of growth'. If one plots aperture radius versus counts, there is an initial steep increase before flattening out and eventually losing linearity. The point at where the curve just starts to level out (i.e. the point at which the stellar flux starts to merge into that of the background) can be taken to be the optimum aperture radius.

Once the optimum aperture radius has been determined, the next step is to perform sky subtraction by positioning an annulus around the stellar aperture (typically with a 'buffer' region between the two) and summing the raw counts (see Fig. 2.5). The mean counts per pixel within the sky annulus are then subtracted from the overall flux to ensure that the value used is representative of the stellar flux only. A typical radius for the sky annulus is 3 x width of the stellar aperture to ensure a good sample of background is acquired.

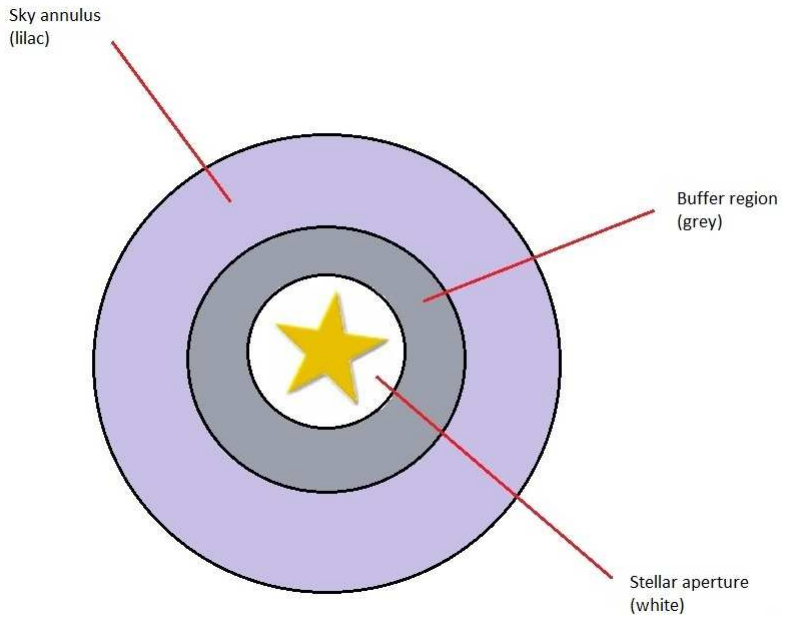

Figure 2.5: A typical set-up for aperture photometry

An instrumental magnitude, m_i, of the star can then be determined from the equation:

$$m_i = -2.5 \times log\left(\frac{F}{t_{\text{exp}}}\right) + 25 \tag{2.11}$$

where F is the sky subtracted flux of the target in counts, t_{exp} is the exposure time of the image, and 25 is an arbitrary constant that ensures all values of m_i remain positive.

To perform differential photometry, this process is carried out for both the target and a selection of comparison stars. By plotting heliocentric Julian date (HJD) against $m_{comparison1} - m_{comparison2}$, it is possible to see if the selected comparison stars have intrinsic variability, as well as allowing any variation due to seeing to be visualised that can then be directly compared to the apparent variability of the target star. One comparison star is then selected to subtract against the m_i of the target star to give a differential magnitude. Plotted against HJD, this then gives the initial light curve, and is the first pointer towards evidence of variability.

The orbital period of the lightcurve can be estimated using a dedicated time-series program such as 04. By inputting a data set containing HJD and the previously-

determined differential magnitudes, 04 aims to find sinusoidal functions that are approximate to the observed lightcurve when several are combined. A Fourier analysis algorithm is used to extract individual, dominant frequencies (equivalent to $1/P$, where P is the period) detected within the input data set and outputs to a spectral window of frequency versus the square of the amplitude (i.e. the power). The analysis is then followed up by refining the frequencies using a least-squares fit. The Fourier analysis alone cannot be used to solve the problem as it is only a single-frequency method, and therefore several frequencies must be extracted. For each frequency, an associated amplitude and phase are calculated along with the residuals and a zero-point. It is then possible to see if the residuals possess any further periodicity by applying another Fourier analysis and extracting a new frequency. This second frequency is then used along with the first for the next fit to improve the residuals. By 'Nyquist's Theorem', the smallest period that can be measured by P 04 has a period of twice the sampling timescale, i.e. the Nyquist frequency, $N_f = 1/2t$ and so shorter periods will not be well accounted for. P 04 automatically determines N_f, and suggests that the Fourier analysis should cease at this value.

This method is susceptible to a problem with 'aliasing', and so care must be taken when determining the peaks in the Fourier spectrum - 04 does not account for gaps in the data set very well (i.e. when there is uneven sampling), and as such the program will try to fit maxima on existing points, and minima where there are none. Due to the cyclical nature of the observations, this will also subsequently result in peaks being produced at multiples of the frequency in question ($2f$, $3f$, etc.). The result is that it can create sinusoidal fits that look viable, but are in fact spurious and can deter from assigning a true period to the data.

Once a period of variability has been established, it is possible to determine at what phase (ϕ) of the cycle any given data point lies - the data are 'phase-folded' to show an entire cycle of variability. Phase-folding the data is done using the following equation:

$$\phi = \frac{t - t_0}{P} \tag{2.12}$$

where t is the time each data point is observed (usually in terms of days, HJD - 2456446), t_0 is a zero-point time (i.e. the point in the lightcurve where $\phi = 0$ will lie), and P is the period.

By varying P and using the estimates gained from the Fourier analysis within P - 04 as a starting point, it is possible to acquire a best-fit lightcurve and subsequently refine the value for the period of the central star system. Once the period has been determined, it is desirable to use a modelling program such as to ascertain what the best-fit stellar parameters are in order to recreate such a lightcurve and allow us to determine with more certainty whether the variability is due to an eclipsing binary system, or if ellipsoidal and irradiation effects are the more dominant factor.

is an inverse-modelling program, whereby a generalised Wilson-Devinney method of solution-convergence is used to alter and assess free parameters in order to reproduce the observed lightcurve. Conventionally, the primary star is defined as the brighter of the two (and therefore usually the more massive, though this cannot necessarily be assumed), and the secondary star is the fainter. Within the program, however, the primary star is taken to be that which is *eclipsing* first. A standard Roche lobe geometry for the binary system is assumed. Six free parameters are mandatory: mass ratio (q), inclination of the binary system ($i°$), $T_{\rm eff}$ of the primary and secondary stars, and the Roche lobe 'fill factor' (RLFF) of each star. Three other free parameters that were altered for the work presented in Ch. 5 are the third light contribution, absolute mass of the system, and absolute distance (the separation between the primary and secondary). By inputting values for each of these parameters into , the program automatically converges the result to a best fit to the observed data. The observed data read in by must be edited so that $\phi = 0$ corresponds to the bottom of the primary eclipse.

For flux calibration purposes, the aperture photometry must be repeated for a selection of photometric standard stars at a variety of airmasses. By observing these standards in the Bessel B, V, R and I filters it is possible to determine the magnitudes and therefore colour indices across these bands, and subsequently apply a correction

factor to the target in order to derive its magnitudes and colours using absolute photometry.

The instrumental magnitude acquired from Eq. [2.11] must be corrected for both the target and the standard stars to account for local extinction at the observatory site (k), and air mass at the time of observation (X):

$$m_{corr} = m_i - (k \times X) \tag{2.13}$$

A zero-point magnitude (i.e. a correction factor) must be determined by taking the difference between a given catalogue magnitude and the calculated value of m_{corr} for each standard star used, which is then applied by addition to the m_{corr} of the target star.

Once all values of m_{corr} had been determined using Eq. [2.13] for both the target and standards, a colour-correction factor needs to be applied. This is determined using observations of standard stars and the equation:

$$m_{std} = (\epsilon \times colour) + C \tag{2.14}$$

where ϵ is the colour-correction factor, 'colour' refers to the colour indices ($B - V$), ($V - R$), and ($B - I$), and C is a linear coefficient.

By applying a best-fit line to a colour-magnitude diagram, created by plotting the calculated colour term against m_{corr} for a particular filter, it is possible to derive the coefficients shown in Eq. [2.14] required to calculate the final corrected magnitude of the target in B, V, R and I. The slope of the fit represents ϵ, and the y-intercept represents C. This then gives the desired overall correction factor to apply to the target data:

$$m_o = m_{corr} - (\epsilon \times colour) - C \tag{2.15}$$

where m_o is the final corrected instrumental (apparent) magnitude of the object.

The colour index is predominantly determined by $T_{\rm eff}$ for the star. Since hotter stars radiate more at shorter wavelengths, the V band magnitude tends to be low relative to

that in *B*, therefore the ($B - V$) colour index is large compared to that of cooler stars (Vorontsov 2010).

2.3 Basic data reduction

The aim of data reduction is to remove any artifacts generated by either the telescope or the instrument (the 'instrumental signature') that could contaminate the acquired target data. Effects such as pixel-to-pixel sensitivity variation, interfering cosmic rays, temperature fluctuations, and simple non-uniform illumination on the CCD can all have an effect on the resultant image, and need to be accounted for before effective analysis of the data can take place. Accurate calibration of the data is also required in order to extract the useful information contained within the raw spectra.

2.3.1 Preliminary data reduction

The following basic CCD data reduction techniques have been applied to all data presented in this thesis, both nebular and stellar, using routines found within the
data reduction package

Bias subtraction

It is necessary to put each acquired data frame through the process of 'debiasing'. A 'bias frame' is simply a zero-second exposure (i.e. a straight read-out of the CCD with the shutter closed), that is taken to account for variation in the offset level of each pixel. The bias level is a deliberate electronic offset added to the received signal to ensure that the Analogue-to-Digital Converter (ADC) always receives a positive value. The offset level generally follows a pattern across the CCD, and so a 'master bias' frame (an average of several bias frames taken at the start of the night) can be subtracted from each data frame acquired to account for this (see Fig. 2.6). Simple subtraction of two frames *increases* random noise in the resulting image by a factor of around $\sqrt{2}$; however, by subtracting the average of several frames using a median combination – whereby the median value for each pixel in the original frames is used rather than a simple average, and any pixels falling outside that value are rejected – one simultaneously significantly reduces the readout noise by a factor $\sqrt{N}$ (where N is the

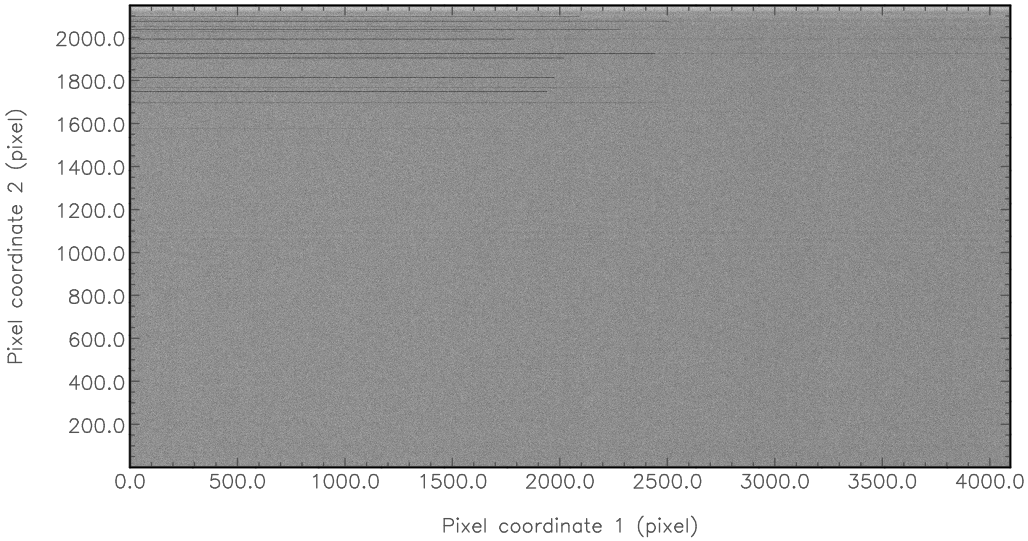

Figure 2.6: An example of a master bias frame from VLT-UVES, created using package, .

number of frames used in the median combination process), and allows the removal of random cosmic ray hits that may have been missed in the cleaning process (see Sec. 2.3.1 below).

The routines and were used to create the master bias frames and subsequently subtract it from the data frames.

Overscan

The bias level can change over the course of the night, and so the true bias may be slightly different to what the master bias accounts for. These differences can be estimated using 'overscan regions' (otherwise known as 'bias strips') - pixels in the final frame that are read out, but are not part of the exposed image (see Fig. 2.7 for an example). The mean level of the pixels in the overscan region gives a measure of the average bias level at the time of observation introduced by the CCD, i.e. the overscan level. Once this level is deduced, it is removed from all pixels in the image. The overscan regions are then trimmed from the frame to leave only the bias-corrected data.

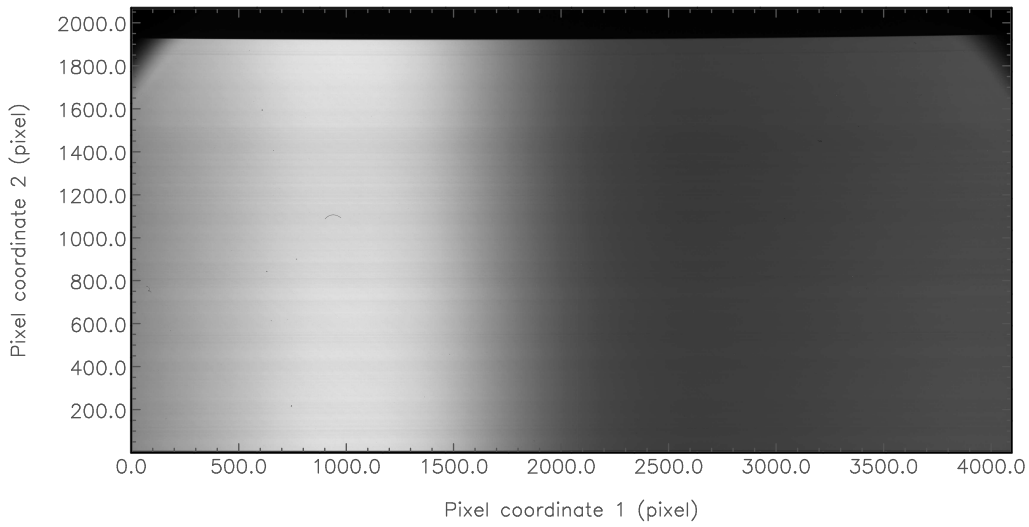

Figure 2.7: An example of a master flat frame for nebular data from NTT-EFOSC2, created using package, . An overscan region can be seen to the top of the image.

Dark current

CCDs are sensitive to temperature, and the dark current represents the thermal response of each pixel in the frame - it is possible for some electrons to already have a high enough energy to activate a CCD pixel without the need for input photons, and so excess charge accumulates across the chip. By cooling the CCD with liquid nitrogen, the dark current is effectively reduced to zero. Generally, if dark current is subtracted from the data, it is not necessary to perform bias subtraction as well as the bias is already contained within the dark exposures. Since all instruments used to acquire the data in this thesis do have their CCDs cooled by liquid nitrogen, only bias frames were necessary.

Cosmic ray cleaning

The program and its (non-interactive) and (interactive) routines were used to remove cosmic ray ‘hits’ and bad columns/rows on the CCD detector. When a cosmic ray hits the CCD its high energy liberates electrons intrinsic to the chip, appearing as either a cluster of bright pixels randomly positioned across the CCD or as a bright line where the cosmic ray has skimmed across the detector at an

angle (see Fig. 2.8a). automatically detects and removes the cosmic ray hits, by replacing the bad pixels with a value interpolated from the surrounding pixels in either the x- or y-direction (i.e. in rows or columns), or the program automatically chooses an interpolation direction based on which has the smallest residuals (see Fig. 2.8b). The cosmic ray search algorithm looks at every pixel in the image and compares its value with the average value of the four nearest surrounding pixels. To be regarded as a cosmic ray, the pixel must exceed that average by an amount greater than a value dictated by the algorithm multiplied by the square root of the average. To differentiate random cosmic ray hits from stars, a 'sharpness' test can be carried out. Here, the ratio of the peak of the central region of the cosmic ray to the peak value of its wings is measured. For stars, the wings tend to be a significant fraction of the peak height, whereas cosmic rays generally have much sharper edges.

is usually used as a follow-up to to patch up any bad pixels that were missed in the initial cleaning process.

2.3.2 Reduction of nebular spectroscopic data

The following steps for further reducing the nebular data presented in this thesis were carried out using routines found within the data reduction package.

Flat fielding

By flat fielding the acquired data frames, variation in the sensitivity of each pixel to the arriving photons can be accounted for. This variation could be due to foreign objects on the detector and filters casting shadows onto the chip, non-homogeneity of the quantum efficiency (QE) of the CCD (the linear response of each pixel with photon hits), or vignetting (optical response). For sky flats, a known 'empty' field of sky is observed at twilight across the wavelength range to be utilised for that night of observation to create a uniformly-illuminated exposure. Several exposures are taken in each filter, and then each frame is bias-subtracted and averaged together to account for

noise, bad pixels and unwanted on-sky objects (the exposures are usually dithered to be able to effectively remove these objects when averaged). The subsequent data frames are then divided by the resultant 'master flat' (see Fig. 2.7). Sky flats are preferred over dome flats (flat field frames taken by e.g. pointing the telescope at a blank piece of dome wall) as there are less systematics to affect the image.

The routines and were used where necessary. initially 'cleans' the data before creating the master flat frame by using a 'box filter' (a rectangular box X- and Y-pixels large that gives a local mean within it). The standard deviation of each pixel from its local surroundings is calculated, and any that deviate by more than a given number of standard deviations are rejected. This procedure then undergoes several iterations, where the bad pixels are removed before each next iteration. A mean value is estimated in each frame to be used as a weight for a particular combination method in creating the final master flat. then divides the target images by the master flat.

Wavelength calibration

Independently of the type of object being observed, it is imperative that the data are accurately wavelength calibrated - that is, it is necessary to re-bin the data onto a linear wavelength scale. For the majority of instruments, this is a fairly straight-forward process. Wavelength calibration involves determining the relationship between pixel number and wavelength across the extent of the CCD. An 'arc lamp' exposure is taken close in time to the target exposures, whose spectral lines are of known wavelength, and covering the wavelength range required for the filter used, to account for any drift as the night progresses due to e.g. instrument flexure. The lines in the arc lamp spectrum are identified by the observer, and the centroids automatically determined for many cross-sections by a program of choice - for the data presented in this thesis, the program 2 was used. By fitting a polynomial to the pixel position and wavelength of the line, the resulting coefficients are then used to re-bin the data onto a linear, calibrated wavelength scale. The choice of arc lamp is mainly dependent on

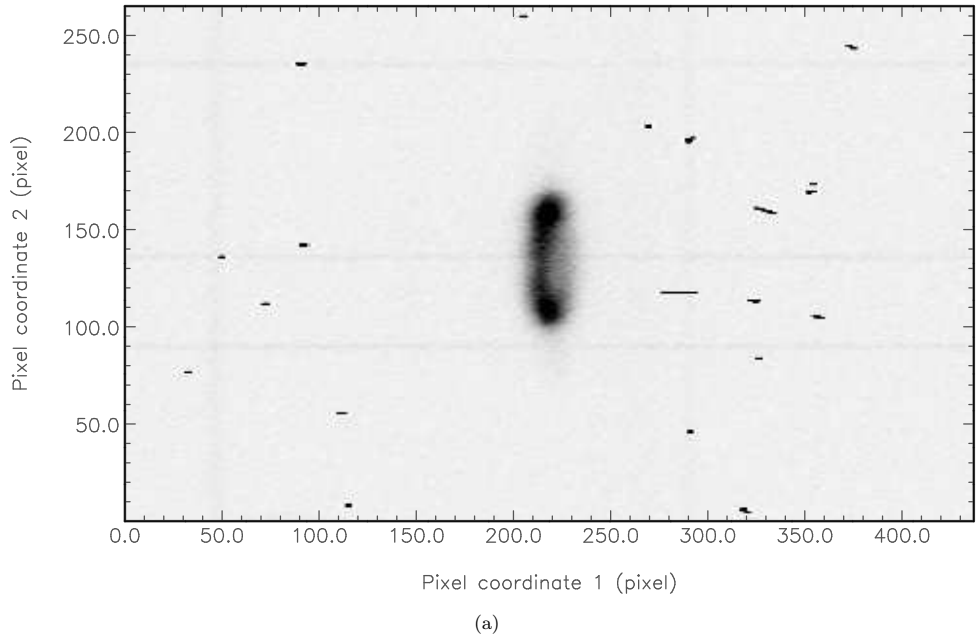

(a)

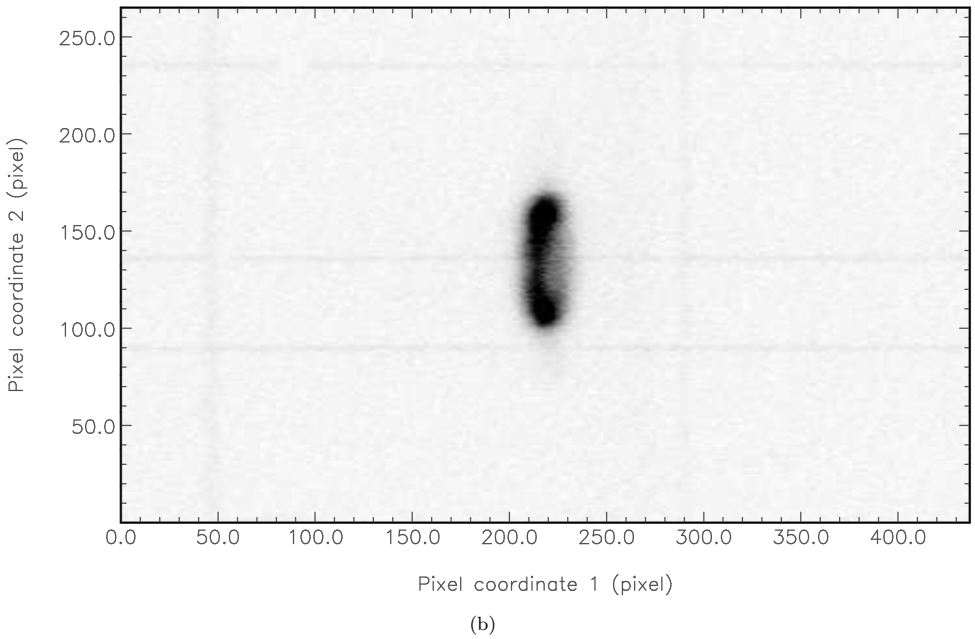

(b)

Figure 2.8: An example of an acquired data frame from NTT-EMMI (a) before the cleaning process to remove cosmic rays and bad pixels, and (b) after the cleaning process, using the routine within the package, .

the wavelength range to be calibrated, as the elemental gases within the lamp possess strong lines across different ranges. When the calibration needs to be applied over a wide spectral range, two lamps can be used in conjunction with each other to provide strong lines across the whole extent of the spectrum. Instrumental factors, such as the overall optical setup and the inefficiencies of the gratings, can also determine which arc lamp is best suited. When using AAT-UCLES, SPM-MES or VLT-UVES, Thorium-Argon (ThAr) is the usual choice for the standard filters used in PNe observations of Hα+[N] and [O]. NTT-EFOSC2 observations tend to be calibrated against an Helium-Argon (HeAr) lamp, as do those acquired from VLT-FORS2 (in conjunction with Neon (Ne) at higher resolution) or alternatively Mercury-Cadmium (HgCd) for grism 600B.

As mentioned previously, performing spectroscopy on PNe effectively means it is possible to create a 2D image of the object. In this way, spectral information, such as radial velocities and line widths can be determined alongside equally-important spatial information, such as the physical size and inclination of the PN. The program 2 , found within the package, was used to wavelength calibrate the nebular data presented in this thesis. An arc lamp exposure associated with a particular data frame in time is input into the program for the initial line identification, and a minimum of four lines are selected to give good spectral coverage (see Fig. 2.9). A wavelength is assigned to each line by the user, as given by a line atlas relevant for the particular instrument used. The lines are then accurately located by 2 at each cross-section by fitting a Gaussian to them; this is more accurate than simply finding centroids, as data from several cross-sections can be blocked together and a Gaussian applied to a block, to improve the S/N. Gaussians also provide errors on the fits, whereas centroiding does not.

Once the Gaussians have been applied to all blocks, a weighted polynomial function is then fitted to the lines to determine the dispersion relation. 2 finds all of the line centres first and checks the fits of the cross-sections before rejecting any bad lines. This happens before any of the polynomial fitting occurs, rather than the alter-

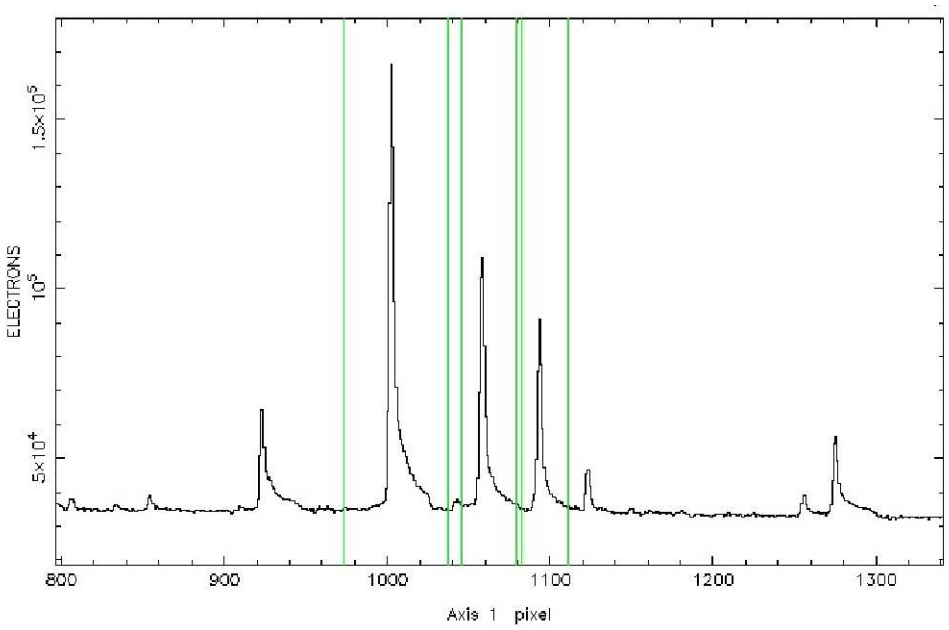

Figure 2.9: An example of line selection for a ThAr arc lamp used with NTT-EMMI created using 2 , found within the package .

native of locating the centres immediately prior to polynomial fitting as the program reads up the spectrum. The residuals of the fit are plotted against cross-section so it is possible to see if there is an effect from noise. The dispersion relation can then be visualised graphically (see Fig. 2.10). 2 tables the difference between the user-input wavelength and the fitted wavelength assigned to a particular line, and any spurious or bad points can be manually rejected from the fit. When the fit is satisfactory, the results (including the start and end wavelength to be applied to the target spectrum), are written to an output file that is then used to re-bin the spectral data from the target using the program, (see Fig. 2.11). An example of a data file before and after the scrunching process is presented in Fig. 2.12.

Transforming to a velocity scale

Since the inverse of the spectral resolution (see Eq. [2.1]) is equivalent to the equation for a non-relativistic Doppler shift (i.e. the formula is only valid in the case where the velocity is much less than the speed of light, $v \ll c$), the spectral axis can be converted

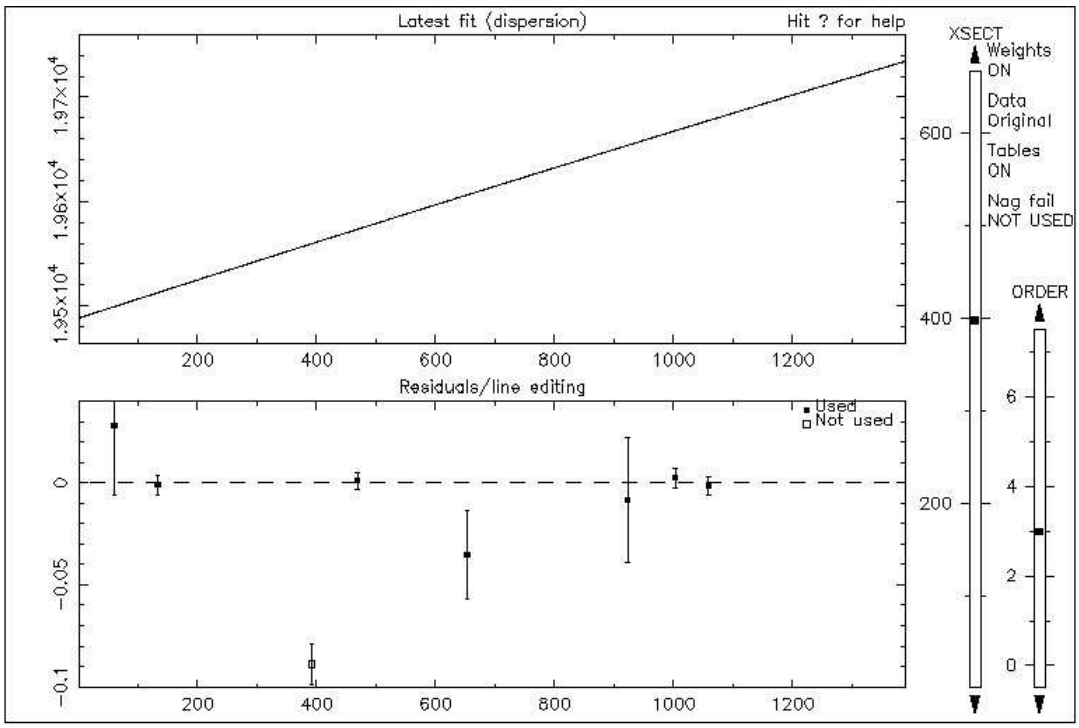

Figure 2.10: An example of the dispersion relation for a completed fit created using 2 , found within the package .

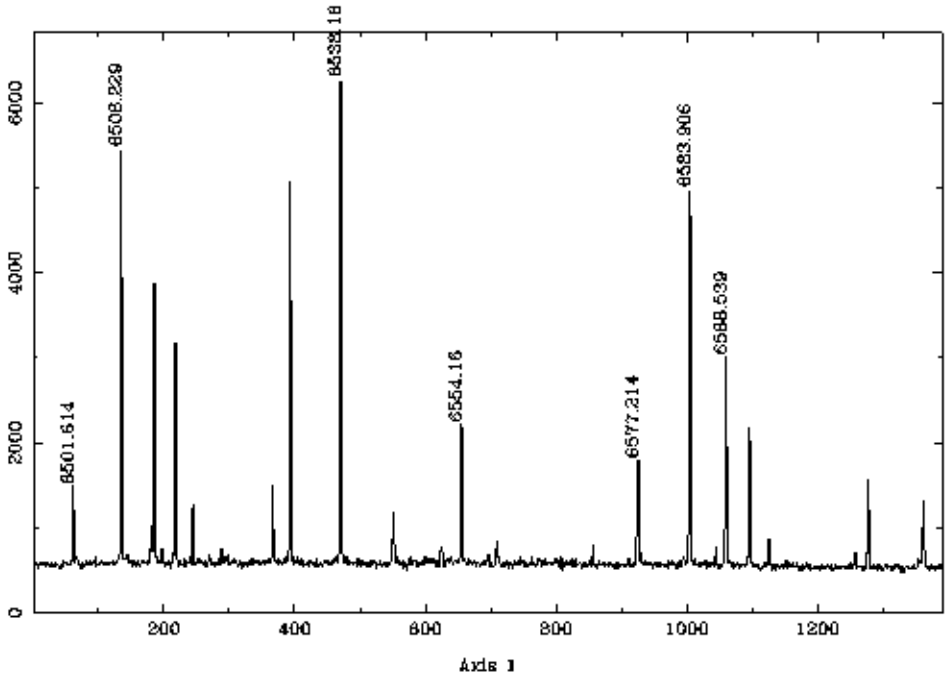

Figure 2.11: An example of an calibrated ThAr arc spectrum created using 2 , found within the package .

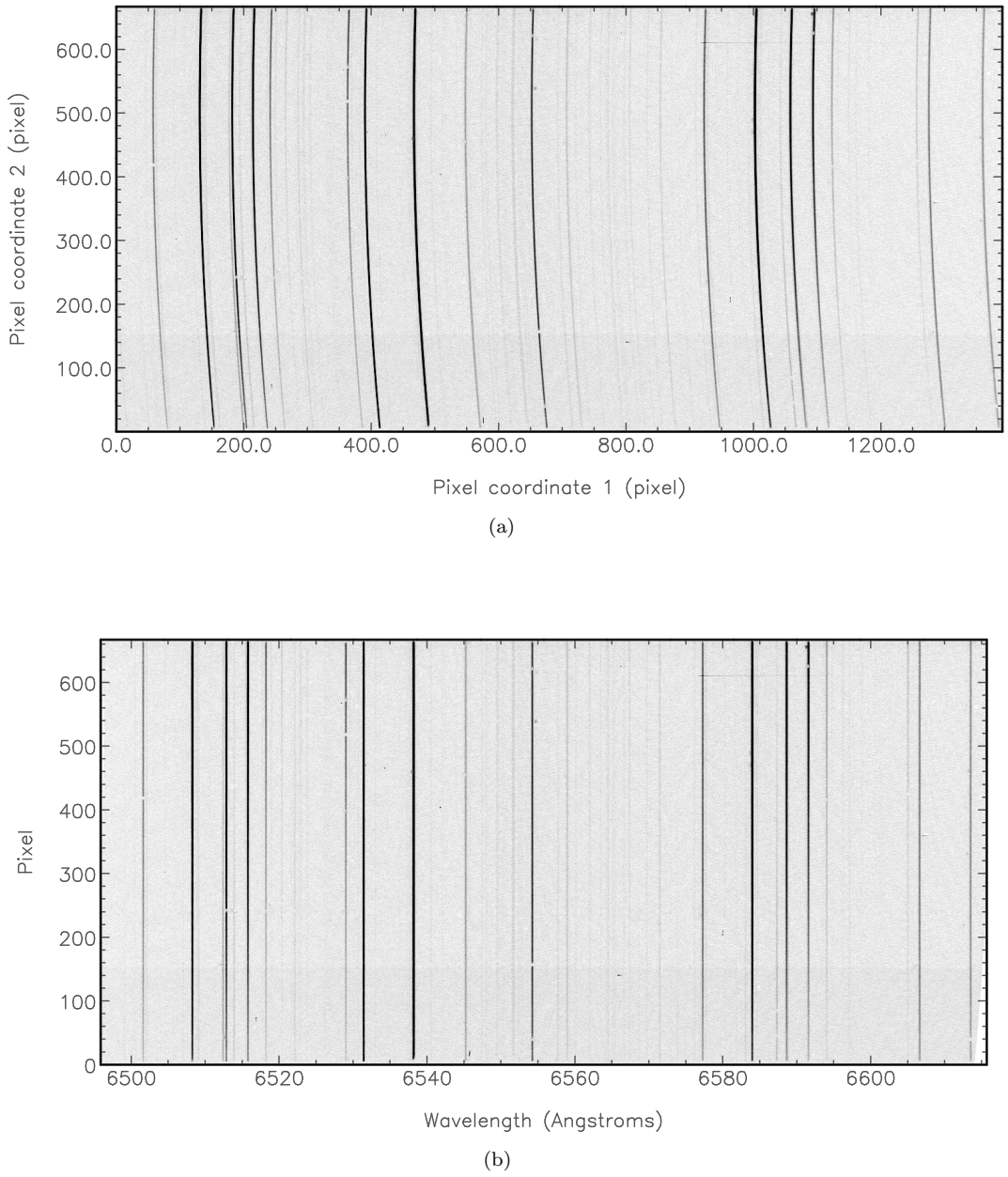

Figure 2.12: An example of ThAr arc lamp (a) before, and (b) after performing the 'scrunching' operation of the wavelength calibration process using the program, 2 , found in the package.

to a radial velocity scale once the data has been properly wavelength calibrated using the following:

$$\frac{\Delta\lambda}{\lambda_0} = \frac{v}{c} \tag{2.16}$$

where $\Delta\lambda$ is the difference between the observed and rest wavelength, λ_0 is the rest wavelength (for the most common nebular emission lines, these values are 6564Å for Hα, 6584Å for [NII], and 5007Å for [OIII]), v is velocity and c is the speed of light. This is applied to the data using the command , using the following format:

$$v = \frac{\lambda_c - \lambda_0}{\lambda_0} \times c \tag{2.17}$$

where λ_c represents the central wavelength of each pixel element; as such, the equation implies that for each given pixel centre, a new value is given corresponding to the current pixel centre minus λ_0 for a given filter. The resultant velocity is the spectroscopic radial velocity of the emission (i.e. the radial component of the velocity of the source along the line of sight - a linear quantity).

Since the observed emission is not found at λ_0, a correction must be applied to account for this by taking into account heliocentric velocity (the radial velocity of the centre of mass of the system with respect to the Sun, i.e. using the Sun as a standard of rest) at the time of observation. By inputting the name of observatory used in acquiring the observations, the target coordinates and the night the data were acquired into the program , radial velocity components of the system relative to the Sun are tabulated for every 30 minutes throughout the selected night. The radial velocity component corresponding to the time of observation of that particular data frame (to an accuracy greater than 0.01 km s^{-1}) is then subtracted from the nebular radial velocity using the command. Once the correction has been applied, the displayed velocity at the centre of the nebular emission is the complete heliocentric-corrected systemic velocity.

2.3.3 Reduction of stellar spectroscopic data

Since stellar spectra are acquired on a 2D detector, they must be collapsed down to 1D in order to extract the spectrum. This involves different data reduction and calibration techniques to those involved in the reduction of nebular data previously described. The following steps for further reducing the stellar data presented in this thesis were carried out using routines found within the data reduction package.

Flat fielding

To flat field the stellar data, the initial step to make a master flat frame is the same as outlined previously for the nebular data in Sec. 2.3.2. However, the master flat must be calibrated to be used with a 1D spectrum. Using the command , found in the package, the area of the frame containing the stellar spectrum is chosen and 'collapsed' by summing a number of rows across a pixel range in the y-direction to give a singular row from which the spectrum will be extracted. The output file is then divided by a constant - in this case, the number of pixels making up the range that produced the 1D array in the previous step, using the command. The resultant output spectrum undergoes a series of 1D smooths along cross-sections in the x-direction using the command, by convolving them with a Gaussian possessing specific values of sigma and cut-off width - outside of this width, the Gaussian is assumed to be zero. is then used to divide each pixel of every cross-section in the x-direction (i.e. each column with a constant y-value) in the master flat by a value from the corresponding pixels in the input smoothed spectrum. The output file at this point is the calibrated master flat frame that is then used to flat field the data frames, using the command to do so (see Fig. 2.13).

Wavelength calibrating stellar spectroscopy

The initial identification of arc lines using 2 is the same as the steps outlined previously in Sec. 2.3.2. However, instead of , the command (applicable

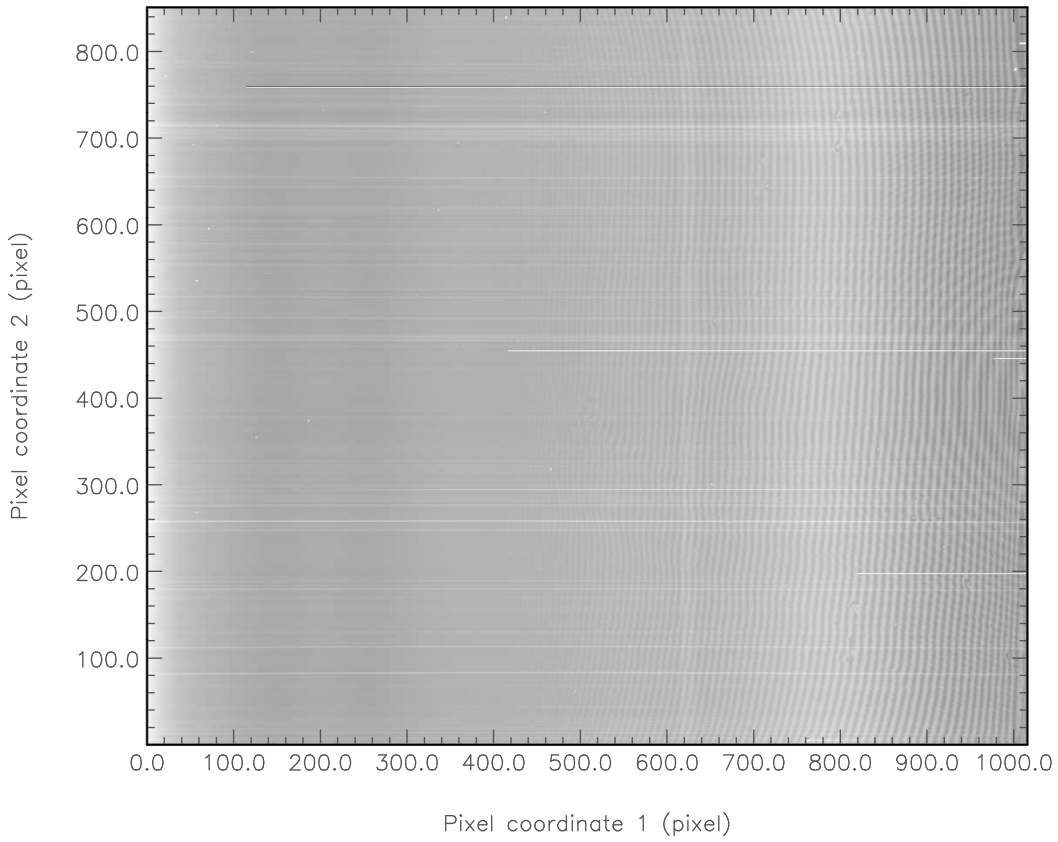

Figure 2.13: An example of a master flat frame for stellar data from NTT-EFOSC2, created using the package, . A dead pixel row is visible at pixel coordinate 760 on the y-axis.

to 1D spectra) is used to rebin the data to a linear wavelength scale. It is important to note that the accurate measurement of stellar spectral lines is not without its difficulties; for example, the spectral lines of early type stars are broad and diffuse as a result of their high $T_{\rm eff}$ and Stark broadening of the lines[i], as well as their associated rapid rotation. The spectral lines of late type stars are numerous, crowded together and prone to blending. With a double-lined binary, the lines from one star may be well separated from those of the other for much of the orbital period. However, at some point in time the two sets of lines approach each other and become partially blended and

[i]The 'Stark effect' is the shifting and splitting of atomic spectral lines due to presence of an external, static electric field. A typical stellar atmosphere cannot sustain a large electric field, as it is an electrical conductor due to its high $T_{\rm eff}$ and therefore high level of ionization. However, as two atoms approach each other in a near-collision, each induces a temporary dipole on the other. The effect of the resulting electric field of one atom on the other produces a general broadening of the lines as a result of the Stark effect (Tatum 2011).

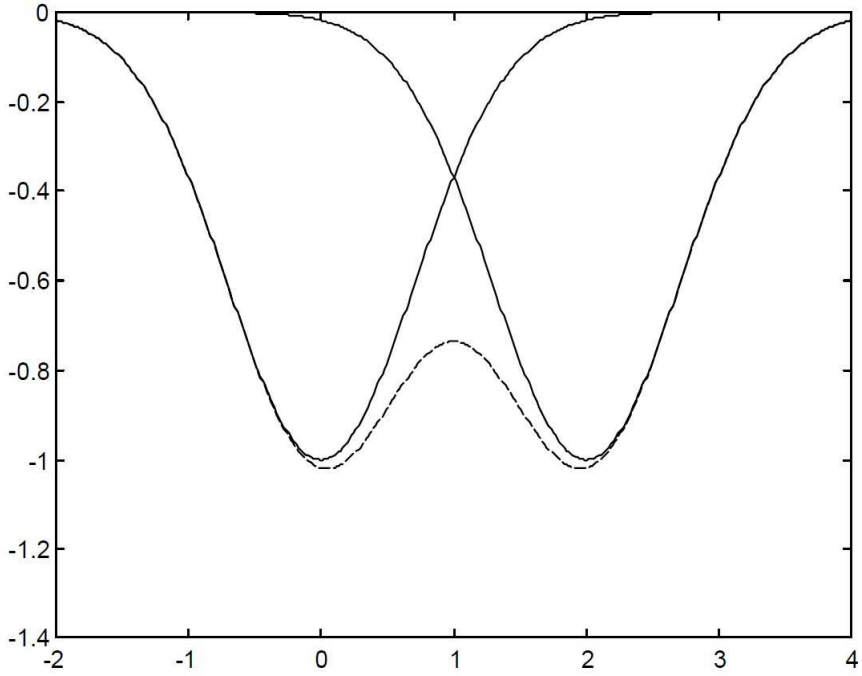

Figure 2.14: Example of a blended Gaussian line profile. The blending of the two solid lines is represented by the dashed line. Image taken from Tatum (2008)

as a result the minima of the blended Gaussian profile will occur closer together than the true minima of the individual lines (see Fig. 2.14). If the minima of the blended profile is inadvertently measured, then an incorrect value for the radial velocity of the system will be noted. As well as this blending effect, the spectra of the binary system may also be susceptible to a rotation effect - if the orbital inclination of the system is close to 90° then the system could be both a spectroscopic binary and an eclipsing binary. However, if the spectrum shows a single-lined binary and this star is determined to be a rapid rotator that is partially eclipsed by the secondary, it is only possible to view part of the surface of the primary that appears to be blue-shifted (due to rotation) towards the observer. This in turn would also give an incorrect measurement of the radial velocity of the system.

Extracting the stellar spectrum

The first step in extracting the 1D stellar spectrum from the 2D data frame is to perform sky subtraction. Using the command , regions above and below the spectrum of interest are selected and fitted with a polynomial in the spatial direction. Only the area within the selected limits is sky subtracted (see Fig. 2.15). The command is then used to determine the spatial profile of the 2D image ready for optimal extraction, by selecting the area on the image containing the spectrum of choice and dividing values along each column by the sum over the same column. Polynomials are used to smooth this profile by accounting for variations with wavelength within the profile. In doing so, the data are normalised (each column is summed to 1) to ensure that there are no negative points. is then used to perform the optimal extraction of the stellar spectrum using the algorithm of Horne (1986). The output spectrum is then the 1D, flat fielded spectrum that can subsequently be flux calibrated.

Flux calibrating stellar spectroscopy

Using spectroscopic standard stars, it is necessary to convert the pixel count into a relative flux (in this case, in units of ergs/s/cm^2/Å). The spectra of the standard stars are calibrated and extracted in the same way as previously described. The wavelength calibrated spectra of the standard stars are input into the package in a table format that provides both the wavelength scale and associated data values (in this case, the average flux density at a given wavelength), with the aim of providing the required range in the x-direction for the target data. The initial step is to turn these spectra into 'spiketra', a spectrum where all the non-tabulated elements are given a value of zero, with the command . When plotted, the output file shows the flux density at each of the tabulated points versus the given value of λ_c for each point in the form of a series of spikes. The next step is to calculate the instrumental response at each of the tabulated points with the command . By combining the spiketrum generated by with the observed spectrum of the standard star, a new spiketrum is generated

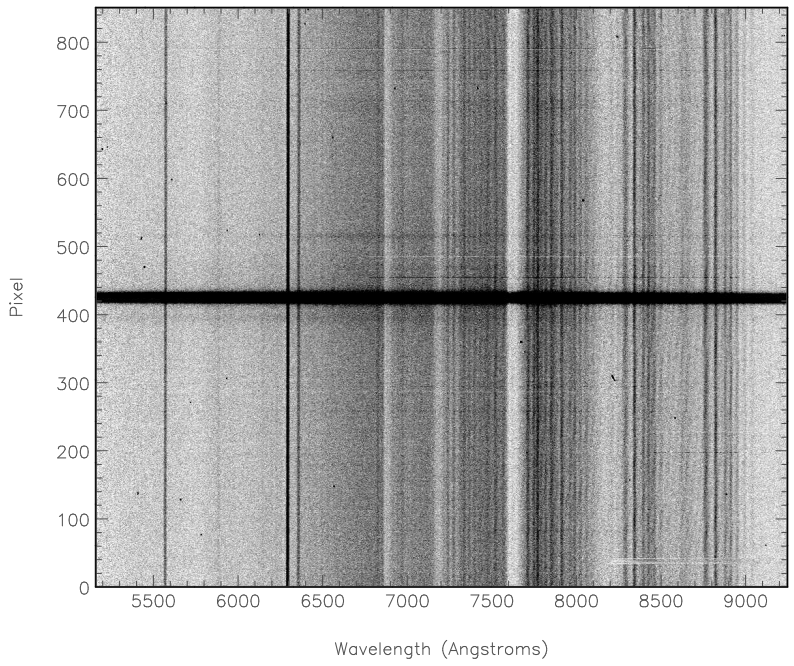

(a)

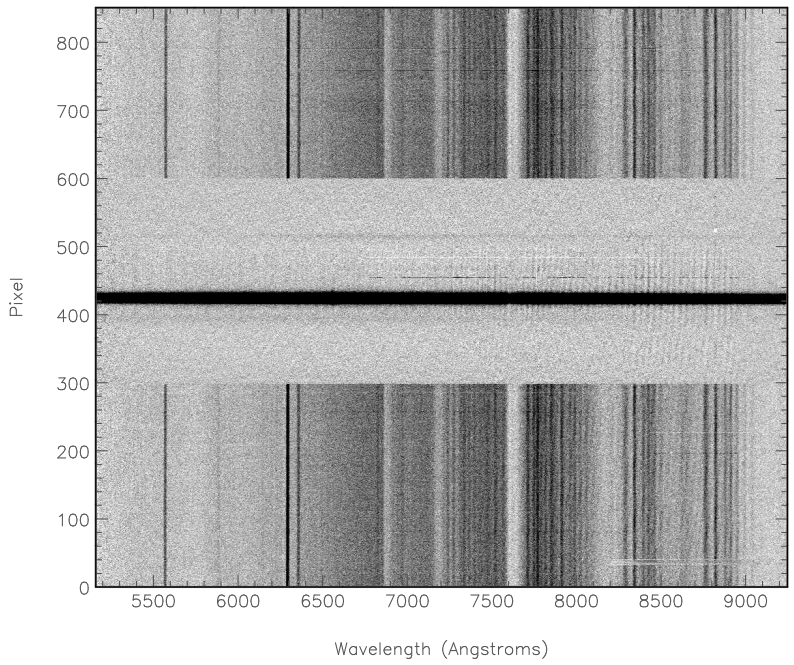

(b)

Figure 2.15: An example of a raw 2D stellar spectrum from NTT-EFOSC2 (a) before, and (b) after the command has been evoked.

that represents the instrumental response at each point of the standard star spectum (in 'units' per count per second per angstrom), by summing the counts in the observed spectrum over the given wavelength range, and dividing them by both the wavelength range and the exposure time. This result is then divided into the values for flux density given in the spiketrum generated by . By interpolating between the points of the new spiketrum with the command (by spline fitting), a new calibration spectrum is the final result. This newly calibrated spectrum of the standard star is then applied to the original, wavelength calibrated spectrum of the target star to give an overall flux-calibrated spectrum (see Fig. 2.16).

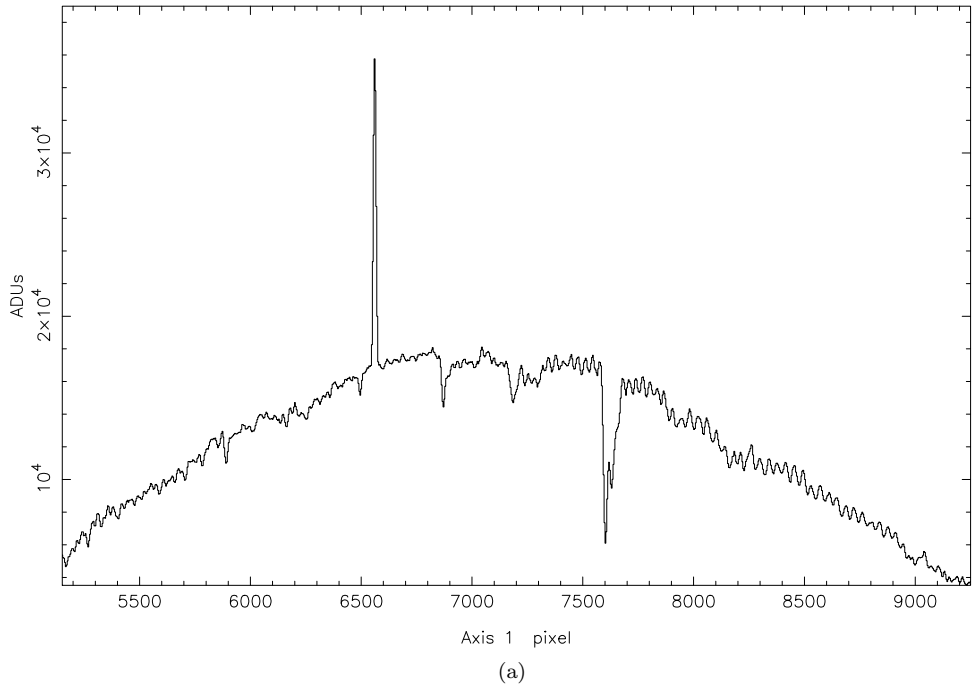

(a)

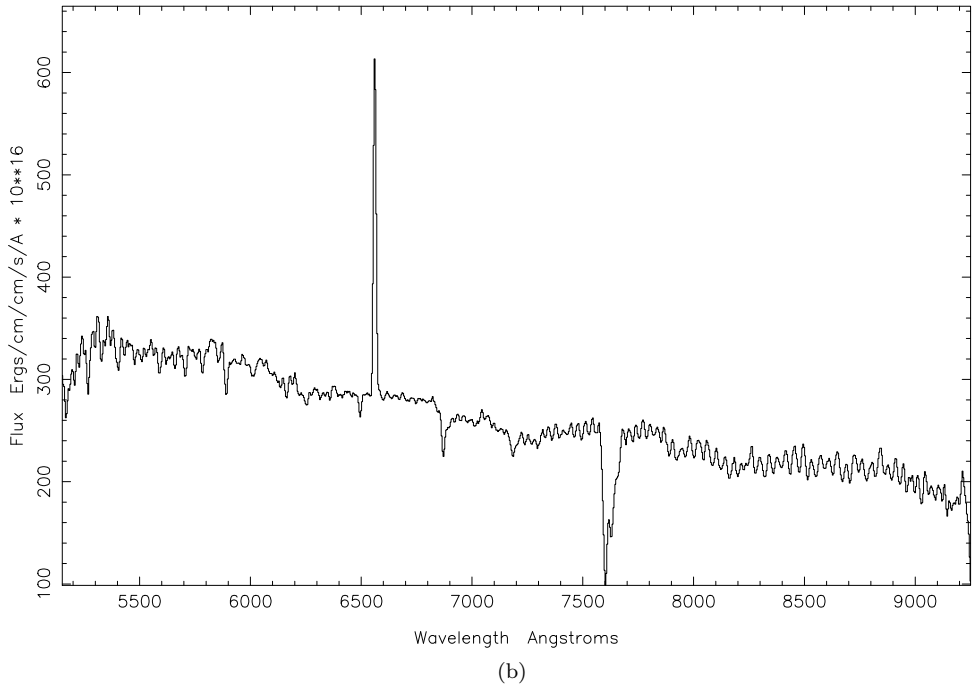

(b)

Figure 2.16: A 1D spectrum of LoTr 1 from NTT-EFOSC2, (a) before flux calibration, and (b) after flux calibration.

3

A study of the kinematics and binary-induced shaping of PN HaTr 4

The work presented in this chapter was published in Tyndall et al. (2012).[1]

3.1 Introduction

The planetary nebula HaTr 4 is one of few known to contain a post-Common Envelope (CE) central star system. CE evolution is believed to play an important role in the shaping of planetary nebulae, but its exact nature is yet to be understood. Using high spatial- and spectral-resolution spectroscopy of the [O] nebular emission line in combination with deep, narrow-band imagery, it is possible to develop a spatio-kinematical model in order to accurately determine the three-dimensional morphology and orientation of the nebula. Frictional forces between the binary and CE result in the transfer of angular momentum, causing the CE to be preferentially ejected in the stellar orbital plane – the symmetry axis of the PN is then expected to be perpendicular to the orbital plane of the binary. Therefore, observing this predicted alignment in a given PN is strongly

indicative that the nebular morphology has been influenced by the binary central star. Only six PNe have previously been observationally shown to possess the predicted alignment between nebula and binary plane – Abell 63 (Mitchell et al. 2007), Abell 41 (Jones et al. 2010b), NGC 6337 (Hillwig et al. 2010; García-Díaz et al. 2009), Sp 1 (Jones et al. 2012a), NGC 6778 (Miszalski et al. 2011a; Guerrero & Miranda 2012), and Abell 65, (Huckvale et al. 2013; Shimansky et al. 2009).

3.1.1 HaTr 4

PN HaTr 4, also referred to as PN G335.2-03.6 (α = 16^h 45^m 00.2^s, δ = -51° 12′ 22.0′′, J2000) is known to contain a photometric binary central star with a period of 1.71 d (Bond & Livio 1990). More detailed investigation by Bodman, Schaub & Hillwig (2012) revised the period to 1.74 d. In either case, no evidence is found for eclipses in the lightcurve, indicating that the inclination of the binary orbital plane with respect to the line of sight must be less than 85°, with the best fit to the data being from a model developed by Bodman, Schaub & Hillwig (2012) at 75°.

Based on the discovery image of Hartl & Tritton (1985), shown in Fig. 3.1, and the subsequent narrowband images of Bond & Livio (1990), shown in Fig. 3.2, HaTr 4 has the appearance of a classic ‘butterfly’ or ‘bow tie’ bipolar nebula lying in the plane of the sky with twin lobes emanating from the central star in an east-west direction. However, imagery alone is insufficient to precisely and unambiguously determine the nebular structure and orientation, as PNe are very prone to inclination-dependent projection effects (Kwok 2010; Frank et al. 1993). Only by using high-resolution, spatially resolved spectroscopy is it possible to fully ascertain the intrinsic 3D structure of a given nebula in order to assess whether the binary has played a role in the shaping of the nebula (see Ch. 2 for more details).

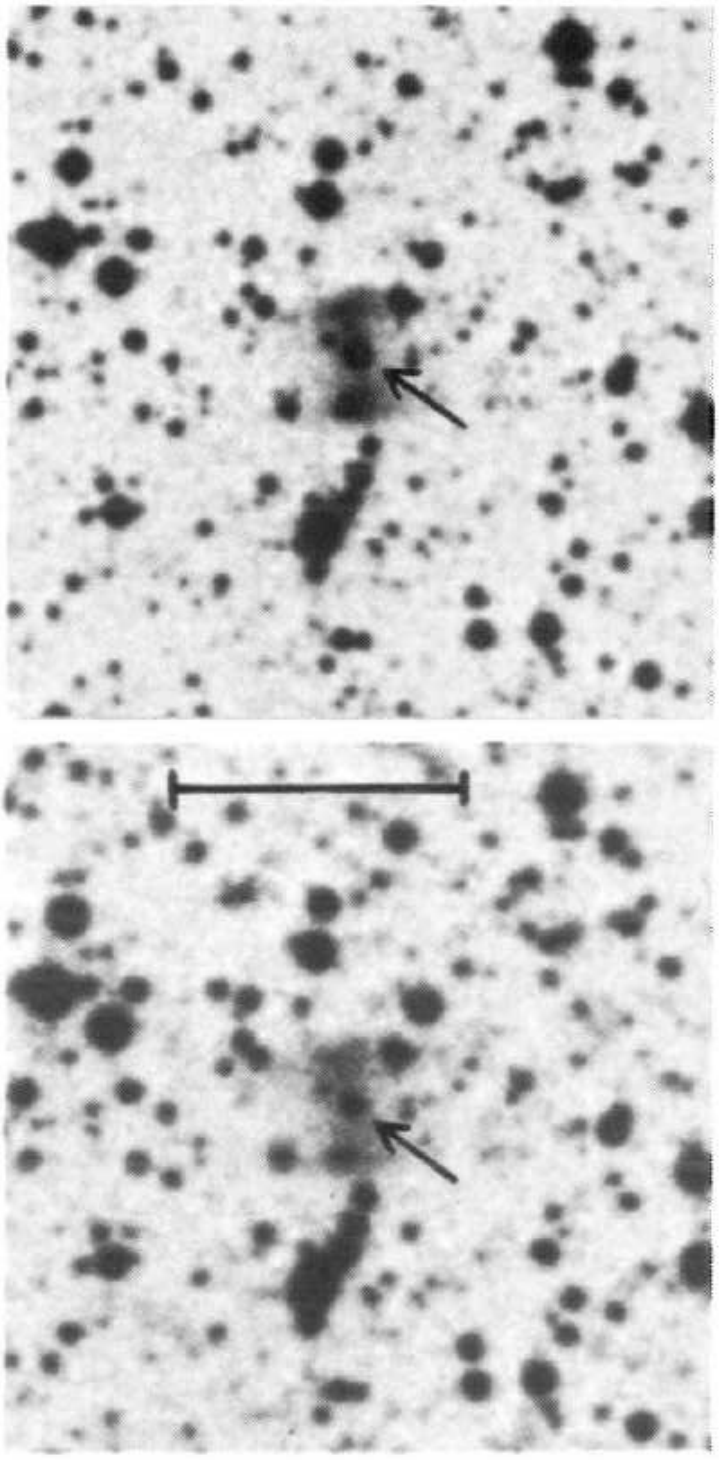

Figure 3.1: Original [O] images of HaTr 4 published by Hartl & Tritton (1985), displayed at different contrasts.

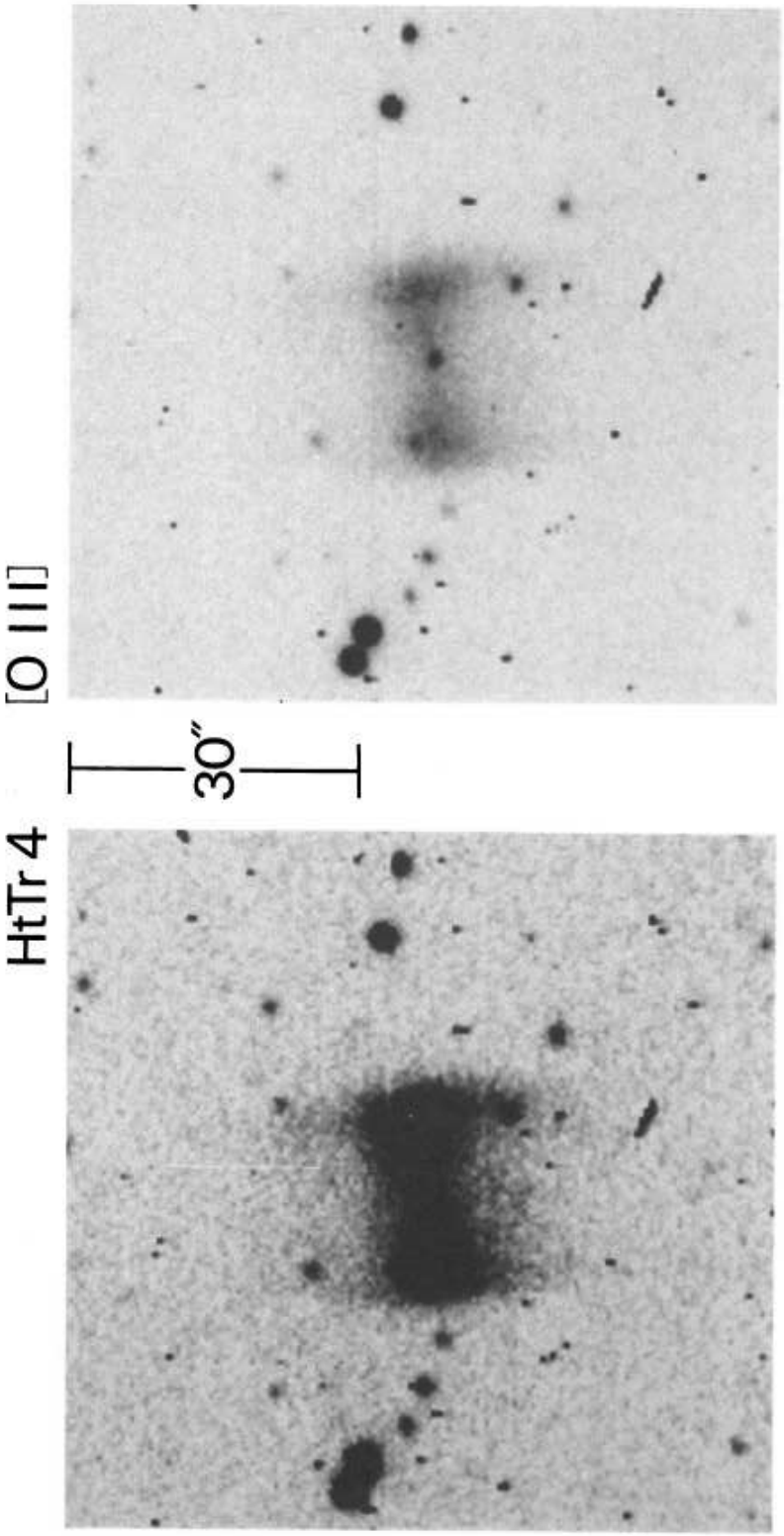

Figure 3.2: UKST-R and SERC-J images of HaTr 4 published by Bond & Livio (1990)

3.2 Observations

The deep Hα+[N] image shown in Fig. 3.3 was acquired on 1995 April 22, using the ESO Multi-Mode Instrument (EMMI; Dekker, Delabre & Dodorico 1986) on the New Technology Telescope (NTT) with an exposure time of 1800 s and seeing of 1.1 arcsec. The image clearly shows the 'bow tie'-shaped central nebula as seen in the original [O] imagery of Bond & Livio (1990) presented here in Fig. 3.2, but also faint extensions to the north and south. These extensions are more consistent with a symmetry axis orientated roughly north-south (as opposed to the previously inferred east-west axis), indicative that the observed emission may, in fact, form the waist of of a larger nebula.

On 2005 March 03-04, data were acquired in both Hα+[N] of HaTr 4 using the red arm of NTT-EMMI. NTT-EMMI was operated in its 300 arcsec longslit, REMD (REd Medium Dispersion) echelle spectroscopy mode using grating #10 and a slit width of 1 arcsec (R $\sim$ 54 000, $\equiv$ 5.5 km s^{-1}). Two MIT/LL CCD chips arranged in a mosaic were used, each possessing 4096 $\times$ 2048 15μm pixels, and the subsequent data frames were stitched together using the MIDAS software package. The data were 2 $\times$ 2 binned to give a pixel scale of 0.33 arcsec in the spatial direction, and a velocity scale of 3.4 km s^{-1} per pixel. An exposure time of $t_{\rm exp}$ = 1200 s was used. Three slit positions were acquired at a position angle (PA) of 97°, and one at a PA of 7°, giving good nebular coverage. The slit positions are shown in Fig. 3.4 (a).

On 2008 July 10–11, data were acquired of HaTr 4 using grating #3 on the visual-to-red arm of the Ultraviolet and Visual Echelle Spectrograph (UVES; Dekker et al. 2000) on the Keuyen Unit Telescope (UT2) of the Very Large Telescope (VLT). VLT-UVES was operated in its 30 arcsec longslit mode with a 0.6 arcsec slit width (R $\sim$ 70 000) using a narrowband filter to isolate the [O] emission line profile and prevent contamination from overlapping orders. 1200 s exposures were taken at 10 different slit positions, shown in Fig. 3.4 (b). Slits 1–5 were taken at a PA of 7°, and slits 6–10 were taken at a PA of 97° in order to give full nebular coverage in

both an east-west and north-south direction. The spatial scale of the observations was 0.17 arcsec per pixel, and the seeing was between 0.8 arcsec and 1.0 arcsec for all observations.

Reduction of the spectra was carried out using standard routines within the - software package, as described in Ch. 2.3. The spectra were wavelength calibrated against a ThAr emission-lamp. Due to the optical set-up of EMMI (the ThAr calibration lamp has poor flux in the bluest orders), it was necessary to perform the wavelength calibrations using a long exposure (3600 s) ThAr emission lamp at the start and end of the night to gain a good number of arc lines, before cross-correlating with shorter exposure (200 s) Ne lamps taken immediately after each observation, to account for any drift due to telescope and instrument flexure. Small shifts ($\sim$ 0.06Å) were accounted for with a linear correction.

The reduced nebular spectra of HaTr 4 from VLT-UVES are presented in Figs. 3.5 and 3.6. Similarly, the reduced NTT-EMMI spectra are presented in Fig. 3.7. In each PV array, cross-section 0 arcsec defines where the central star is found.

The PV arrays presented in Fig. 3.5 are consistent with a nebula extended in the north-south direction, as indicated by the Hα+[N] image shown in Fig. 3.3, with slits 1, 3 and 5 showing velocity ellipses. However, some data are missing as the slit is not quite long enough to cover the full north-south extent of the nebular emission (as indicated by the sudden cut-off at the top and bottom of the PV arrays, e.g. at cross-section 13.5 arcsec in Fig. 2e). The PV arrays from both slits 1 and 3 (Figs. 3.5a and c) appear to be closed at their northernmost extent (as supported by the northern extension of slit 3, shown in slit 2, Fig. 3.5b) but open in the south; however, the data from the southern extension to slit 3 - slit 4, Fig. 3.5(d) - clearly shows that this PV array is in fact closed.

The presence of two separate velocity components (corresponding to the red- and blue-shifted sides of a velocity ellipse) is consistent with front and back walls of an expanding hollow shell extended along the slit length (i.e. in a north-south direction) - this orientation is perpendicular to the east-west orientation previously indicated by

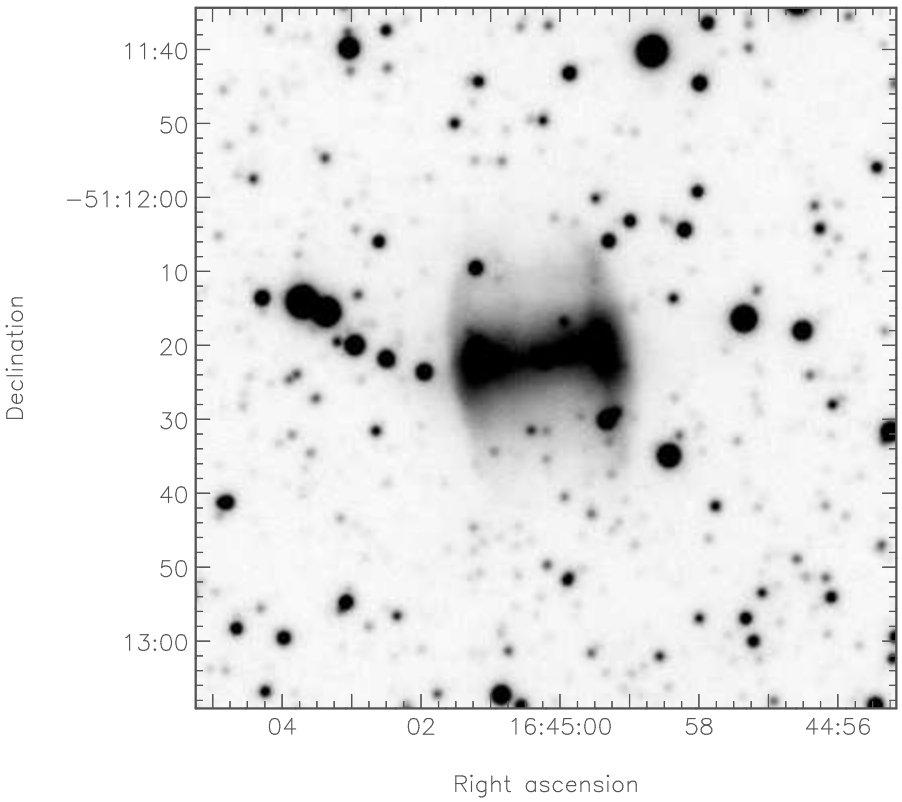

Figure 3.3: High contrast Hα+[N] NTT-EMMI image of HaTr 4.

the imagery presented in Fig. 3.3. The emission from the central (equatorial) region of this shell is significantly brighter than that from the north and south ends, and it is this equatorial region which gives the impression of an east-west bow tie shape, as seen in Fig. 3.3.

The PV arrays presented in Fig. 3.6 are obtained from slit positions perpendicular to those in Fig. 3.5. They each show a closed velocity ellipse, confirming the presence of a shell extending in a north-south direction. Slit 7 appears to have a larger FWHM for the blue-shifted component at cross-section 0 arcsec, whereas slit 9 appears to have a larger FWHM for the red-shifted component at cross-section 0 arcsec.

The PV arrays presented in Fig. 3.7 show HaTr 4 to have strong Hα emission, but only accompanied by significant [N] emission through the central E-W slit (slit position 2, Fig. 3.7d). The emission from a field star is visible at around cross-section 7 arcsec in this PV array. The 'hollow shell'-like structure that is apparent in Figs. 3.5

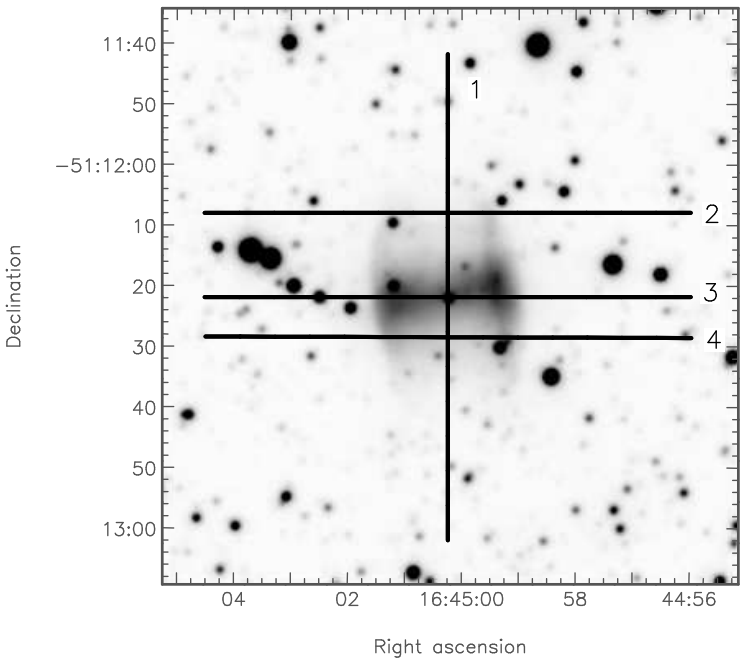

(a)

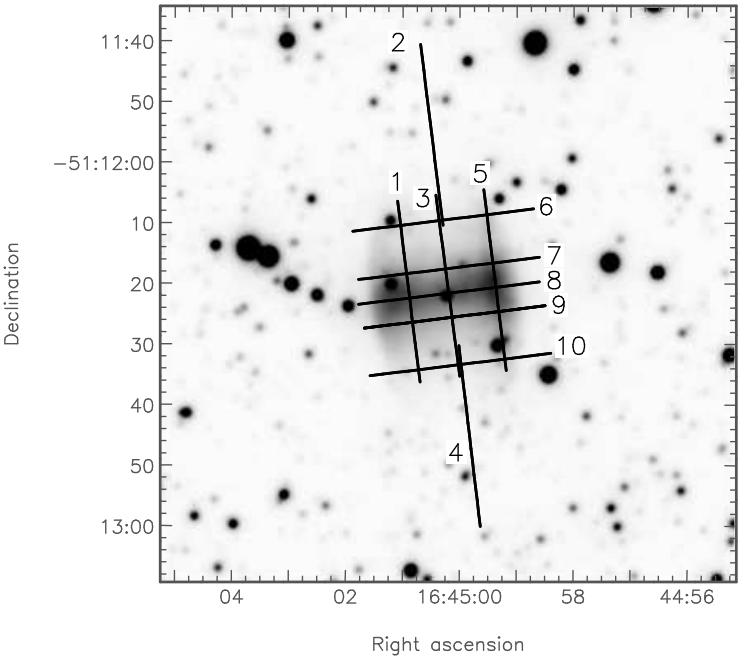

(b)

Figure 3.4: Figure showing (a) NTT-EMMI, and (b) VLT-UVES slit positions.

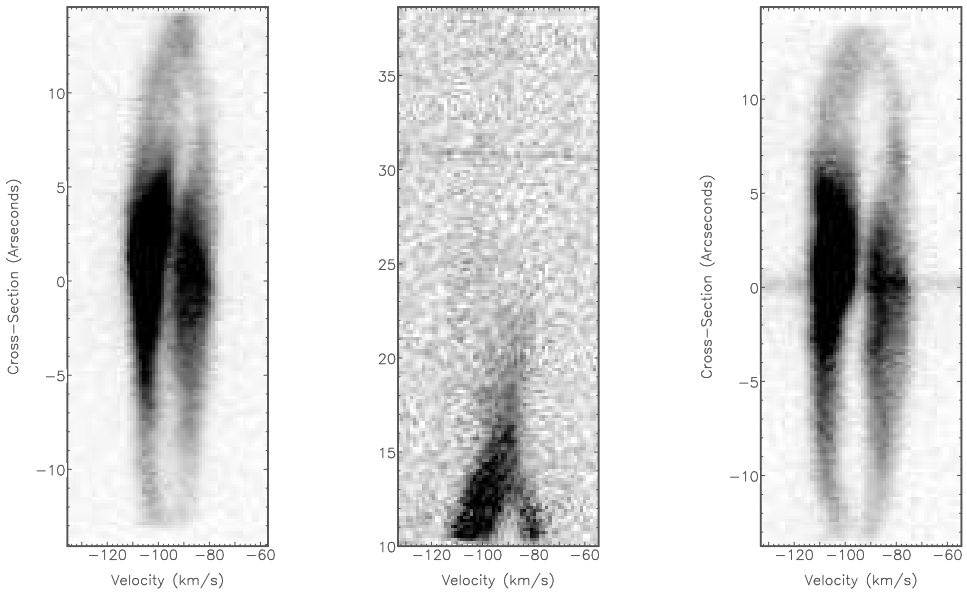

(a) Slit position 1 (b) Slit position 2 (c) Slit position 3

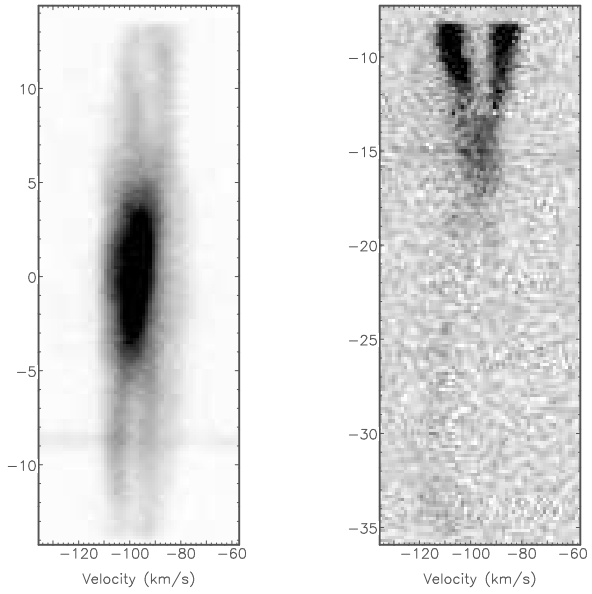

(d) Slit position 4 (e) Slit position 5

Figure 3.5: PV arrays showing reduced [O] spectra from the VLT-UVES slit positions 1–5. North is to the top of the array. The velocity axis is heliocentric velocity, $V_{\rm hel}$. The display scale has been modified to highlight the spatio-kinematic features referred to in the text. Cross-section 0 arcsec defines where the central star is found, the continuum of which can be seen in (c). The continuum of a field star is visible in (d) at cross-section -8 arcsec.

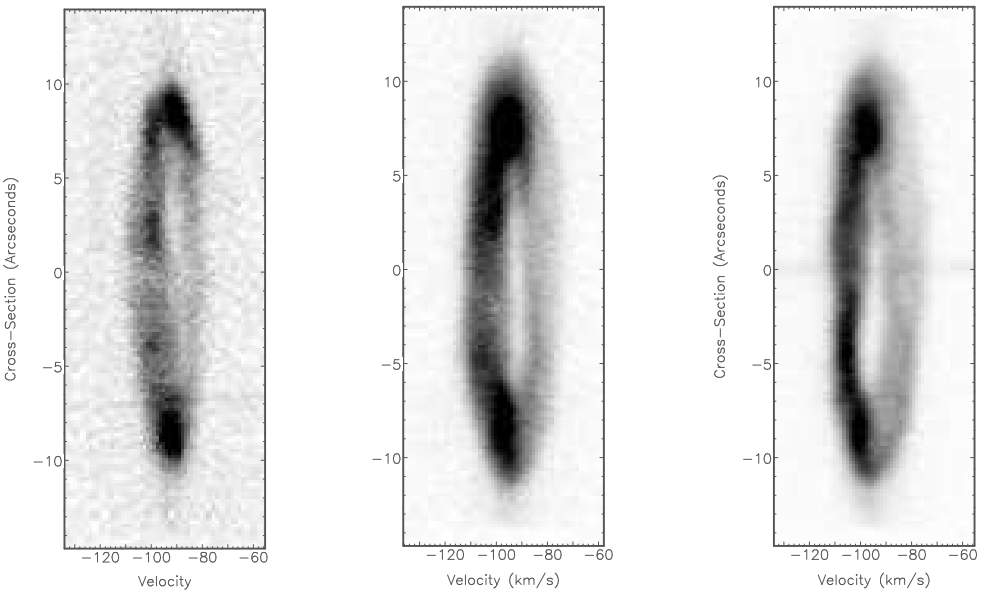

(a) Slit position 6 (b) Slit position 7 (c) Slit position 8

(d) Slit position 9 (e) Slit position 10

Figure 3.6: PV arrays showing reduced [O] spectra from the VLT-UVES slit positions 6–10. West is to the top of the array. The velocity axis is heliocentric velocity, $V_{\rm hel}$. The display scale has been modified to highlight the spatio-kinematic features referred to in the text. Cross-section 0 arcsec defines where the central star is found.

and 3.6 is not so clear in the EMMI data due to the solid appearance of the Hα emission. There is a suggestion of it in the [N] emission shown in Fig. 3.7 (d), as one can see the obvious brightening to the red-shifted side, but also a fainter, connecting component between 90-100 km s^{-1} to create a velocity ellipse. The Hα emission shown in Fig. 3.7 (a) could also be said to show signs of a velocity ellipse in the fainter, more extended components at around cross-sections +5 arcsec and -5 arcsec. No discernible structure is shown in the [N] emission in Fig. 3.7 (b). No [N] emission was visible for slit positions 3 and 4, and so only the Hα is presented in PV arrays for these two slits. Again the Hα emission presented in Fig. 3.7 (f) shows an indication of the shell-like nature of HaTr 4, with a fainter component visible in the centre also between cross-sections +5 arcsec and -5 arcsec that is obscured by the bright component on the red-shifted side (the spectrum of another star is visible at around cross-section 7 arcsec). However, it is only with the VLT-UVES spectra presented above that the true structure of HaTr 4 can be inferred.

3.3 Spatio-Kinematical Reconstruction

Using the astrophysical, user-driven modelling program [i] (Steffen & López 2006; Steffen et al. 2011), a spatio-kinematical model was developed in order to reconstruct the nebular morphology of HaTr 4 based on both the high resolution Hα+[N] imagery shown in Fig. 3.3 and the high resolution, spatially resolved [O] spectra shown in Figs. 3.5 and 3.6.

The main aim of the program is to allow users to reconstruct the 3D structure of an astrophysical object based on the observations acquired (as such, the term 'reconstruction' is more appropriate than 'model'), specifically with data sets in mind that may lack sufficient detail, or for cases where the observed object does not conform to usual standards that allow for easy and obvious modelling. In its most basic form, the initial model is constructed in a 3D environment with a mesh-based renderer by

[i] http://bufadora.astrosen.unam.mx/shape/

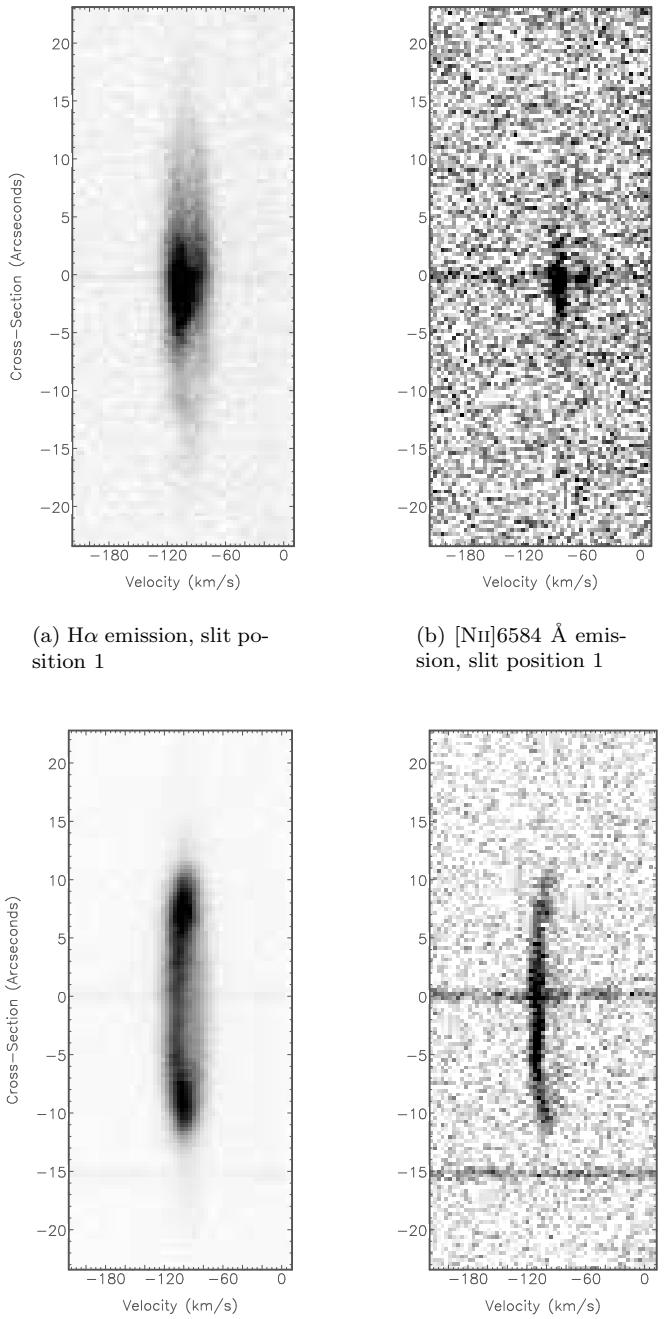

(a) Hα emission, slit position 1

(b) [NII]6584 Å emission, slit position 1

(c) Hα emission, slit position 3

(d) [NII]6584 Å emission, slit position 3

Figure 3.7: Hα+[N] spectra from the NTT-EMMI slit positions that pass through the central star, 1 and 3. In (a) and (b), north is to the top of the array. In (c) and (d), west is to the top of the array. The velocity axis is heliocentric velocity, $V_{\rm hel}$. The display scale has been modified to highlight the spatio-kinematic features referred to in the text. Cross-section 0 arcsec defines where the central star is found.

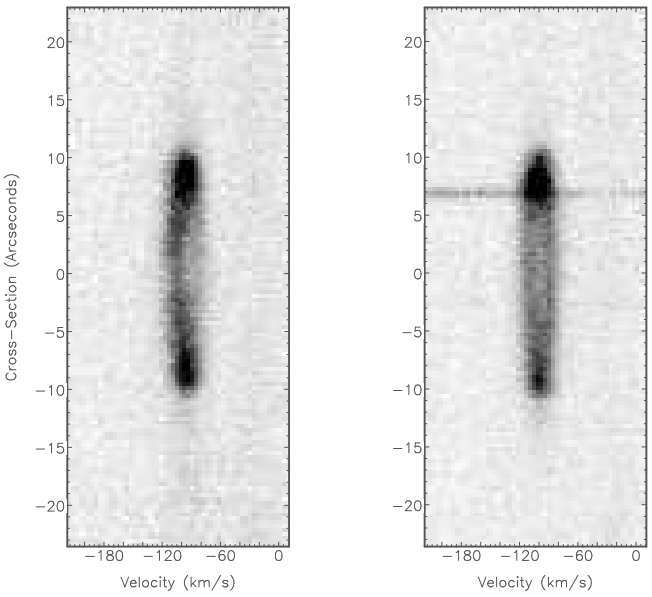

(a) Hα emission, slit position 2

(b) Hα emission, slit poisition 4

Figure 3.7: Hα spectra of HaTr 4 from the NTT-EMMI slit positions 3 and 4. West is to the top of the array. The velocity axis is heliocentric velocity, $V_{\rm hel}$. The display scale has been modified to highlight the spatio-kinematic features referred to in the text. Cross-section 0 arcsec defines where the central star is found. The spectrum of a field star is visible in (f) at cross-section 7 arcsec.

the user from a basic geometric object that is subsequently intricately adjusted with so-called 'modifiers' (that allow user control over general parameters such as size, rotation, etc., and also operations along a specific axis such as 'sheer', 'squeeze' and 'twist') until it represents the observed object. then allows the user to view the the result in a 2D simulation representing how the 3D model object would appear in 'reality', by producing both an image and a spectrum as though it had been observed through a telescope and spectrograph. These output images can then be directly compared to the observations to gain a best fit, with a margin of error based on how much the parameters can be changed before the two no longer conform.

A wide range of different morphologies and orientations for the nebular shell and waist were applied to the model of HaTr 4. The nebular expansion was assumed to follow a Hubble-type law (i.e. $v \propto r$), but the scale velocity was considered a free parameter in the modelling ($[r/r_o] \times k$, where r is radius from the central star, r_o is the

inner equatorial radius, and *k* is the velocity at r_o).

A more cylindrical structure for the base geometry was discounted, as a cylindrical shell produced a nebula which was too 'straight-edged' compared to the observed imagery, and did not create the roughly elliptical profile followed by the two spectral components observed in slits 1–10 (see Fig. 3.8). Similarly, a tighter waist was also discounted as it gave both the nebular image and spectra a 'figure-of-eight'-like appearance, with the nebular shell protruding from the central bow tie rather than it being a smooth transition, i.e. it is not 'wasp-waisted', akin to other such close binary central star planetary nebulae (bCSPNe) whose waist radius is comparable to that of its bipolar lobes, such as Abell 41 (Jones et al. 2010b). If the shell thickness parameter was set to greater than 5 arcsec, it created broader components at the northern and southern tips of the model spectra than are observed in the data. A ring was applied to the equatorial region of the model in order to increase the apparent thickness of the shell at low latitudes. The bow tie shape could not be accurately reproduced by simply enhancing the brightness of the shell in this region. Moreover, the increased physical thickness also leads to broader FWHM spectral components from this equatorial region due to the larger range of velocities present.

The best-fitting basic model, determined by eye, was an elongated ovoid nebular shell incorporating a thicker equatorial ring, an image of which is shown in Fig. 3.9 at the same scale, PA (7°), and inclination to the line of sight as the image shown in Fig. 3.3 and presented again here for comparison. The synthetic PV arrays corresponding to this best-fitting model are presented in Fig. 3.10. The model accurately reproduces the two velocity components seen in all of the slit positions shown in Figs. 3.5 and 3.6, corresponding to the front (blue-shifted) and back (red-shifted) walls of the main nebular shell. The model also recreates the bright emission associated with the nebular waist, appearing as the two bright velocity components around cross-section 0 arcsec (see Fig. 3.10e).

Once the basic model was determined, its inclination was varied in order to assess over what range a satisfactory fit to the data could be found. Comparison between

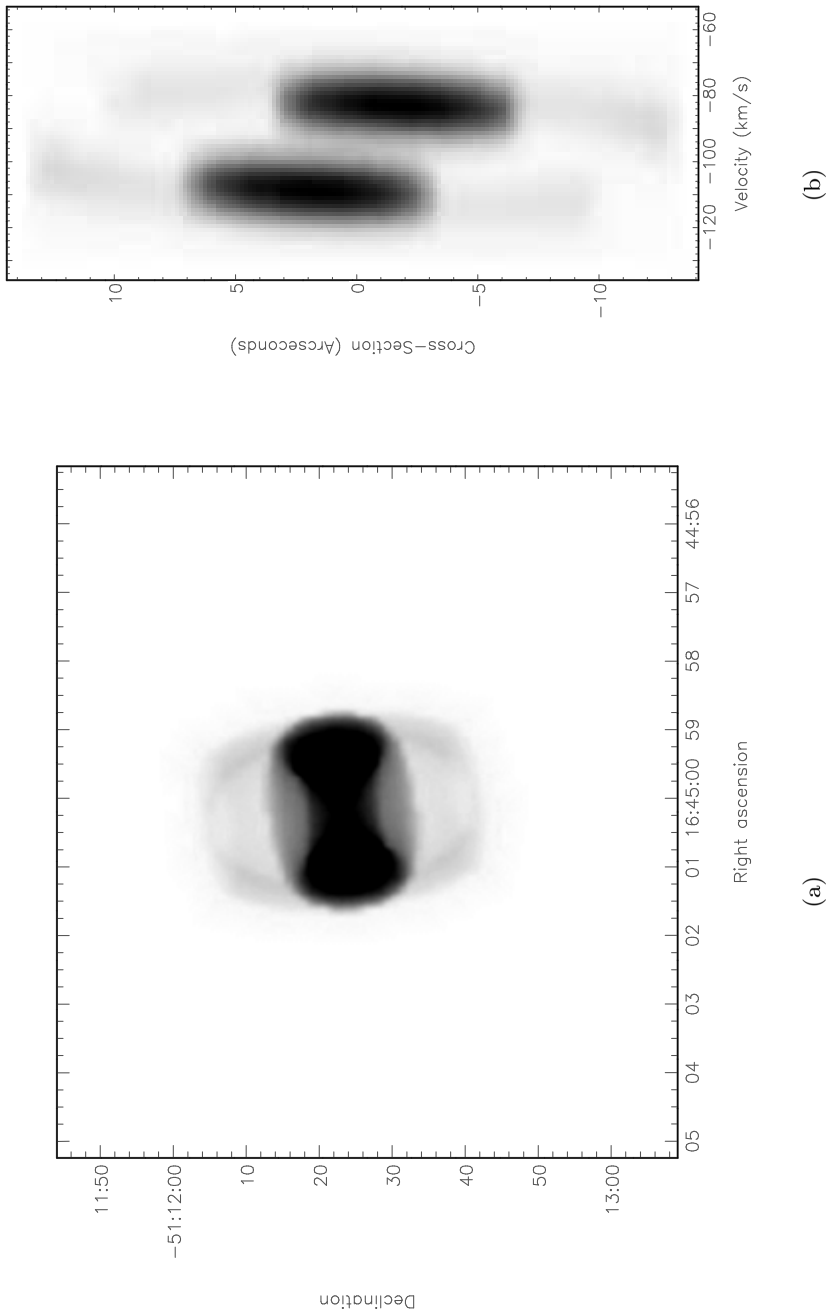

Figure 3.8: (a) model of HaTr 4 at the best-fitting inclination of 75°, and (b) the resultant model spectra, based on an initial cylindrical geometry.

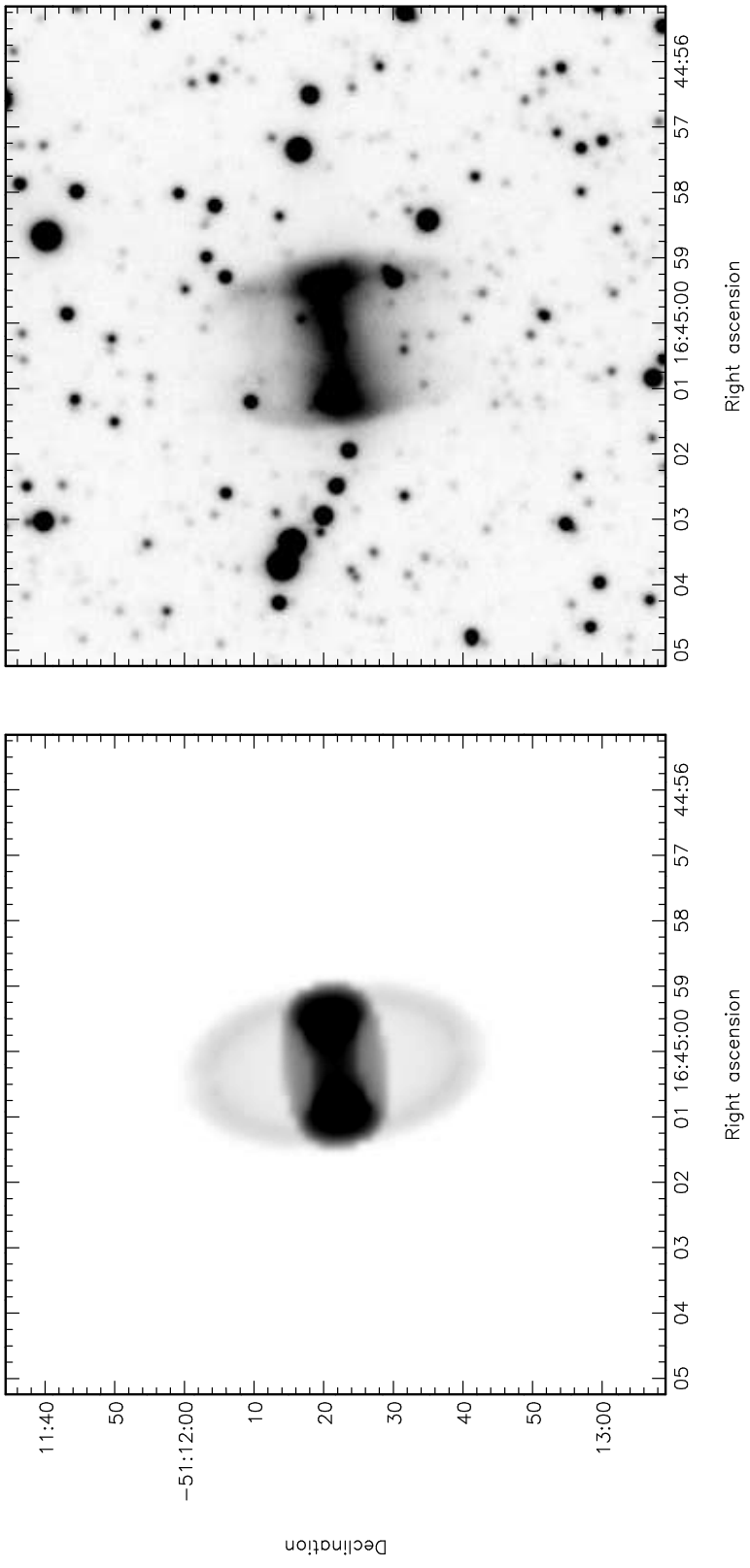

(a) 75° model nebula

(b) Observed image of HaTr 4

Figure 3.9: (a) model of HaTr 4 at the best-fitting inclination of 75°, with (b) the real observed image for comparison.

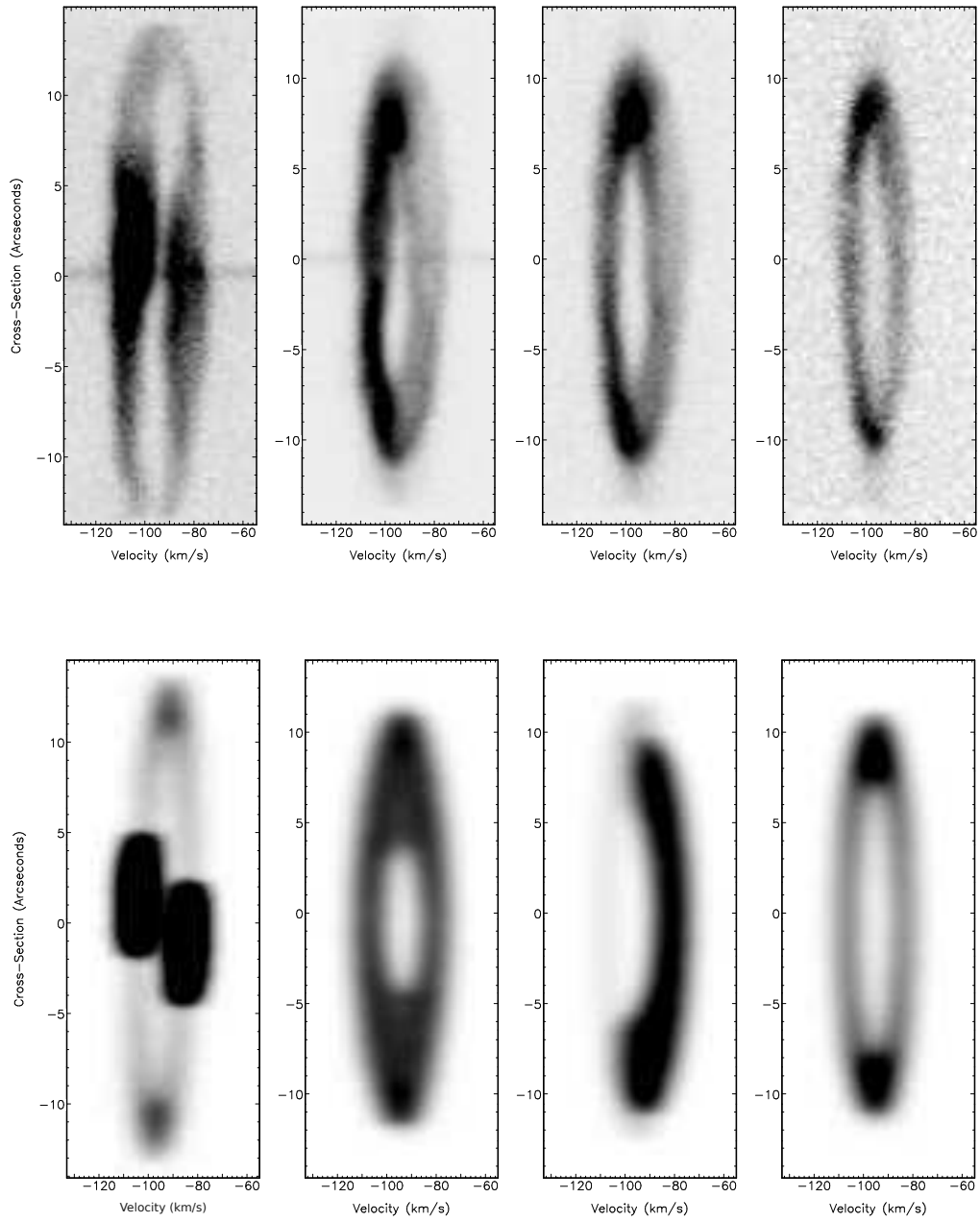

Figure 3.10: Top row (a)–(d) reproduces the observed spectra for slit positions 3, 8, 9 and 10 (see Figs. 3.5 and 3.6). Bottom row (e)–(h) shows the equivalent models, at a best fitting inclination of 75° relative to the line of sight, to show the differences between cuts through the major axis, equatorial ring, and the outer shell of the nebula. Slit positions are as shown in Fig. 3.4.

observed and modelled imagery constrains the inclination of the nebula to be between 65° and 80° – below 65° the central bow tie becomes too extended in the north-south direction, and its centre becomes too narrow as less of the ring overlaps in the line of sight. Above 80°, the ring becomes too tube-like in shape rather than the apparent bow tie as the model nebula becomes close to lying in the plane of the sky. Comparison between modelled and observed spectroscopy further constrains the inclination to be 75° ± 5°, as other inclinations did not replicate the observed brightness offset between the red- and blue-shifted velocity components seen in slits 1–5.

The key parameters of the best-fit model are summarised in Tab. 3.1. The determined expansion velocity relative to the central star of V_{exp} = 13 ± 2 km s^{-1} in the equatorial plane is fairly typical for a PN (Weinberger 1989), and the systemic velocity (V_{sys} = -94 ± 4 km s^{-1}) is in good agreement with that of Beaulieu, Dopita & Freeman (1999; V_{sys} = -97 ± 15 km s^{-1}). The kinematical age per unit distance, as determined by the model parameters, is found to be 4516 ± 766 yrs kpc^{-1}. Using a surface brightness-distance relationship, Frew (2008) finds a distance to HaTr 4 of roughly 3 kpc; using this value, we derive a kinematical age of 13 550 ± 2300 yrs for HaTr 4 and an equatorial radius of approximately 0.18 pc.

Fig. 3.10 (e) shows the model spectrum corresponding to the observed PV array from central slit 3 (reproduced above it in Fig. 3.10a) at the best-fitting inclination of 75°. The model PV array nicely confirms that the splitting of bright components shown in the spectrum is indeed due to an elongated shell possessing a thicker and brighter equatorial ring, as the relative vertical offset between the two bright components is dependent on nebular inclination. Figs. 3.10 (f), (g) and (h) shows the models of slits 8, 9 and 10 (see Fig. 3.4) at the best-fitting inclination of 75° beneath their observed spectral counterparts to highlight how the brightness variations across the velocity ellipses change depending on the shell/waist overlap as a result of inclination effects. The fact that the variations in the model do not exactly match the spectra highlights the asymmetry of the structure of HaTr 4 in reality. Indeed, in all of the spectra shown in Figs. 3.5 and 3.6, the blue-shifted emission component is observed to be

Table 3.1: Table of the main parameters of nebular ring in the best-fitting model of HaTr 4 shown in Fig. 3.9 (errors are the range over which the parameter could be altered and still be considered a reasonable fit to the observed image and spectra).

Parameter	**Value**
Semi-major axis (to outer edge)	12.65 ± 0.5 arcsec
Semi-minor axis (to outer edge)	7.5 ± 0.5 arcsec
Shell thickness	5 ± 1 arcsec
Equatorial expansion velocity, V_{exp} (r = 7.5 arcsec)	13 ± 2 km s^{-1}
Heliocentric systemic velocity, V_{sys}	-94 ± 4 km s^{-1}
Inclination, *i*	75 ± 5°

brighter than the red-shifted with no obvious explanation, as the best-fitting model does not replicate this trend; however, possible explanations are ISM interaction (which may also account for the thinner nature of that side in Fig. 3.6 (c)), or more likely that there is internal extinction blocking emission from the back wall.

The velocity difference between the front and back walls of the nebular shell was determined by subtracting the heliocentric velocity of a point on the red-shifted side of the model spectra from an equivalent point on the blue-shifted side, giving an expansion velocity of $V_{\rm exp}$ = 13 ± 2 km s^{-1}. The angular diameter of the nebula was determined to be 23 ± 2 arcsec, giving an equatorial radius of 0.16 pc. The kinematical age of HaTr 4 is therefore of order 12 044 ± 2450 yrs at 3 kpc. The expansion velocity and age of the nebula are fairly standard for a PN of this size.

The -modelled nebular inclination of 75° ± 5° relative to the line of sight is approximately perpendicular to the binary plane, as determined in the work of Bodman, Schaub & Hillwig (2012). Bodman, Schaub & Hillwig (2012) state that the best-fit range for the binary falls between 75° and 80°, but with an acceptable fit as low as 55°. In knowing that the PN symmetry axis is expected to lie perpendicular to

the orbital plane of the binary and having seen that the inclinations of the two *are* in agreement, these results further imply that the binary is responsible for influencing the shaping of HaTr 4.

3.4 Discussion

The imaging, spectroscopy and subsequent spatio-kinematical modelling presented in this chapter clearly show HaTr 4 to have an elongated, axisymmetric morphology with an equatorial enhancement consistent with a nebular ring. This work demonstrates for the first time that the symmetry axis of HaTr 4 lies in a roughly north-south orientation, as opposed to the east-west orientation inferred from previous imagery. The 'bow tie' appearance of the central region of the nebula is shown to result from a line-of-sight inclination effect associated with the enhanced nebular waist, rather than a bipolar structure as previously believed.

The spatio-kinematical modelling of HaTr 4 reveals fairly typical dynamical properties, with a kinematical age of order 13 500 yrs and an equatorial $V_{\rm exp} = 13 \pm 2$ km s^{-1}. This is consistent with the age derived from the observed spectra within the associated errors, which is of order 12 000 yrs at a distance of 3 kpc.

No evidence is found for extended emission beyond the main nebular shell or jet-like outflows associated with HaTr 4, such as those found in other known bCSPNe: ETHOS 1 (Miszalski et al. 2011a), The Necklace (Corradi et al. 2011), Abell 63 (A63) (Mitchell et al. 2007) and NGC 6337 (García-Díaz et al. 2009). Similarly, even once the effects of inclination have been taken into account, no obvious analogue for HaTr 4 can be found amongst the other bCSPNe which have been the subject of detailed spatio-kinematical study. While the morphology of HaTr 4 is axisymmetric it is not bi lobed, displaying more of an overall elliptical structure. Perhaps those that are morphologically the closest in resemblance to HaTr 4 are A63 (Mitchell et al. 2007) and Abell 41 (A41) (Jones et al. 2010b); however, both show marked differences to HaTr 4: A63 has no ring-like equatorial feature, and also displays extended polar out-

flows which are absent in HaTr 4. A41 does display an equatorial ring, but a far less extended version than the one seen in HaTr 4. Similarly, A41 has a distinct bi lobed structure not seen in HaTr 4. The other three PNe mentioned in Sec. 3.1 that are also shown to be aligned to the binary orbital plane are NGC 6337, NGC 6778, and Abell 65 (A65). Once again, they are very morphologically different to HaTr 4 which emphasises how many different mechanisms and intrinsic/extrinsic factors influence the process of the formation and shaping of PNe. NGC 6337 shows an almost completely circular (slightly elliptical) morphology, but is in fact the waist of a nearly edge-on bipolar nebula possessing point-symmetric structures, with an estimated binary–nebula inclination of order 15° (Corradi et al. 2000; García-Díaz et al. 2009; Hillwig et al. 2010). NGC 6778 is described as having a main nebular shell possessing a disrupted equatorial ring and kinematically disturbed bipolar lobes, implying that it most likely underwent an explosive event earlier on in its lifetime (Guerrero & Miranda 2012). The binary–nebula inclination for this PN is of order 85° (Miszalski et al. 2011a). Finally, A65 shows to be a double-shelled (non-coeval) PN with the inner nebula displaying the bipolar morphology, implying separate mass-loss events with a time differential of around 7000 yrs. In this case, the binary–(inner)nebula inclination is of order 68°. This lack of direct analogue highlights the morphologically disparate nature of the current sample of bCSPNe that have been studied in detail (Jones et al. 2011b). The imaging study of Miszalski et al. (2009b) did, however, indicate that the most common morphological feature amongst the known sample is some form of equatorial ring - a feature we have shown to clearly be present in HaTr 4, and is probably associated with the ejection of a CE.

The inclination of the nebular symmetry axis of HaTr 4 is found to be $\sim 75°$, consistent with the non-eclipsing nature of the binary central star. Further investigation into the central star system by Bodman, Schaub & Hillwig (2012), indicates that the inclination of the central binary plane is very close to the nebular inclination, as predicted by theories of binary-induced PN shaping (Nordhaus & Blackman 2006). HaTr 4 is one of only seven PNe to have had this alignment between nebular symmetry axis and

binary plane observationally shown, a finding entirely consistent with HaTr 4 having been shaped by its central binary star.

Notes

[1]The imagery presented in Fig. 3.3 was acquired by S.A. Bell and D. Pollacco under ESO programme ID 055.D-0550(A). The NTT-EMMI spectroscopy was acquired by D. Mitchell and D. Pollacco under ESO programme ID 074.D-0373(A). The VLT-UVES spectroscopy was acquired by T.J. O'Brien and D. Jones under ESO programme ID 081.D-0857(A). The subsequent data reduction, analysis and modelling was done by the author.

4

LoTr 1 and its relation to PNe possessing Barium central stars.

The work presented in this chapter was published in Tyndall et al. (2013).[1]

4.1 Introduction

LoTr 1 is a planetary nebula thought to contain an intermediate period binary central star system of orbital period, $P \sim 100$–1500 d; (van Winckel et al. 2009). The system shows the signature of a K-type, rapidly rotating giant and most likely constitutes an accretion-induced post-mass transfer system similar to other PNe such as LoTr 5, WeBo 1 and A70. Such systems represent rare opportunities to further the investigation into the formation of barium stars and intermediate period post-AGB systems – a formation process still far from being understood. In this chapter, I present the first detailed analyses of both the central star system and the surrounding nebula of LoTr 1 using a combination of spectra obtained with VLT-FORS2, AAT-UCLES and NTT-EMMI, as well as SuperWASP photometry.

4.1.1 LoTr 1

As discussed in detail in Ch. 1, the interaction between the progenitor star and a binary companion is believed to shape the resulting PN and in some cases even thought to be almost essential for a PN to form (Moe & De Marco 2006). The shaping influence of CE evolution has been studied extensively (see, e.g. Jones et al. 2010b; Tyndall et al. 2012) and understood in terms of either a collimated fast wind carving out an axisymmetric nebula (Soker & Rappaport 2000) or the ejected CE forming an equatorial density enhancement (Nordhaus & Blackman 2006) as required by the GISW model (Kahn & West 1985b; see Ch. 1.2.3). However, very little is known about intermediate period, post-AGB binaries, including their effect on PNe formation and morphology, due to lack of observations. The intermediate period binaries fall between post-CE systems (Miszalski et al. 2009a) and visually resolved systems (e.g. Ciardullo et al. 1999). Soker (1997) claimed that these interacting systems are the most likely PNe central stars to form the classical 'butterfly' (bipolar) morphologies, but with few systems known and limited investigations this has yet to be confirmed. Only by finding and studying CSPNe with intermediate periods can we substantiate this claim and relate the processes at work in the formation of PNe by both post-CE evolution and intermediate period CSPNe.

The PN LoTr 1 (α = 05^h 55^m 06.6^s, δ = −22° 54′ 02.4″, J2000) was first discovered by A.J. Longmore and S.B. Tritton with the UK 1.2 m Schmidt telescope (Longmore & Tritton 1980). It is generally noted that LoTr 1 belongs to the so-called 'Abell 35-type' group of PNe (Bond, Ciardullo & Meakes 1993) showing evidence of a binary system consisting of a cool central star (a rapidly rotating subgiant or giant) and an optically faint hot companion (a WD with effective temperature, $T_{\rm eff} \sim 10^5$ K) since these giant stars are too cool to ionize the surrounding nebula. Four PNe fell into this category: Abell 35 (hereafter, A35), LoTr 5 (Thevenin & Jasniewicz 1997), WeBo 1 (Bond, Pollacco & Webbink 2003) and Abell 70 (Miszalski et al. 2012, hereafter A70). However, Frew (2008) determined that A35 is most likely not a true PN,

but rather a Strömgren zone in the ambient interstellar medium (ISM). This claim is substantiated by Ziegler et al. (2012), who find that the central star may in fact have evolved directly from the extended horizontal branch to the WD phase (a so-called AGB-manqué, or 'failed', star). As such, we choose not to consider A35 in our comparisons among this group.

Another common factor amongst the A35 group is evidence for the existence of 'Barium (Ba) stars' (Bidelman & Keenan 1951) – Population I G/K-type giant stars that show an overabundance of carbon and s-process elements, in particular barium (Thevenin & Jasniewicz 1997). As discussed in detail in Ch. 1.3.2, a now-canonical model for the formation of these Ba stars states that they form not through CE evolution, as is the case for close binaries found within PNe, but rather via a wind accretion scenario (Boffin & Jorissen 1988). However, some exceptional systems exist that also experience similar enrichment within a close binary system, e.g. the Necklace nebula (Miszalski, Boffin & Corradi 2013) which possesses a carbon dwarf star. PN K 1-6 (Frew et al. 2011) is another potential candidate for this group of objects as it also shows evidence of possessing a G- or K-type giant (inferred from imagery, looking at both optical and 2MASS near-infrared colours) and a very hot sub-dwarf or WD (inferred from GALEX archival images) at its core. However, no stellar spectroscopy is available as yet to look for signs of chemical enrichment (Frew et al. 2011). More recently, Miszalski et al. (2013) presented evidence for a carbon and s-process enriched giant at the centre of the PN Hen 2-39. However, due to it being a newly investigated system, Hen 2-39 is not included in this study.

One important prediction to come out of the wind accretion model is that the accreting star, i.e. the future Ba star, also accretes angular momentum from the companion to become a rapid rotator (Jeffries & Stevens 1996; Theuns, Boffin & Jorissen 1996). Indeed, photometric monitoring of LoTr 5 (Thevenin & Jasniewicz 1997) and Webo 1 (Bond, Pollacco & Webbink 2003) has revealed that their cool components are in fact rapid rotators with a rotation period of a few days, thus providing further evidence for this formation scenario. This is further emphasised by the fact that Montez et al.

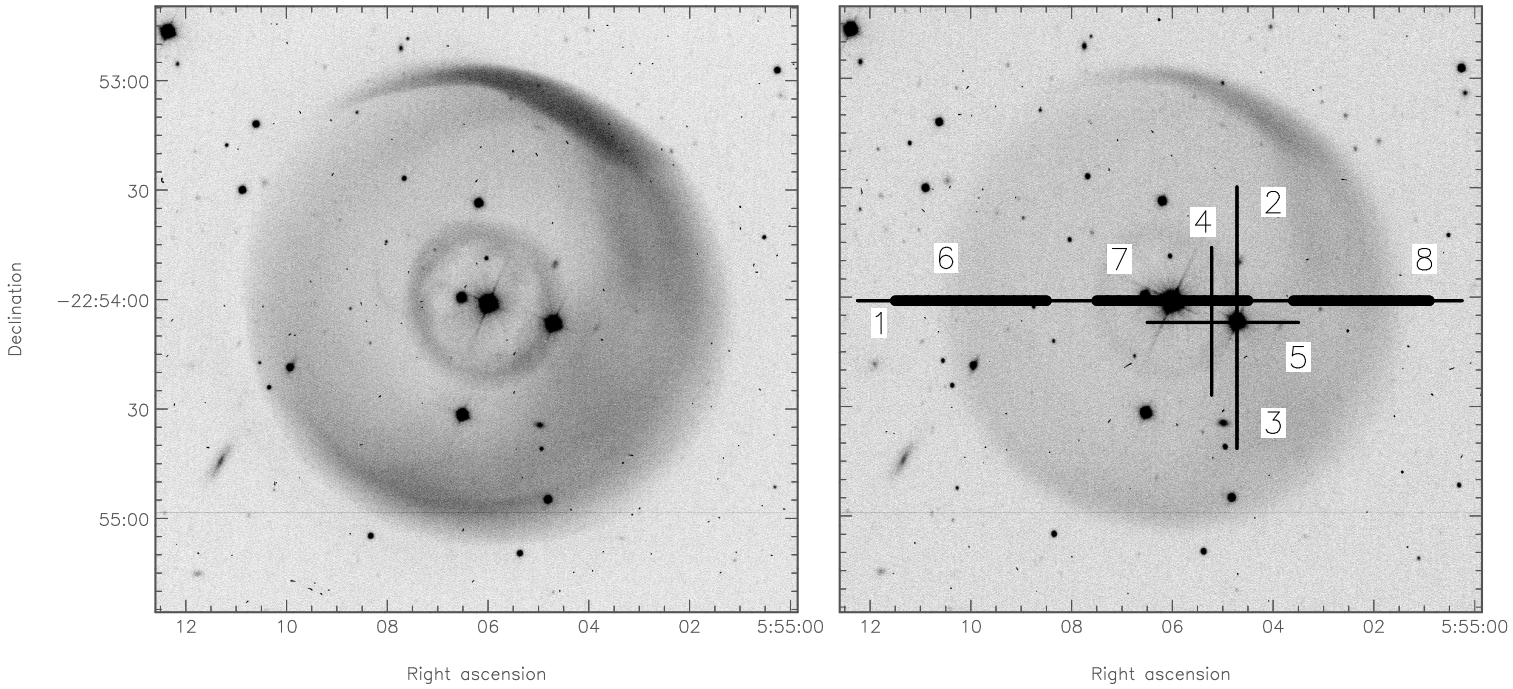

(a) (b)

Figure 4.1: Deep, narrowband images of PN LoTr 1, in (a) [O] and (b) Hα+[N]. North is to the top of the image, east is left. The central star is visible at α = 05:55:06.6, δ = −22:54:02.4. Overlaid in image (b) are the slit positions of the spatio-kinematic data presented in Sec. 4.2.1. Slit 1 (E–W) was acquired using NTT-EMMI and is centered on the central star. Slits 2–4 (N–S) and 5–8 (E–W, width of slits 6–8 exaggerated to clearly show the positioning due to overlapping with slit 1) were acquired using AAT-UCLES. The spectroscopic data for all slits were taken using the [O]λ5007 Å filter.

(2010) found that the X-ray emission from the binary central stars of LoTr 5 is most likely due to the chromospheric activity from a spun-up companion.

Most Ba stars are not observed to be within PNe, almost certainly because the lifetime of the PN is very short with respect to the lifetime of the stellar system. However, this does not completely rule out the possibility that some Ba stars may be formed without passing through a PN phase. There are a few examples of field stars that have been shown to consist of a rapidly rotating cool star linked to an optically faint hot component in a similar fashion to the A35 group, but without current evidence for a surrounding PN. HD 128220 (P = 872 d) is one such system, made up of an O subdwarf and a G0 giant companion (Bond, Pollacco & Webbink 2003). O subdwarfs overlap with CSPNe in terms of their log g and $T_{\rm eff}$, implying that they too are found to be in a post-AGB phase of evolution (Howarth & Heber 1990). 56 Pegasi is another example, whereby it possesses a system consisting of a K0 giant and a hot WD companion with evidence for an overabundance of Ba, and has an estimated orbital period of 111 d (Griffin 2006). In knowing that the chemical pollution process that formed the Ba central stars happened very recently – either during, or immediately prior to, the formation of the PN – makes it highly important to study such systems as A70 and WeBo 1, as it will allow us to gain greater insight into both the s-process within AGB stars and mass-transfer mechanisms.

In this chapter, photometric and spectroscopic observations of LoTr 1 and its central star are presented along with complementary data of A70 and WeBo 1, in order to try to relate the evolutionary processes of these three systems and see if they belong to a common ‘fellowship’ of s-process enriched, cool CSPNe inside ring-like nebulae.

4.2 Observations and Analysis

4.2.1 LoTr1

Imaging

The deep [O] and Hα+[N] images shown in Figs. 4.1 (a) and (b) were acquired on 2005 March 03 using the red arm of NTT-EMMI (Dekker, Delabre & Dodorico 1986). EMMI was used with the mosaic of two MIT/LL CCDs of 2048 × 4096 15μm pixels. The exposure time, $t_{\rm exp}$, in each filter was 1800 s, and the binning was set to 2 × 2 (≡ 0.33 arcsec pixel^{-1}). The seeing was ∼0.7 arcsec.

The images show LoTr 1 to have an apparent double-shell structure, with the central shell having a circular profile of angular diameter 47 ± 4 arcsec, and the outer shell a more irregular, but still roughly circular, appearance, with a diameter of 2 arcmin 26 arcsec ± 4 arcsec. Furthermore, in [O], the outer shell appears brighter in the north-west and south-east directions. This, coupled with the slight deviation from circular symmetry, could be considered evidence for an inclined, elongated structure, where the brighter areas result from a projection effect. Interaction with the ISM is also frequently invoked to explain deviation from symmetry and brightening of the nebular shell (e.g. Jones et al. 2010b); however, this would not produce the apparent axisymmetry in the nebular brightening as the nebula would only interact strongly with the ISM in the direction of its motion (Wareing, Zijlstra & O'Brien 2007).

Nebular spectroscopy

Longslit echelle spectroscopy was carried out using AAT-UCLES and NTT-EMMI, focusing on [O] emission over eight different slit positions (see Fig. 4.1b) in order to gain spatially resolved velocity profiles across a good sample of the nebula and subsequently build up the 3D environment (see Ch. 1.3.1 for more detail). The resulting spectra are then plotted as position–velocity (PV) arrays.

On 2005 March 03, a spectrum was acquired from the nebula using EMMI in its

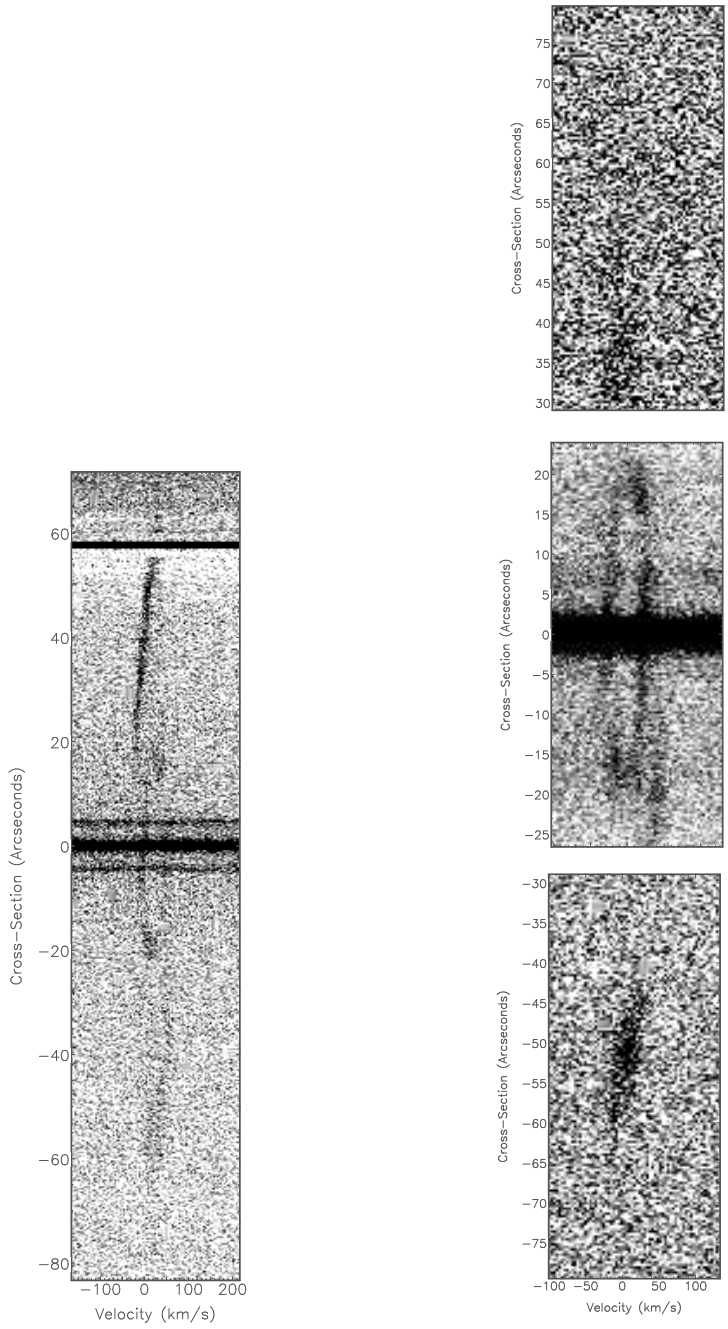

Figure 4.2: PV arrays showing reduced, longslit [O] NTT-EMMI and AAT-UCLES spectra of LoTr 1, both aligned E–W, to show the overall nebular structure. West is to the top of the array. The velocity axis is heliocentric velocity, $V_{\rm hel}$. The display scale has been modified to highlight the spatio-kinematic features referred to in the text. Cross-section 0 arcsec defines where the central star is found. The gap between the two CCDs in (a) is visible as a black strip across the frame at cross-section 58 arcsec (see the text for details).

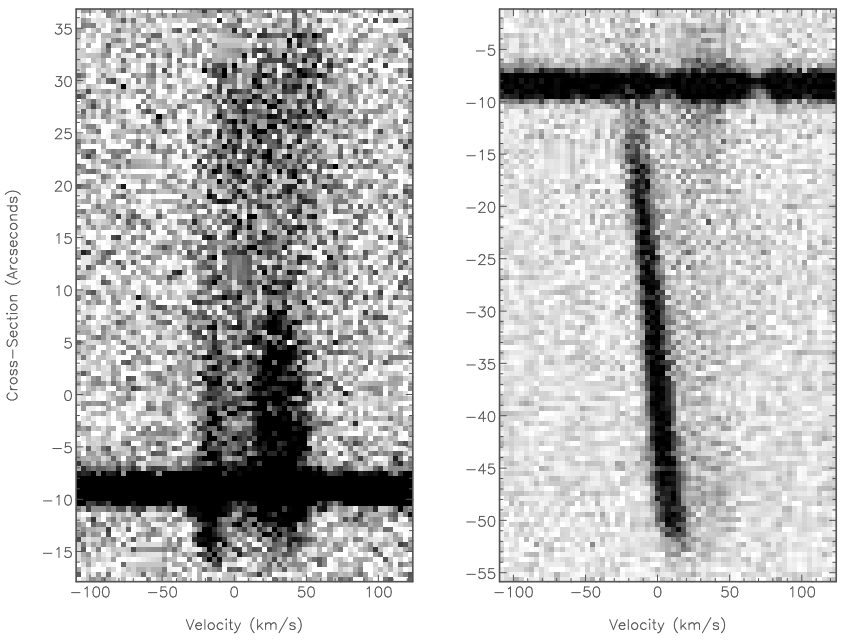

(a) Slit position 2

(b) Slit position 3

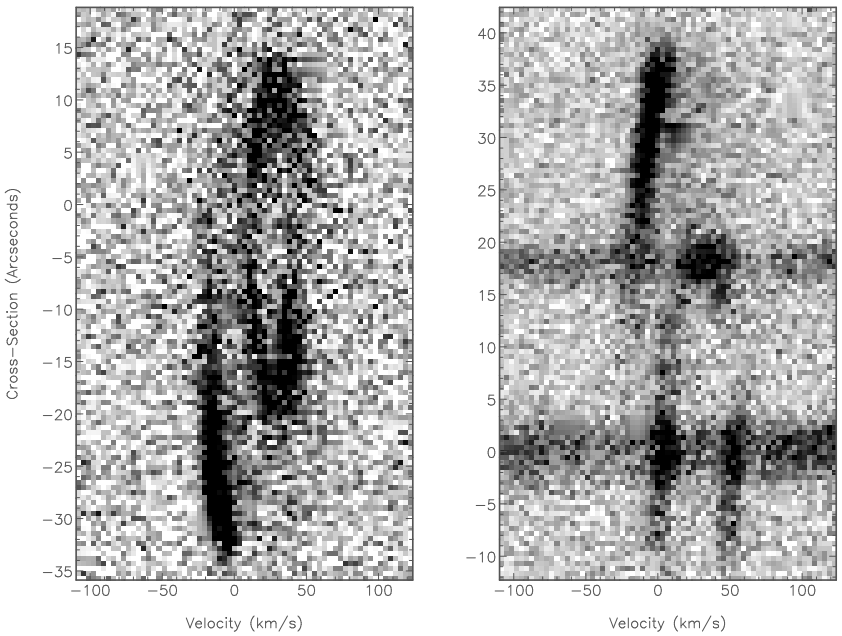

(c) Slit position 4

(d) Slit position 5

Figure 4.3: PV arrays showing reduced [O] AAT-UCLES spectra of LoTr 1. The velocity axis is heliocentric velocity, $V_{\rm hel}$. The display scale has been modified to highlight the spatio-kinematic features referred to in the text. Slits 2–4 are N–S (north is to the top of the array), slit 5 is E–W (west is to the top of the array). Cross-section 0 arcsec defines where the central star is found. The continuum of a field star is visible at cross-section −8 arcsec in (a) and (b), and at cross-section +18 arcsec in (d).

single order echelle mode, employing grating #10 and a narrowband [O] filter to prevent contamination from overlapping echelle orders. The maximum slit length of 330 arcsec and a slit width of 1 arcsec was used to give a resolution, R ∼ 54 000 (5.5 km s^{-1}). A 1800 s exposure was taken at a position angle (PA) of 90° crossing the central star (slit position 1 in Fig. 4.1b), and the data were 2 × 2 binned to give a spatial scale of 0.33 arcsec and a velocity scale of 3.9 km s^{-1} $pixel^{-1}$. The seeing was ∼0.7 arcsec.

On 2005 January 14, spectra were acquired from the nebula of LoTr 1 using the 79 lines mm^{-1} grating on AAT-UCLES. UCLES was operated in its longslit mode with a maximum slit length of 56 arcsec and a slit width of 1.97 arcsec to give a resolution R ∼ 20 000 (15 km s^{-1}). The EEV2 CCD (2048 × 4096, 13.5μm pixels) was used with binning of 2× 3, resulting in a pixel scale of 3.88 km s^{-1} $pixel^{-1}$ in the spectral direction and 0.48 arcsec $pixel^{-1}$ in the spatial direction. 1800 s exposures were taken at five different slit positions (shown in Fig. 4.1b) using a narrowband filter to isolate the 45th echelle order containing [O] emission line profile. Slits 2–4 were taken at a PA of 0°, and slit 5 was taken at a PA of 90°. The seeing during the observations was ∼2 arcsec. A further three slits (slit positions 6–8 in Fig. 4.1b) were acquired using the same instrument and CCD on 2013 January 3 with a seeing of ∼1.5 arcsec and a binning of 2 × 2 (≡ 0.32 arcsec $pixel^{-1}$ in the spatial direction). Here, a slit width of 1 arcsec was employed for slits 6 and 8 (R ∼ 45 000 ≡ 6.7 km s^{-1}) and 1.5 arcsec for slit 7 (R ∼ 30 000 ≡ 10 km s^{-1}). The slit width for slit 7 was altered to try to match the seeing conditions during the night. However, as all observations were carried out with the same binning in the spectral direction and the same grating resulting in them having approximately the same dispersion, they can all be used to qualitatively assess the spatio kinematic structure of the nebula (varying on scales much greater than the slit widths employed, due to the angular size of the nebula also being much greater than the slit width).

All the spectra were cleaned of cosmic rays and debiased appropriately, as described in Ch. 2.3. The AAT-UCLES spectra were wavelength calibrated against a

ThAr emission lamp, rescaled to a linear velocity scale appropriate for the [O] emission and corrected to heliocentric velocity, $V_{\rm hel}$. Due to the optical setup of NTT-EMMI, it was necessary to perform the wavelength calibrations accounting for spectral shifts using a long exposure (3600 s) ThAr emission lamp as described previously in Ch. 3.2.

The reduced nebular spectra of LoTr 1 are presented in Figs. 4.2 and 4.3 as PV arrays. In each PV array, cross-section 0 arcsec defines where the central star is found. In Fig. 4.2(a), the bright lines located around the central star at cross-sections +3 arcsec and -3 arcsec are most likely artifacts due to the comparative difference in brightness between the central star and the nebula (Jones et al. 2010a).

The closed velocity ellipses shown in the PV arrays presented in Figs. 4.2 (a), 4.3 (c) and the central PV array of 4.2 (b) (i.e. representing slit positions 1, 4 and 7) have a major axis which has the same length as the diameter of the inner shell (see Sec. 4.2.1), with no significant asymmetries visible. This is indicative that the nebular structure is indeed an isolated, closed shell or elongated ovoid viewed directly along the symmetry axis rather than a projection effect related to a bipolar structure being viewed end on. The expansion velocity, $V_{\rm exp}$ for the inner shell is measured to be 17 ± 4 km s^{-1} at the location of the central star, while the $V_{\rm exp}$ for the outer shell is measured to be 25 ± 4 km s^{-1} falling within the typical range for a PN (Weinberger 1989). Assuming typical expansion properties for the nebula (i.e. the velocity is proportional to distance from the central star), the latter velocity is then the maximum expansion velocity for an elliptical shell viewed pole-on, or the uniform expansion velocity of the shell in the case of a sphere. The heliocentric systemic velocity, $V_{\rm sys}$ of this central shell was determined to be 14 ± 4 km s^{-1}.

In slit 1 (Fig. 4.2a), emission associated with the outer shell is clearly detected outside of the central shell at cross-sections ~ 40 arcsec and ~ −40 arcsec (see Sec. 4.2.1). Here, the emission from the eastern side appears blue-shifted with respect to the nebular $V_{\rm sys}$, and the west appears red shifted; this is indicative of an inclined and extended structure, e.g. an elliptical nebula, where the approaching ‘lobe’ is tilted slightly to the

east of its receding counterpart. Consideration of the other slits presented in Fig. 4.3 (b), (c) and (d) confirms this asymmetry in the velocity profile across the nebula, but indicates that the symmetry axis may lie closer to the northeast–southwest direction than east–west. However, any deviation from the line of sight must be rather small given the almost circular appearance of the shell in the images (see Fig. 4.1).

Determination of the exact structure and inclination of the nebula would require a more extensive, higher S/N data set covering more of the physical extent of nebula (given the outer shell's faintness), and a detailed spatio kinematical model such as that presented in Jones et al. (2012b). However, it is clear from both the imaging and spectroscopy presented here that LoTr 1 shows a double-shelled structure with evidence for an elliptical and slightly inclined outer shell, and a morphologically similar inner shell at a different orientation.

Stellar photometry

The field of LoTr 1 has been observed by WASP-S between 2006 May 4 and 2012 February 17 with a total of 21407 photometric points obtained with the two cameras DAS 226 and 228. WASP-S is a wide field survey camera situated at SAAO, Sutherland, South Africa, and together with its northerly sister, SuperWASP-N, is designed to obtain extremely accurate photometry of bright stars in order to search for transits from exoplanets (see Pollacco et al. 2006, for a more detailed description of the facility, the data reduction and archive). Data mining tools and the public archive are discussed by Butters et al. (2010). After reduction through the instrument pipeline (Pollacco et al. 2006), the time series were examined with a simple Lomb–Scargle filter for periodic signal detection. From the light curves reproduced in Fig. 4.4 taken from Jones et al. (2011a), a period of 6.4 d was derived with a peak-to-peak amplitude of 0.061 mag. This is close to the value of 6.6 d with an amplitude of 0.1 mag in *V*, initially derived by Bond, Ciardullo & Meakes (1989). Given the period, this amplitude is probably too high to be considered due to irradiation effects (De Marco 2006), so the most likely explanation is that the periodicity is following spots on a cool star – the signature of a

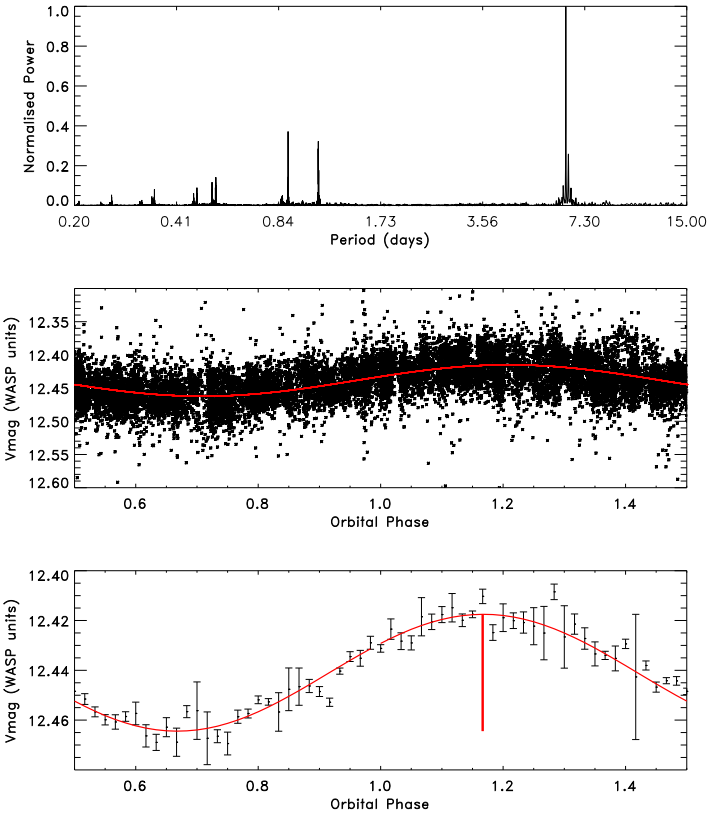

Figure 4.4: SuperWASP photometry of LoTr 1. Upper panel: periodogram showing a clear detection of periodicity at 6.3967 ± 0.0005 d. Middle panel: the data points folded on the period obtained from the periodogram. Lower panel: the data binned into phase bins, overlaid is a sinusoidal fit with a peak-to-peak amplitude of 0.061 mag. (Figure credit: D. Pollacco)

rapid rotator, analogous to the systems of LoTr 5 (5.9 ± 0.3 d; Thevenin & Jasniewicz 1997) and WeBo 1 (4.69 ± 0.05 d; Bond, Pollacco & Webbink 2003).

Stellar spectroscopy

On 2012 February 10, a high resolution spectrum was acquired of the central star of LoTr 1 using VLT-FORS2 (Appenzeller et al. 1998) with grism 1200g. FORS2 was operated with a maximum slit length of 6 arcmin and a 0.5 arcsec slit width (R ∼ 3000), and at a PA of 45°. The data were 2 × 2 binned to give a spatial scale of 0.25 arcsec pixel^{-1}, with a dispersion on the spectral axis of 0.3Å pixel^{-1}. A single 600 s exposure was taken under seeing of ∼ 0.7 arcsec.

On 2012 February 29, a low resolution spectrum was acquired of the central star of LoTr 1 using NTT-EFOSC2 (Melnick & Mendes de Oliveira 1995). 2×2 binning of CCD-40 was employed to give a spatial scale of 0.24 arcsec pixel^{-1} (2048×2048, 15μm pixels). A slit width of 1 arcsec was used at a PA of 0° to acquire the spectrum, giving dispersion on the spectral axis is 4.04Å pixel^{-1}. An exposure of $t_{\rm exp} = 300$ s was taken under 0.6 arcsec seeing.

The EFOSC2 data were eventually discounted due to difficulties encountered with the flux calibration of the spectrum and were not used in the subsequent analysis of the central star of LoTr 1. There was also an unusual high flux towards the blue end of the spectrum between ~ 5000–6000Å which could not be accounted for (see Fig. 4.5) and is most likely due to an instrumental, rather than physical, effect. As such, a proper fit could not be made to determine the spectral type accurately.

The FORS2 stellar data were extracted to 1D and flux calibrated against standard star Hz 4, and are presented in Fig. 4.6. All reductions were carried out using standard routines.

The central star of LoTr 1 was classified as a K1 III-type giant by comparing the flux calibrated FORS2 spectrum with UVES Paranal Observatory Project (POP) standard stars (Bagnulo et al. 2003) that had been rebinned and smoothed to match the resolution of the FORS2 data. Figure 4.8 is presented here to show a comparison of the overall fit of the spectrum between a K0 III giant (a) and the chosen K1 III giant (b) with LoTr 1. As is evident here, a K0 spectral type was discounted as the overall flux is too low, as well as there being a mismatch with some spectral features when compared with a K1 III giant (e.g. there is a bad fit to the block of lines that peak at around ~ 90 ergs cm^{-2} Å^{-1} at ~ 4590Å). Figure 4.9 shows the chosen K1 III spectral classification across the acquired spectral range to show the goodness of fit.

To refine the analysis and derive the possible s-process overabundance, the stellar spectral synthesis code of R. Gray, version 2.76[i], with models from Castelli & Kurucz (2003), was used by H. Boffin (private communication). The best-

[i] See http://www1.appstate.edu/dept/physics/spectrum/

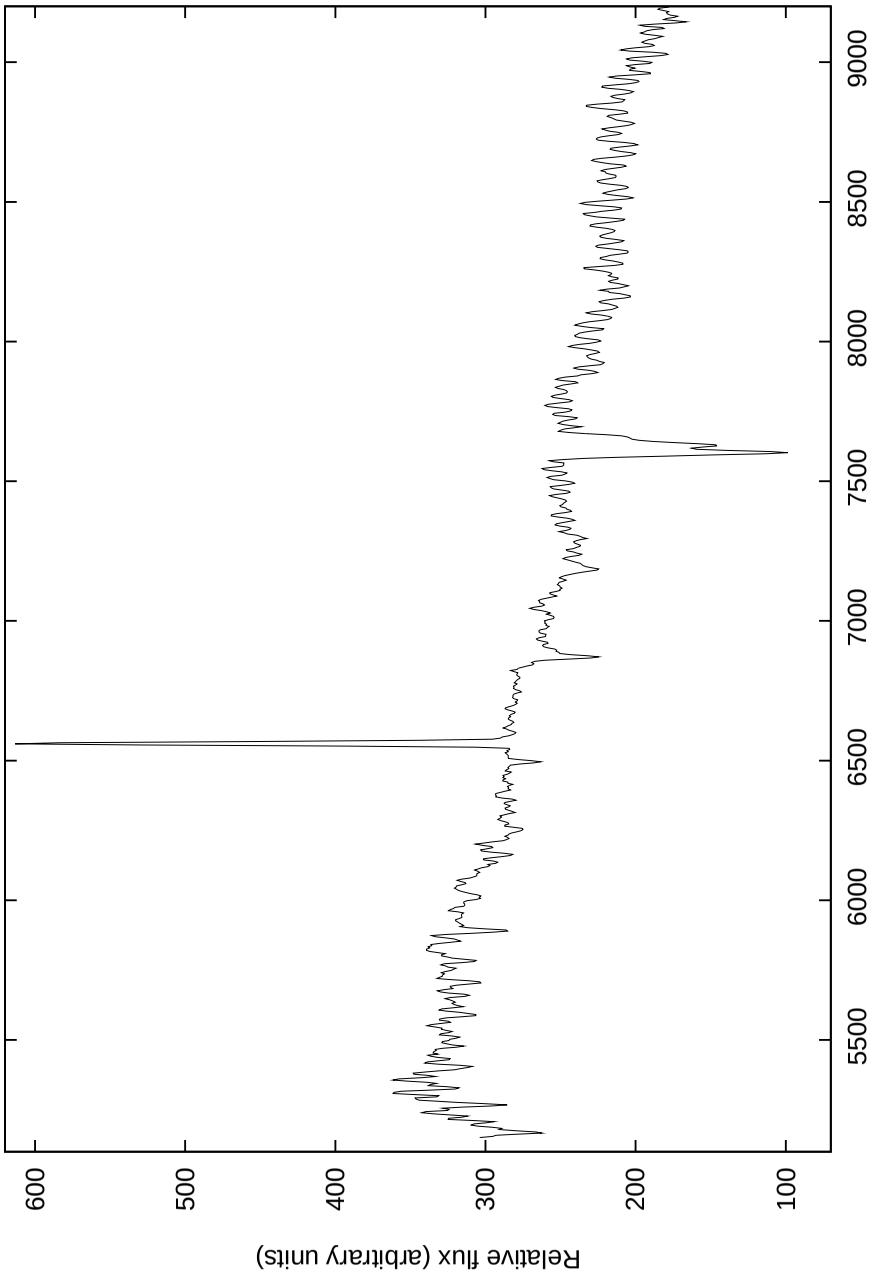

Figure 4.5: Flux calibrated spectrum of LoTr 1 from NTT-EFOSC2.

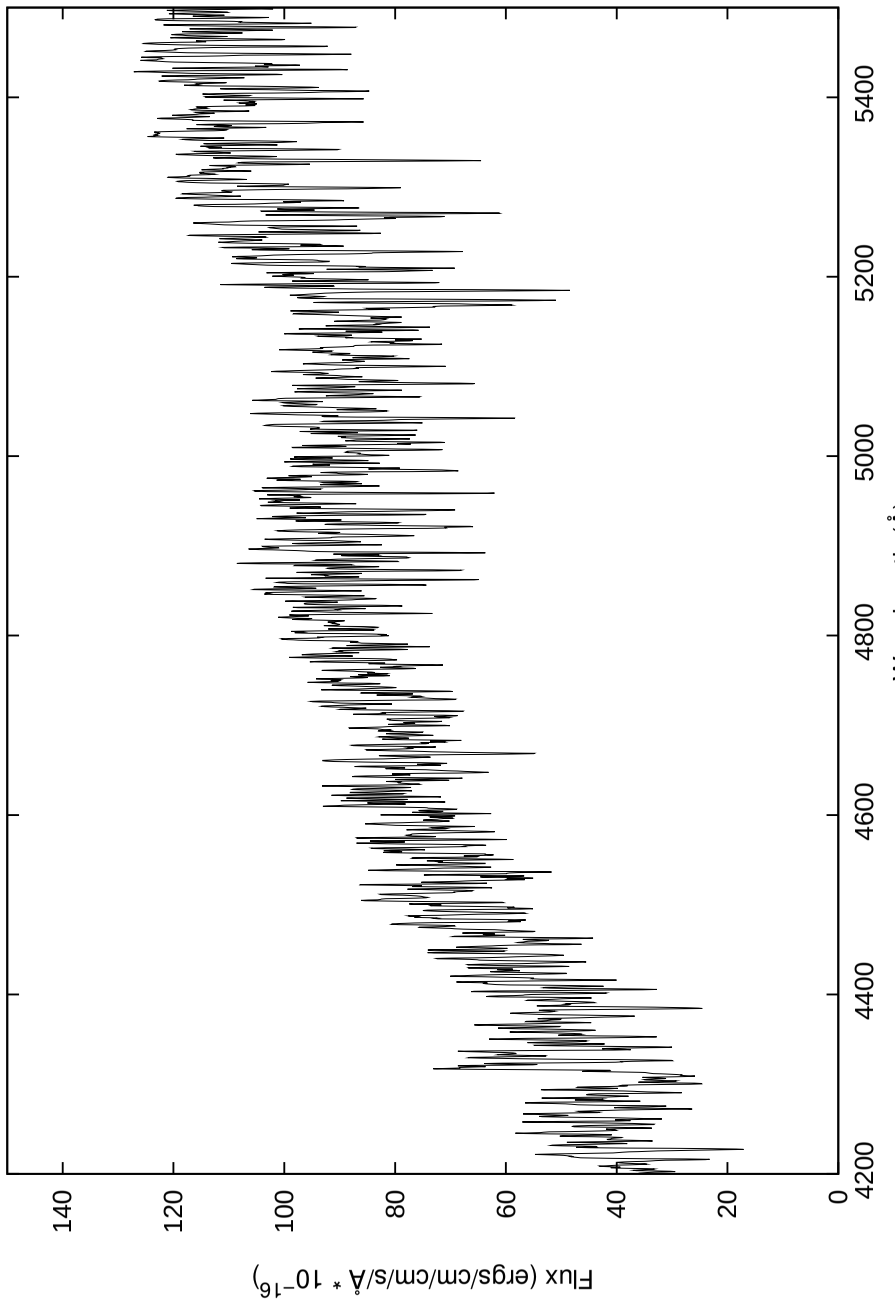

Figure 4.6: Flux calibrated FORS2 spectrum of the central star system of LoTr 1.

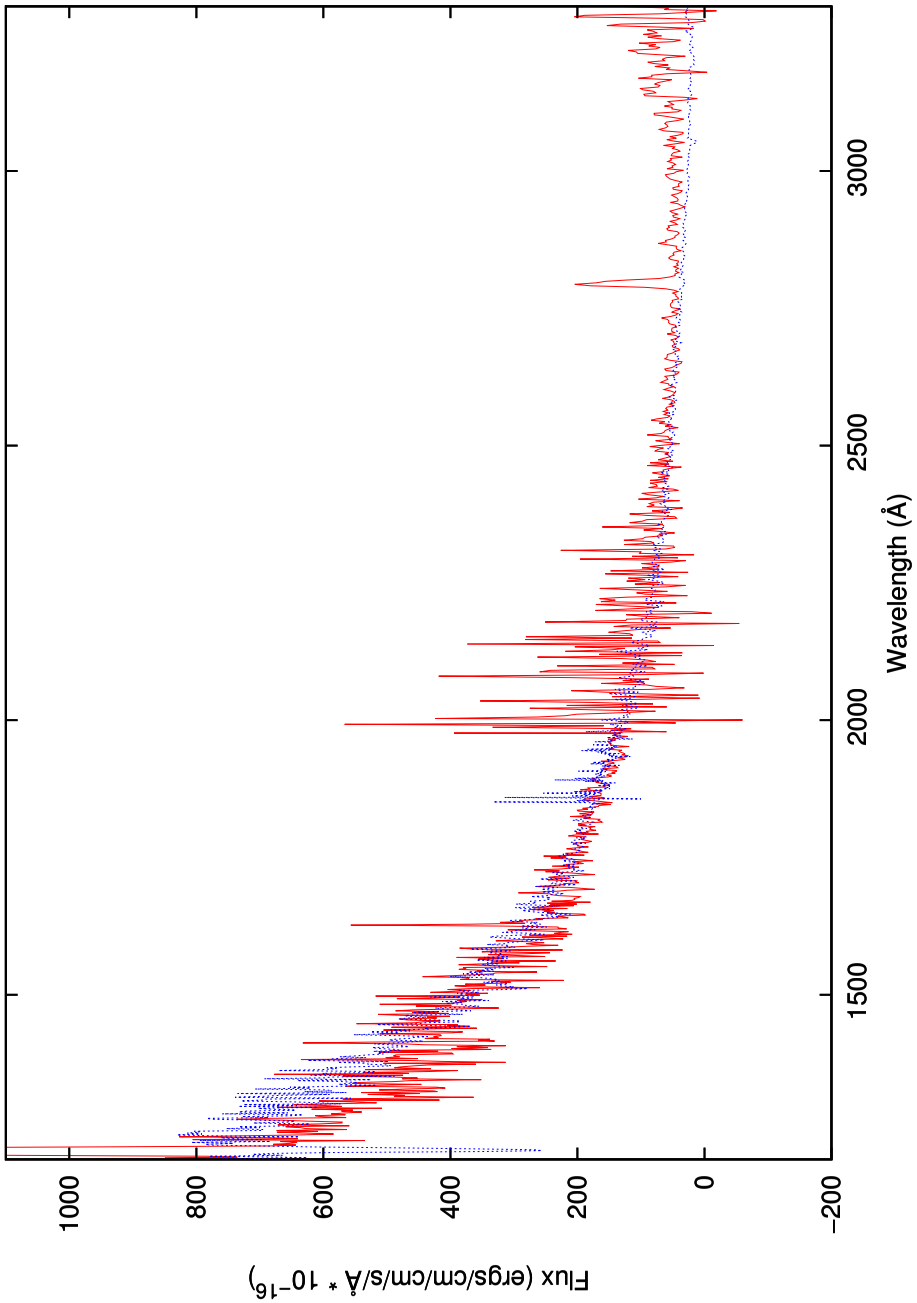

Figure 4.7: Flux calibrated IUE spectra of LoTr 1 (solid line), and of NGC 7293 (dashed line) used to determine the parameters of the WD. Note also the presence of the MgII emission at 2800 Å which is a sign of chromospheric activity from the cool companion (e.g. Jasniewicz et al. 1996; Montez et al. 2010).

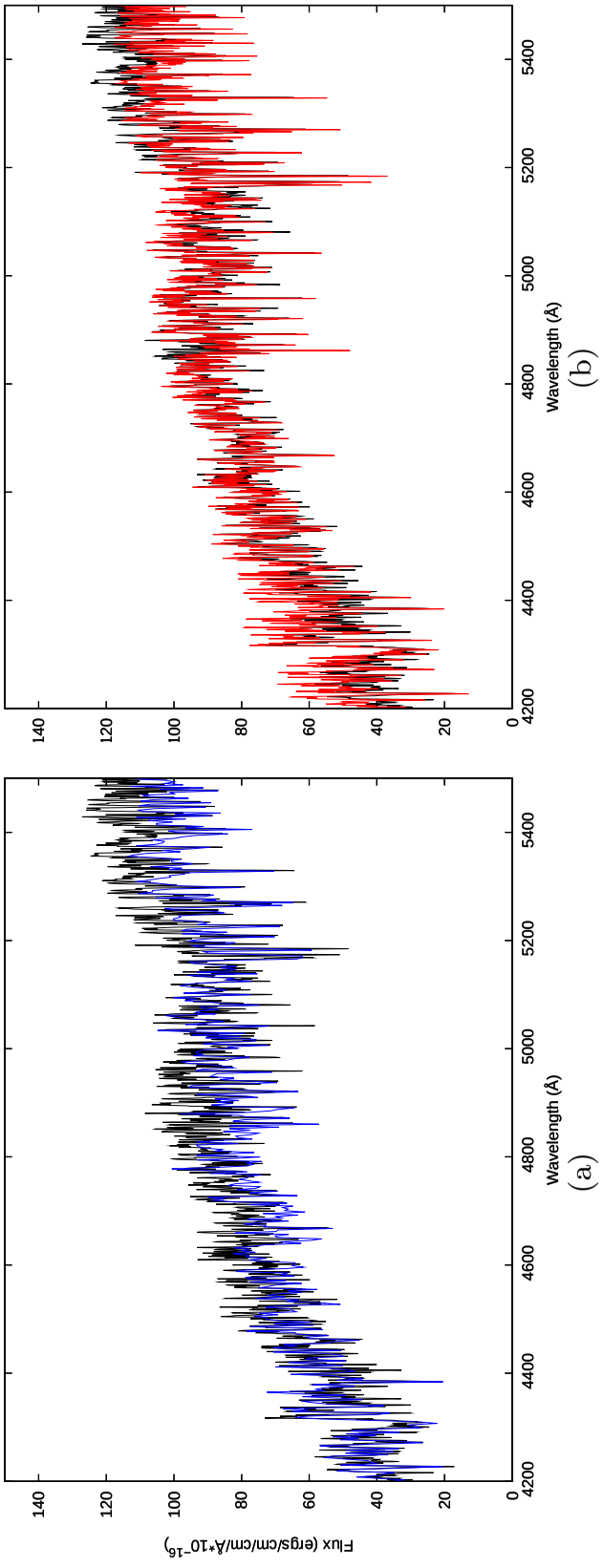

Figure 4.8: Figure showing the VLT-FORS2 stellar spectrum of LoTr 1 (black) overlayed with UVES POP stars of spectral type (a) K0 III (blue), and (b) K1 III (red) for a comparison of the fits.

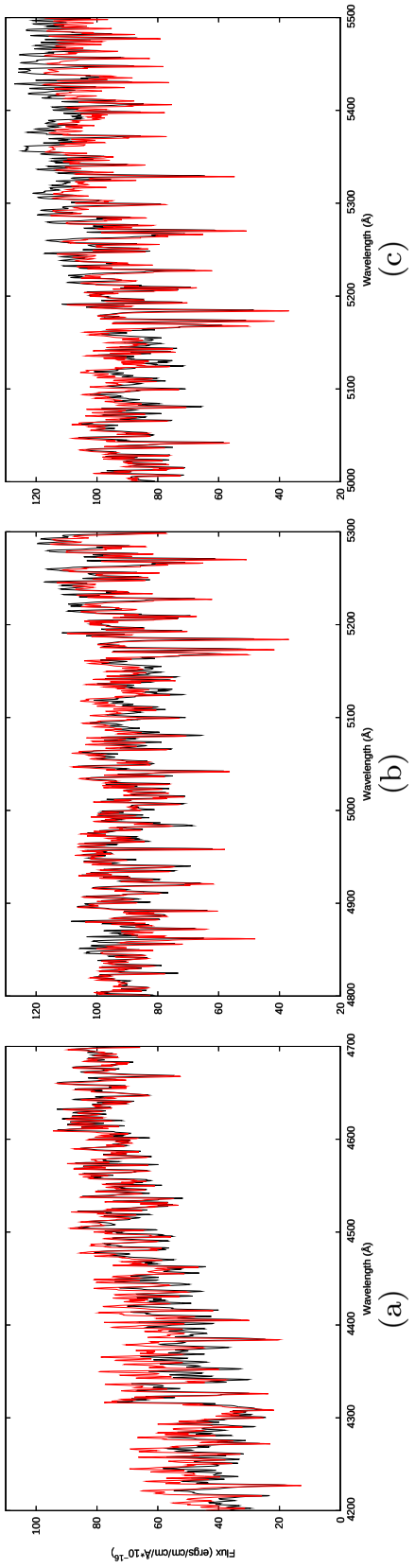

Figure 4.9: Figure showing the FORS2 stellar spectrum of LoTr 1 (black) overlayed with a UVES POP star of spectral type K1 III (red), to show how the goodness of the fit decreases towards the (a) far blue and (c) far red ends of the spectrum, compared to the fit in the centre, (b).

fitting parameters subsequently derived were $T_{\rm eff}$ = 4750 ± 150 K and log g = 2.0 ± 0.5, which is in agreement with the K1 III spectral type. Using the average value of the absolute magnitude, M_v = +0.7 for such a giant as given in Allen's *'Astrophysical Quantities'* (2000), the flux for the spectrum shown in Fig. 4.6 that allows the derivation of an apparent magnitude, m_v = +12.6 (accounting for 20% slit-losses) and extinction A_V=0.1285 (Schlegel, Finkbeiner & Davis 1998), one can determine a rough distance to the star of 2.6 kpc and a not-unreasonable radius of the giant of 11.5 $R_\odot$. Alternatively, one can use the average value of V derived from SuperWASP (see Fig. 4.4), i.e. V = 12.44, to derive a distance of 2.1 kpc. Note that this observed SuperWASP magnitude is likely to be contaminated by line emission and close field stars because of the broad observing band and large (14 arcsec) pixels. Therefore, it is preferable to use the distance derived from the flux calibrated spectra.

To check that the giant and the PN are indeed linked and not merely a chance superposition, the radial velocity difference between the nebular lines in the FORS2 spectrum and the giant star's absorption lines was computed, cross-correlating the acquired spectrum (shifted so that the nebular lines were at velocity zero) with the synthetic K1 III spectrum. The resulting stellar velocity of 4 ± 2 km s^{-1} with respect to the nebula implies that the cool central star and nebula are physically related.

The FORS2 spectrum was used to check for signs of Ba pollution at 4554Å. Figure 4.10 shows the FORS2 spectrum of LoTr 1 plotted alongside three synthetic spectra with various Ba enhancements, from [Ba/Fe] = 0.1 to 0.5. An overabundance of 0.5 or greater classifies the system as a definite Ba star, with a value of 0.2–0.5 being possibly a 'mild' Ba star (Pilachowski 1977). Due to the relatively low S/N and resolution of the spectrum, we are unable to determine a definitive value for the Ba abundance in LoTr 1, but we can clearly state that it is much less than 0.5 and therefore does not show any measurable Ba enhancement. This is contrary to both A70 and WeBo 1 (see Miszalski et al. 2012 and Bond et al. 2002, respectively), which both possess definite Ba stars.

On 2013 January 3, 3 × 30 min spectra were acquired from the CSPN of LoTr 1

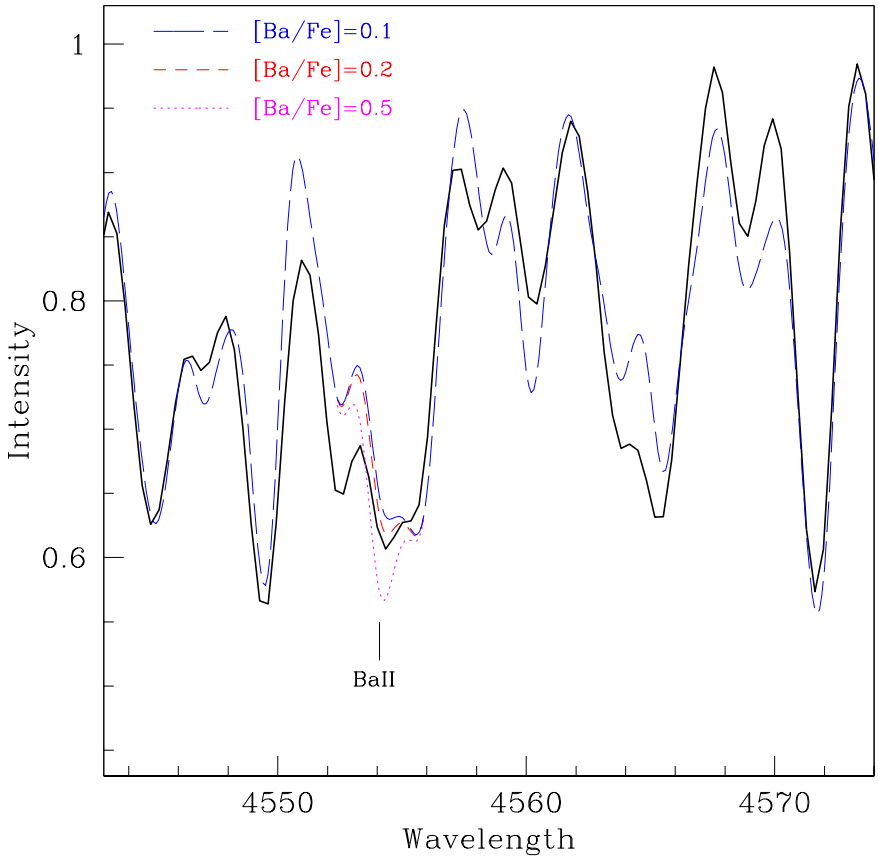

Figure 4.10: LoTr 1 FORS2 stellar spectrum (solid line) alongside three synthetic spectra with [Ba/Fe] = 0.1, 0.2, and 0.5, smoothed to match the FORS2 resolution and plotted over a wavelength range which includes the Ba 4554Å line. (Figure credit: H. Boffin)

using AAT-UCLES using the 79 lines mm^{-1} grating, operated in full echelle mode with a slit width of 1 arcsec to give a resolution R ~ 45 000. All spectra were reduced using standard routines, corrected to heliocentric velocity and then summed. Unfortunately, because of the large interorders in the spectra (UCLES operated in this mode gave non-continuous wavelength coverage from roughly 5200 to 8900Å across 19 orders with interorder spacing of 100–200Å), it is not possible to assess the Ba abundance as none of the available orders contain the Ba lines at 6141.7 and 6496.9Å. We have verified, however, that the iron lines are well fitted with a solar abundance and our preferred model, in agreement with what we derived from the FORS2 spectrum. Looking at the La 6390Å and Y 6222Å lines it is also clear that these elements are

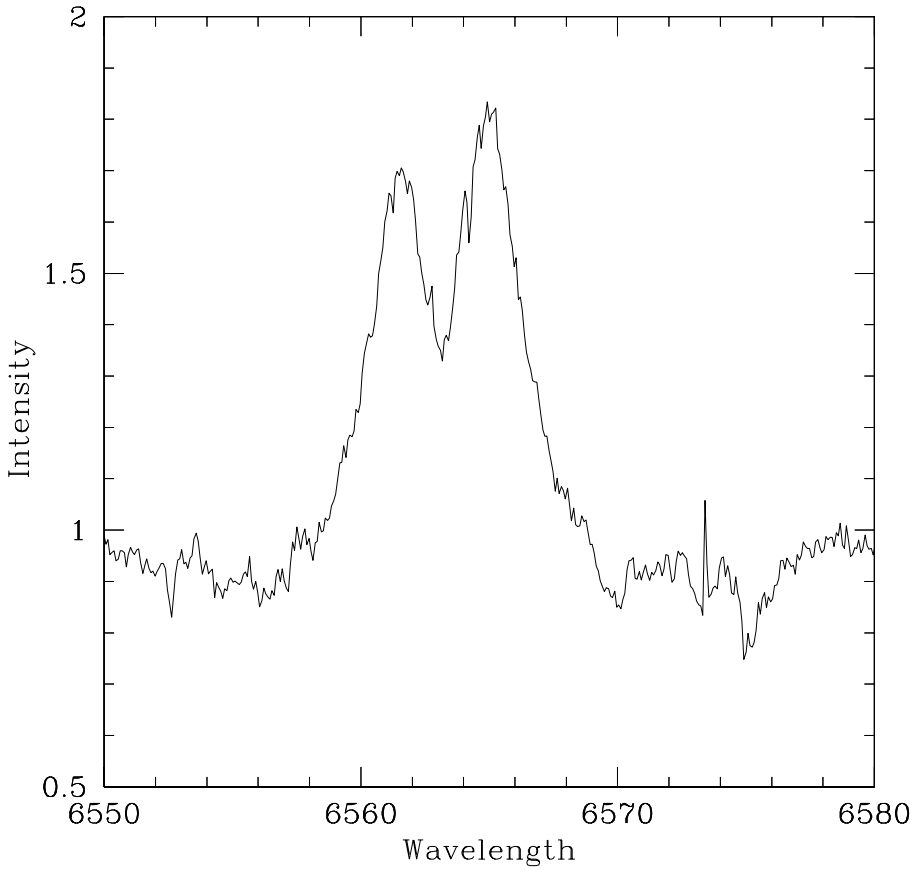

Figure 4.11: Hα emission seen in LoTr 1. (Figure credit: H. Boffin)

not overabundant, confirming the lack of s-process enhancement in LoTr 1.

The AAT-UCLES spectra allowed us to find that the stellar component of Hα is in emission (see Fig. 4.11). The line is very broad and is clearly double peaked, with an equivalent width of about 6Å and a velocity spread of 572 km s^{-1}. Using the method of Hodgkin, Jameson & Steele (1995), H. Boffin derived an Hα luminosity $L_{\mathrm{H}\alpha}$ = 0.044 L$_{\odot}$. With the above estimated total luminosity of the star ($L_{*} \sim 60\ L_{\odot}$), this gives a value $\log L_{\mathrm{H}\alpha}/L_{*} = -3.12$.

Such Hα double peaked emission lines have been found in LoTr 5 (Jasniewicz et al. 1994; Strassmeier, Hubl & Rice 1997) and A35 (Acker & Jasniewicz 1990; Jasniewicz et al. 1992), but the origin is still unknown. Rapidly rotating giants, such as RS CVn or FK Com stars, are known to have high chromospheric activity which is often revealed by

emission cores in some lines. Indeed, Acker & Jasniewicz (1990) find a modulation of the Hα emission line with the rotation phase, while Jasniewicz et al. (1992) postulate that the variable double peaked emission line is the result of an overlap between an absorption and an emission line at Hα, with the possibility for the absorption component to be formed in the photosphere or through a self-absorption process as in Be stars. However, the measured FWHM velocity seems too high to be caused by mass motions inside the chromosphere, while the luminosity is too small to be due to accretion. Such double peaked emission is also sometimes found in symbiotic stars (detached systems which interact via wind accretion). A few of them, out of an outburst event, produce bipolar nebulae very similar to PNe. It turns out that many symbiotic stars show double Hα profiles (e.g. Schild, Muerset & Schmutz 1996; Burmeister & Leedjärv 2009), which might be caused by a narrow absorption component from the giant overlaid with very broad Hα emission from high velocity jets at the core of the system, or by disc-like structures. It would thus be of interest to further study the possible link between LoTr 1 and symbiotic stars.

A spectrum of the central star system of LoTr 1 was acquired using the International Ultraviolet Explorer (IUE) satellite by Bond, Ciardullo & Meakes (1989). Presented here in Fig. 4.7, it indicates a strong UV continuum of $T_{\rm eff} \geq 10^5$ K. Comparing this IUE spectrum to a known WD within NGC 7293 (d = 219^{+27}_{-21} pc, m_v = +13.5; Harris et al. 2007) gave us a reasonable fit: $T_{\rm eff} \geq 1.23 \times 10^5$ K and R = 0.017 $R_\odot$. Based on values of D = 2 arcmin 22 arcsec ± 4 arcsec, and $V_{\rm exp}$ = 25 ± 4 km s^{-1} at a distance of 2.6 kpc, we derived a kinematical age of 33 000 ± 9000 yrs for the outer nebular shell. For the inner shell, with given values of D = 47 ± 2 arcsec and $V_{\rm exp}$ = 17 ± 4 km s^{-1}, the age is derived as 16 000 ± 6500 yrs. Using the white dwarf evolutionary curves from Bloecker (1995) and assuming an average remnant mass of 0.6 $M_\odot$, we derived a stellar temperature at the age of the PN of approximately 120 000 K. The derived radius and age of LoTr 1 are consistent with Bloecker's evolutionary curves.

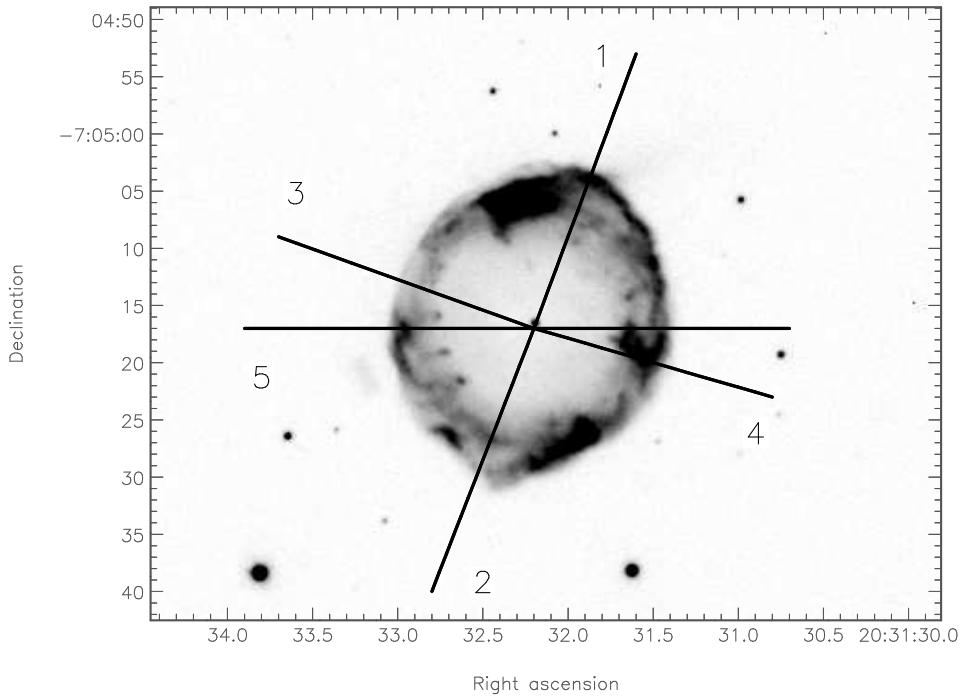

Figure 4.12: Hα+[N] image of A70 showing all slit positions. Slits 1–4 were acquired in [O] using VLT-UVES, and slit 5 was acquired in Hα and [O] using SPM-MES. The central star is visible at α = 20:31:32.2, δ = −07:05:17.0.

4.2.2 A70

Imaging

The Hα+[N] image of A70 shown in Fig. 4.12 was acquired on 2012 July 08 using FORS2, with an exposure time of 60 s and seeing of 0.8 arcsec. At first glance the image shows a general ring-like appearance similar to that of PNe such as SuWt 2 (Jones et al. 2010a); however, just as noted by Miszalski et al. (2012), closer inspection reveals a 'ridged' profile more like that of a bipolar nebula viewed end-on (e.g. Sp 1; Jones et al. 2012a). Furthermore, this image shows in detail the low-ionization knots first identified by Miszalski et al. (2012). Many of these structures seem to be akin to the cometary globules seen in the Helix Nebula (dense condensations of molecular gas embedded in the ionized nebula; see Meaburn et al. 1992), with knotty heads closest to the nebula centre and extended tails reaching out towards the outer rim. Extended material is also visible outside the east-southeasterly edge of the nebular ring (the

emission visible to the north of the ring originates from a background field galaxy).

Assuming the 'ring' is a physical structure rather than a projection effect, the inclination of the nebula can be derived by deprojection. The angular size of the nebula was determined to be 44 × 38 arcsec ± 2 arcsec, falling in line with the previously given value of 45.2 × 37.8 arcsec by Tylenda et al. (2003), giving an inclination of 30° ± 10°.

Nebular Spectroscopy

On 2011 June 10–11, high-resolution data of the nebula of A70 were acquired in [O] using grating #3 on the visual-to-red arm of VLT-UVES (Dekker et al. 2000). UVES was operated in its 30 arcsec longslit mode with a 0.6 arcsec slit width (R ∼ 70 000, 4.3 km s^{-1} $pixel^{-1}$) to give a spatial scale of 0.17 arcsec $pixel^{-1}$. A filter was used to isolate the [O] emission lines and prevent contamination from overlapping orders. The seeing was between 0.5 arcsec and 0.7 arcsec for all observations. Four 1200s exposures were taken over four different slit positions. Slits 1 and 2 were taken with VLT-UVES at a PA of 160° and slits 3 and 4 at a PA of 70°, to line up with the major and minor axis of the nebula, respectively. Slit 5 was acquired in both [O] and Hα on 2011 May 15 using SPM-MES (Meaburn et al. 2003; López et al. 2012). The full slit length of 5 arcmin was used with a slit width of 150μm (≡ 2 arcsec, R ∼ 30 000), and taken at a PA of 90°. The data were 2 × 2 binned to give a spatial scale of 0.75 arcsec $pixel^{-1}$. The seeing was ∼ 3 arcsec.

The nebular spectra acquired from VLT-UVES shown in Fig. 4.13 show two highly filamentary components, one red shifted and one blue shifted that are roughly symmetrical, joined by bright knots of emission where the slits cross the nebular ring to form a closed velocity ellipse in both axes. These filamentary and irregular structures are typical of disrupted nebulae, where instabilities have begun to structurally deform the shell (Guerrero & Miranda 2012), and clearly show that A70 is not simply an inclined ring but instead has 'bubbles' extending in the line of sight. It is reasonable to assume that these bubbles form a closed and axisymmetric structure. The bright emission at the

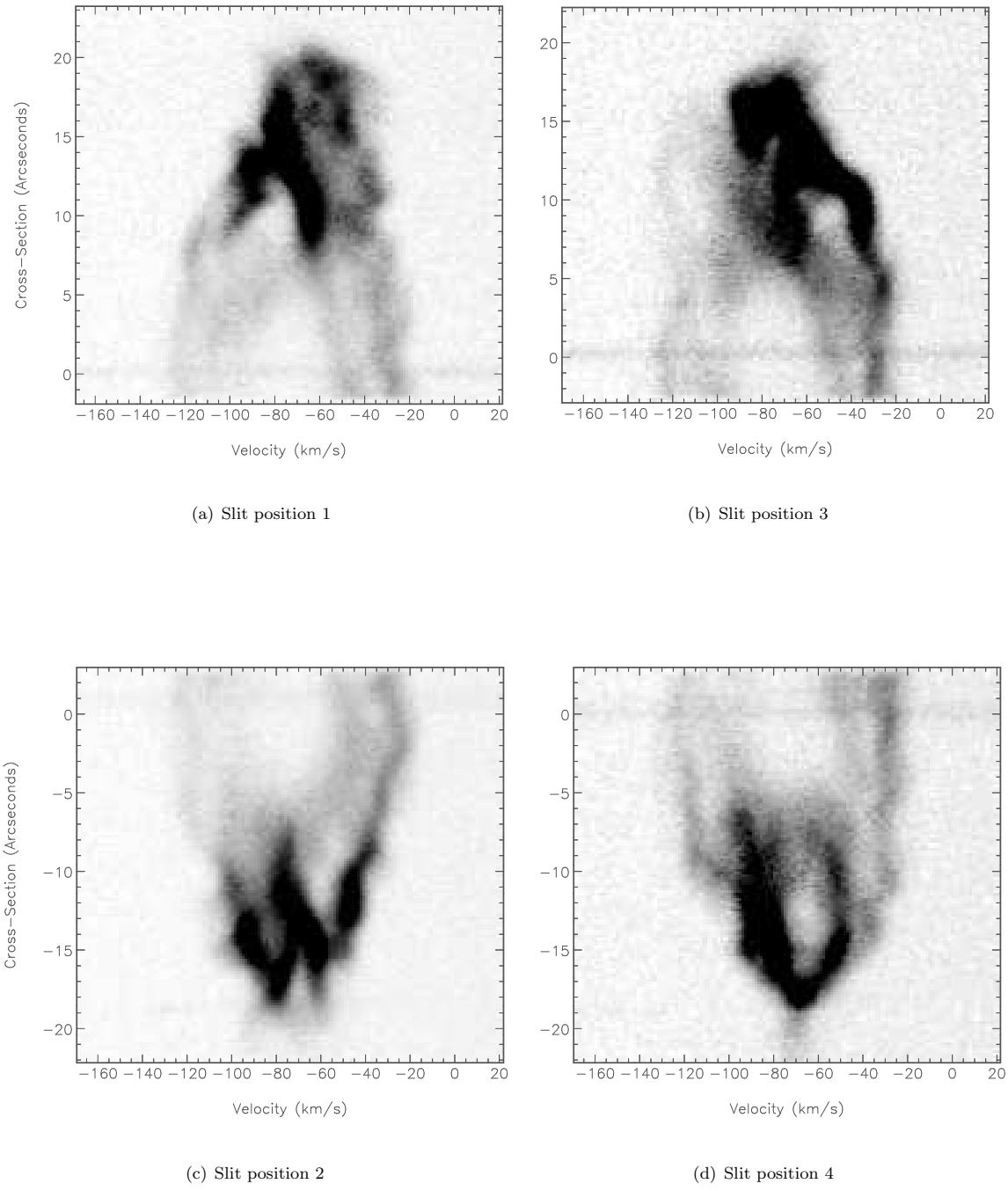

(a) Slit position 1

(b) Slit position 3

(c) Slit position 2

(d) Slit position 4

Figure 4.13: PV arrays showing reduced VLT-UVES spectra in [O] from A70. Figures (a) and (c) show emission from the major axis, (b) and (d) are from the minor axis. Positive spatial offsets are to the northern (1 and 2) or eastern (3 and 4) ends of the slits.The velocity axis is heliocentric velocity, $V_{\rm hel}$. The display scale has been modified to highlight the spatio-kinematic features referred to in the text. Cross-section 0 arcsec defines where the central star is found.

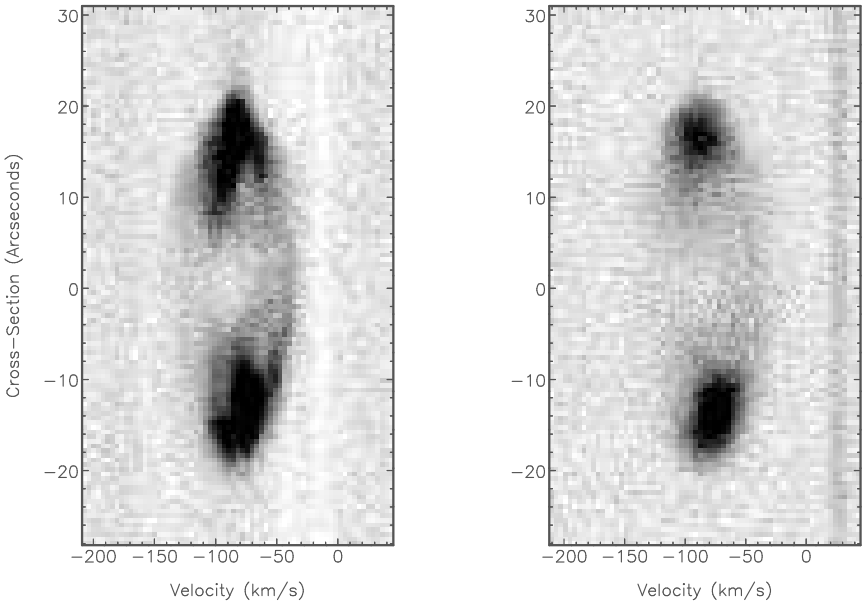

(a) Slit position 5, [OIII] (b) Slit position 5, Hα

Figure 4.14: PV arrays showing reduced Hα and [O] SPM-MES spectra of A70. Emission is through the horizontal axis (slit 5 in Fig. 4.12). The velocity axis is heliocentric velocity, $V_{\rm hel}$. The display scale has been modified to highlight the spatio kinematic features referred to in the text. Cross-section 0 arcsec defines where the central star is found.

extremes of each slit indicate that the nebula may have a cusped waist, with slits 1 and 2 showing the 'crow's foot'-like structure typical of narrow-waisted nebulae viewed along their symmetry axis (Jones et al. 2012b). However, there is a clear brightening in these regions and those of slits 3 and 4, consistent with a bright ring. We therefore deduce that A70 is composed of such a bright ring, encircling the waist of a disrupted and faint bipolar shell.

Using the same spectra, a polar expansion velocity $V_{\rm exp}$ for A70 was calculated to be 39 ± 10 km s^{-1}. This is in agreement with the value for expansion velocity of $V_{\rm exp}$ = 38 km s^{-1} given by Meatheringham, Wood & Faulkner (1988), although no error was quoted. A $V_{\rm sys}$ of -73 ± 4 km s^{-1} was determined for the nebula, which is consistent with the value of -72 ± 3 km s^{-1} by Miszalski et al. (2012). The kinematical age of A70 was determined to be 2700 ± 950 yrs kpc^{-1}. Taking the distance to the nebula to be 5 kpc, as given by Miszalski et al. (2012), this gives an overall kinematical age for

A70 of the order of 13 400 ± 4700 yrs.

The limited depth and resolution of the MES-SPM spectra offer little extra to the discussion of the nebular morphology and kinematics, other than to show that there is no major difference between the emission in Hα and that in [O]. They are shown here in Fig. 4.14 mainly for comparison with similar data acquired from WeBo 1, which will be discussed in Sec. 4.2.3.

4.2.3 WeBo 1

Imaging

The deep Hα+[N] image shown in Fig. 4.15 (a) is the result of coadding 2 × 120 s exposures, each with seeing better than 1.2 arcsec, acquired as part of the INT/WFC Photometric Hα Survey (IPHAS) survey (Drew et al. 2005) using the Wide Field Camera (WFC) on the 2.5m Isaac Newton Telescope (INT) based at the Observatorio Roque de los Muchachos, La Palma. The [O] image shown in Fig. 4.15(b) was acquired using the same instrument on 2010 September 9, with an exposure time of 1200 s and under seeing of 1.4 arcsec.

The images show another ring-like morphology, although structurally different to A70 (see Sec. 4.2.2), with a pronounced inner edge and fainter, more extended emission around its entire circumference. The ring is particularly diffuse in [O], as shown by the lack of a visible inner edge. Similar extended emission is also found in SuWt 2 (Jones et al. 2010a) and HaTr 10 (Tajitsu et al. 1999), where the ring is actually the waist of an extended bipolar structure, possibly indicating that WeBo 1 may display the same morphology but with as yet undetected, very faint lobes. In SuWt 2, Jones et al. (2010a) attribute this extended material to structural and brightness variations across an irregular toroidal structure; however (particularly in the light of the Hα+[N] spectra acquired – see Fig. 4.16), WeBo 1 shows a much more regular and even ring-like shape, indicating that this is more likely an intrinsic structural property, i.e. a tear drop rather than circular shaped cross-section.

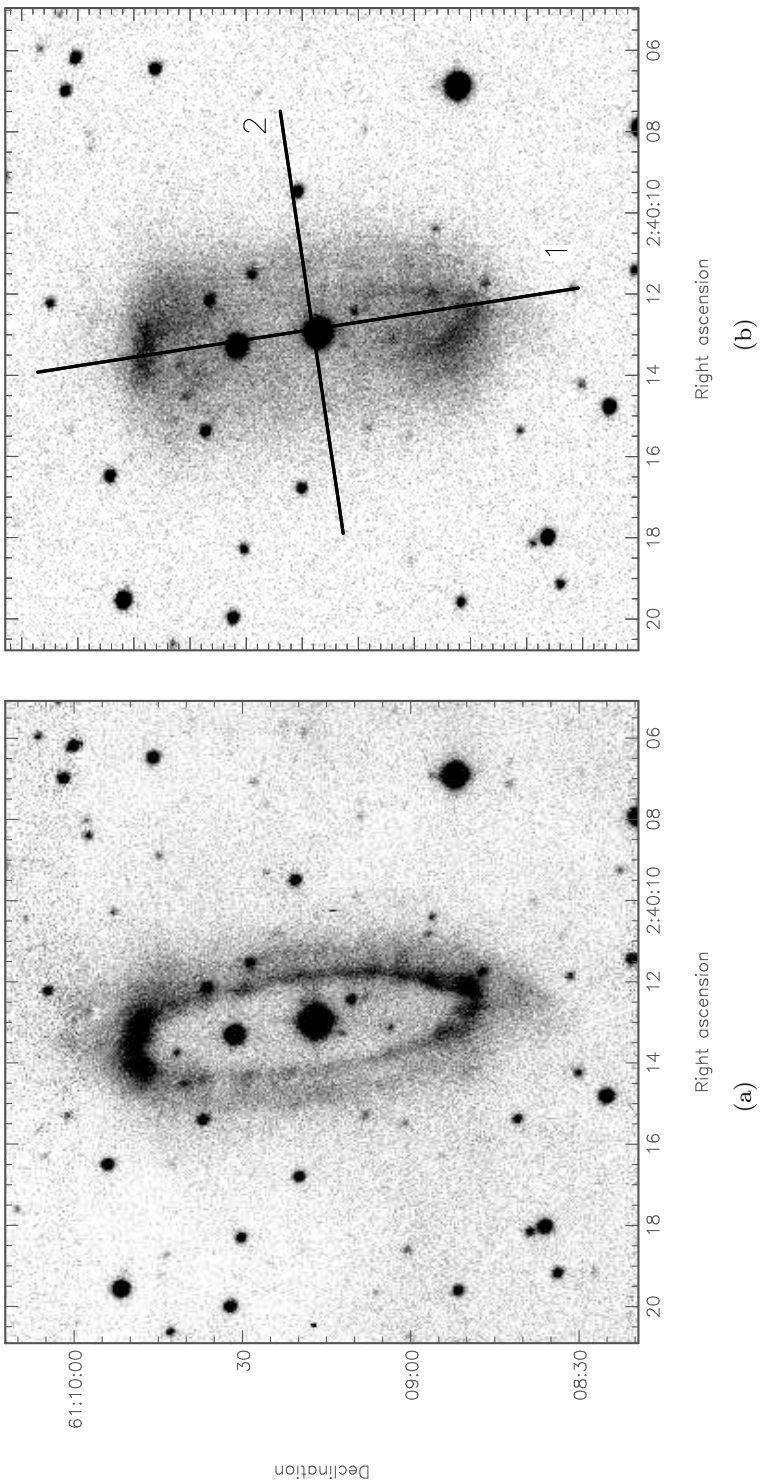

Figure 4.15: Images of PN WeBo 1 in (a) Hα+[N] and (b) [O], with (b) showing the two slit positions. Both slits were acquired in [N] and [O] using SPM-MES. The central star is visible at α = 02:40:13.0, δ = +61:09:17.0. North is to the top of the images, east is left.

Smith, Bally & Walawender (2007) deprojected the ring of WeBo 1, determining that it is seen almost edge-on with an inclination of 75 ± 3° with an inner-ring radius of ∼ 25 arcsec, which is consistent with the ring dimensions of 64 × 22 arcsec given by Bond, Pollacco & Webbink (2003) and as measured from the images presented here (65 × 20 arcsec ± 4 arcsec).

Nebular Spectroscopy

On 2010 December 10, spectra were acquired of WeBo 1 in both Hα+[N] and [O] using SPM-MES. The maximum slit length of 5 arcmin was used with a slit width of 150μm (≡ 2 arcsec, R ∼ 30 000) for each filter. The data were 2 × 2 binned to give a spatial scale of 0.75 arcsec pixel^{-1}. Slit 1 was taken at a PA of 353° and slit 2 was taken at a PA of 263° to cover the major and minor axes of the nebula, respectively. The seeing was ∼1.5 arcsec. Due to the Hα profiles having high galactic background emission, only the background-subtracted [N] and [O] are presented here. The reduced PV arrays are presented in Fig. 4.16.

Just as in the imagery (see Sec. 4.2.3), the [N] profiles show well defined emission originating from the ring, while the [O] is much more diffuse. The [N] profiles from both slit positions show strong emission at the inner edge of the ring, with slightly fainter material (also with a lower velocity dispersion) reaching out to greater angular extents. This is consistent with the tear drop cross-section interpretation presented in Sec. 4.2.3. The [N] profile from slit 1 shows little velocity difference between the emission originating from the two opposing sides of the ring, indicating that the slit is roughly perpendicular to the PA of the nebular symmetry axis; therefore, the deprojected velocity difference of the two sides of the ring in slit 2 should offer a good measure of the ring's expansion velocity. Taking the nebula inclination to be 75°, the deprojected expansion velocity for the ring was calculated to be $V_{\rm exp}$ = 22.6±10 km s^{-1}.

A $V_{\rm sys}$ of -6 ± 4 km s^{-1} was calculated for the nebula. The kinematical age of WeBo 1 was determined to be of the order of 7300 ± 3700 yrs kpc^{-1}. Taking the

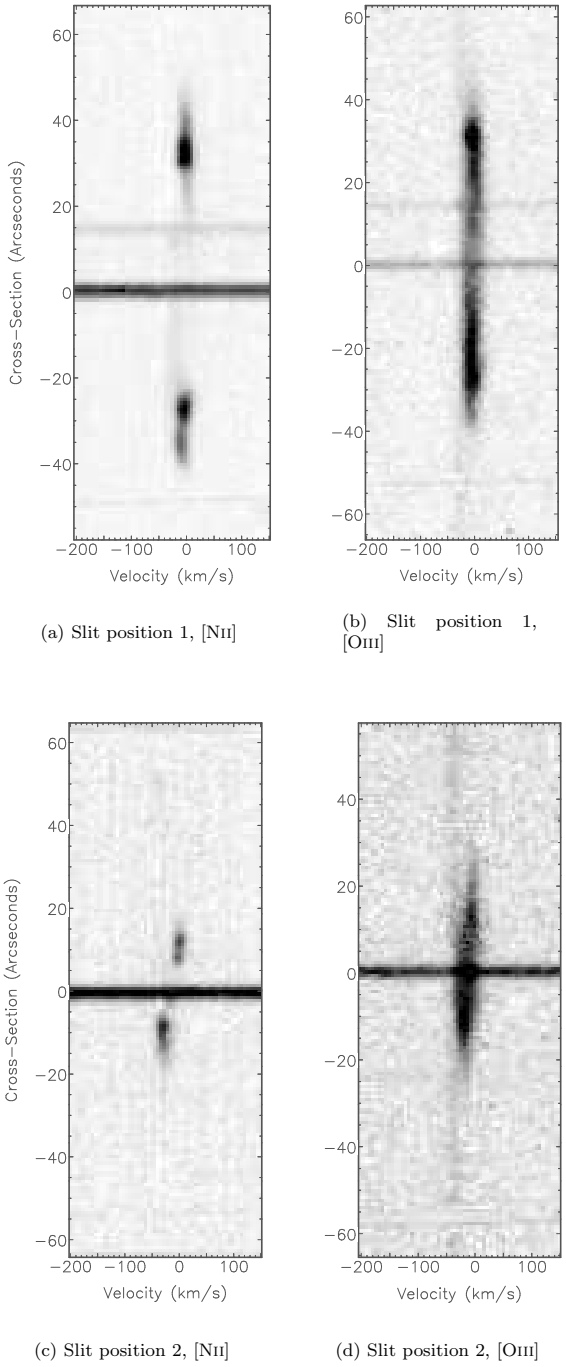

(a) Slit position 1, [NII]

(b) Slit position 1, [OIII]

(c) Slit position 2, [NII]

(d) Slit position 2, [OIII]

Figure 4.16: PV arrays showing reduced [N] and [O] SPM-MES spectra of WeBo 1. Figures (a) and (b) show the [N] and [O] emission from slit 1, (c) and (d) from slit 2 (see Fig. 4.15). North is to the top of the array. The velocity axis is heliocentric velocity, $V_{\rm hel}$. The display scale has been modified to highlight the spatio-kinematic features referred to in the text. Cross-section 0 arcsec defines where the central star is found. The continuum of a field star is visible at cross-section +15 arcsec in (a) and (b).

distance to the nebula to be 1.6 kpc (Bond, Pollacco & Webbink 2003), this gives an overall age for WeBo 1 of 11 700 ± 5900 yrs. [ii]

No clear evidence of lobes or extended nebular structure are detected in the spectra, unlike for A70 (see Sec. 4.2.2); however, faint material detected inside the ring on the [N] PV array of slit 1 could be consistent with such a structure. Deeper, higher resolution spectra are required to confirm the nature of this emission, but it is safe to say that if any lobes are present they are significantly fainter than those of A70, as its lobes were still clearly observable in the SPM-MES spectra (see Fig. 4.14).

4.3 Discussion

4.3.1 The A35 group and PN mimics

A35 - the archetype of the class of PNe discussed in this paper – has recently been shown to be a PN mimic. It is, therefore, critical to establish the true nature of the objects considered here before beginning a comparison. We restrict our analysis to the three PNe presented in this work, and exclude both A35 (which is no longer considered a true PN) and LoTr 5 (which is a considerably more complex case and discussed in more detail in Frew 2008; see also Graham et al. 2004).

Frew & Parker (2010) present a 'recipe' for determining whether we can classify an object as a true PN or not, parts of which we can apply to the nebulae presented here.

- Presence of a hot, blue central star – all three nebulae presented here show evidence of excess UV flux that point towards the existence of a hot companion – see Figs. 4.6 and 4.7 for LoTr 1, Miszalski et al. 2012 for A70, and Siegel et al. 2012 for WeBo 1.

- Nebular morphology – each PN possesses what we would classify as a 'typical'

[ii] Bond, Pollacco & Webbink (2003) assume an expansion velocity of 20 km s^{-1} to derive a similar age of 12 000 ± 6000 yrs.

PN shape, with rings (A70 and WeBo 1) and shells (LoTr 1). A mimic is often more diffuse.

- Systemic velocity – the V_{sys} of the central star is consistent with the V_{sys} of the nebula for both LoTr 1 and A70 (see Sec. 4.2.1 and Miszalski et al. 2012), and so we can say that the observed emission comes from a true PN. No V_{sys} for the central star of WeBo 1 has been published.

- Nebula expansion – all three nebulae have been shown to have an expansion velocity typical for a PN (see Tab. 4.1).

- Nebular diameter – using the values stated in this paper, the physical diameters of LoTr 1, A70 and WeBo 1 are all of the order of $\sim$1 pc (see Tab. 4.1): a sensible value for a PN.

- Galactic latitude – two of the three nebulae are found at high galactic latitudes of $-22°$ and $-25°$ for LoTr 1 and A70, respectively (WeBo 1 is at $+1°$). PNe are more likely to be found away from the Galactic plane than isolated Strömgren spheres.

Table 4.1: Physical parameters of LoTr 1, A 70 and WeBo 1

Nebula	$V_{\rm exp}$ **(km s^{-1})**	**Kinematical age (yr)**	**Physical size (pc)**	**Morphology**
LoTr 1 (inner)	17 ± 4	17 000 ± 5500	0.59 ± 0.05	Spherical/elliptical
LoTr 1 (outer)	25 ± 4	35 000 ± 7000	$1.86^{+0.05}_{-0.09}$	Spherical/elliptical
A70	39 ± 10	13 400 ± 4700	$1.10^{+0.06}_{-0.04}$	Ringed-waist with detected lobes
WeBo 1	23 ± 10	11 700 ± 5900	0.50 ± 0.03	Ringed-waist, no lobes detected

It is apparent that the three objects studied in this paper show the characteristics of bona fide PNe, although, as mentioned earlier, their link with symbiotic stars should also be investigated further.

4.3.2 Conclusions

From the study conducted in this paper, we have been able to show that LoTr 1 possesses a double-shelled, slightly elliptical morphology of age 35 000 ± 7000 yrs for the outer shell and 17 000 ± 5500 yrs for the inner. We have been able to infer the presence of a K1 III-type giant ($T_{\rm eff}$ ~ 4500 K) and hot WD ($T_{\rm eff}$ ~ 123 kK, R = 0.017 $R_{\odot}$) binary system at its core. The cool star has been shown to be kinematically associated with the nebula and to have a rotation period of 6.4 d. Although it was not possible to accurately determine the [Ba/Fe] value for the central star system, we were able to say with confidence that LoTr 1 does *not* show any evidence for an overabundance of Ba. LoTr 1 also presents double peaked emission lines, which have been seen in the other PNe with cool central stars.

Unlike LoTr 1, the PNe A70 and WeBo 1 have both been previously confirmed to contain a Ba-enriched central star system at their core. The two nebulae are also shown here to display morphologies distinct to that of LoTr 1, with both possessing ring-like waists and possible extended lobes. The similar morphologies and chemical enrichment strongly imply that the two have undergone very similar evolutionary or mass-loss processes, and so it is possible that the wind accretion process involved in the formation of Ba stars is also responsible for the formation of these ring-like morphologies. Although the CSPN of LoTr 1 does share some common traits with those of A70 and WeBo 1 – namely binarity with a hot and cool components, and rapid rotation of the secondary – both the lack of a significant overabundance of Ba and the marked difference in nebular morphology would imply a difference in the evolution of this system. The lack of Ba enhancement could be explained by a difference in progenitor mass, metallicity, or simply quantity of mass transferred via the same wind-

accretion process (the amount of material accreted is strongly dependent on orbital separation; Boffin & Jorissen 1988). However, as shown by Boffin & Zacs (1994) only a small amount of matter is needed to be accreted to make a star appear as a Ba star and some mass must have been transferred as it is required in order to spin up the secondary to its rapid rotator state. The most obvious explanation, therefore, is that the mass was transferred at an earlier stage in the evolution of the primary, i.e. before the thermally pulsing AGB phase, when the s-process elements are created and brought to the surface. This would allow us to infer that the AGB evolution of the primary was cut short by this mass-transfer episode, signs of which should be detectable in the properties of the WD. Follow-up observations of the system in order to confirm this hypothesis would be the logical next step to continue the investigation, and it is particularly crucial to determine the orbital period of these systems. However, given the inclination of the nebula of LoTr 1 (very close to pole-on), any radial velocity variations of the central star system would be very difficult to detect, particularly for the expected period of ~1–3 yrs.

With regards to the nebular morphology, multiple shells are not uncommon in PNe, with 25–60% found to show outer structures (Chu, Jacoby & Arendt 1987). However, it is important to distinguish here between 'halo-like' shells (Corradi et al. 2003, 2004), which are extended, generally spherical, structures attached to the inner shell, and detached outer shells, with the latter being far less common. This is critical as the halos are generally understood to be the ionized remnant of mass lost on the AGB which is now being swept up to form the inner shell, while the formation mechanism for multiple, detached shells is still a mystery. Schönberner et al. (1997) show that this may be possible via a combination of photo-ionization and wind interaction, or, alternatively, a binary evolution might be responsible for rapid changes in mass-loss that could form two distinct shells, such as with Abell 65 (Huckvale et al. 2013).

LoTr 1 clearly shows a detached outer shell which may have been produced by rapid changes in mass-loss/transfer during the PN formation phase. The difference in kinematical ages between the two shells of roughly 18 000–20 000 yrs is much shorter

than the single star evolutionary timescales on which these changes might occur.

The results presented here show that we still have some way to go to fully constrain mass-transfer mechanisms in intermediate period binary and post-AGB systems. As such, further study of other similar systems would be highly beneficial, in particular with regards to Ba pollution.

Notes

[1]The acquisition of both the imagery presented in Fig. 4.1 and the nebular spectroscopy from NTT-EMMI of LoTr 1 was acquired by M. Lloyd under ESO programme ID 074.D-0373(A). The nebular and stellar spectroscopy of LoTr 1 from AAT-UCLES was acquired on 2005 January 13–14 by A. López, H. Riesgo and D. Mitchell, and on 2013 January 03 by D. Jones and S. Martell. The SuperWASP-N / WASP-S photometry of LoTr 1 was carried out by D. Pollacco and F. Faedi, who are also responsible for writing the relevant paragraph that is included in this thesis for completeness. The VLT-FORS2 stellar spectroscopy of LoTr 1 was aquired by H.M.J. Boffin under ESO programme ID 088.D-0514(A). The NTT-EFOSC2 stellar spectroscopy of LoTr 1 were acquired by H.M.J. Boffin, D. Jones and the author under ESO programme ID 088.D-0573(A).

The acquisition of the imagery of Abell 70 presented in Fig. 4.12 was done by H. Boffin under ESO programme ID 0.89.D-0453(A). The nebular spectroscopy of Abell 70 from VLT-UVES was acquired by D. Jones under ESO programme ID 087.D-0174(A). The nebular spectroscopy of Abell 70 from SPM-MES was acquired by M. Lloyd, D. Jones, and S. Akras. The main data analysis of Abell 70 was carried out by D. Jones.

The imagery of WeBo 1 presented in Fig. 4.15 was acquired through the IPHAS survey using the Isaac Newton Telescope (INT). The nebular spectroscopy of WeBo 1 was acquired by P. Boumis using SPM-MES.

5

Photometry of the binary central star of PN G033.8+01.5

The work presented in this chapter is in preparation for publication. [1]

5.1 Introduction

PN G033.8+01.5 (α = 18^h 47^m 48.52^s, δ = +01° 32′ 46.08″) was originally detected through the Macquarie/AAO/Strasbourg Hα (MASH) planetary nebula survey (Parker et al. 2006; Miszalski et al. 2008b). The latest version of the MASH catalogue contains over 1200 true, likely and possible new Galactic PN found after re-examining the AAO/UKST SuperCosmos Hα Survey (SHS) of the southern Galactic Plane. The newly formed Paranal Observatory Project to Image Planetary Nebulae (POPIPlaN; Boffin et al. 2012a) aims to become its descendant by updating the MASH catalogue using the high resolution available from an 8m-class telescope. As such, when complete the POPIPlaN database will consist of deep, narrowband images using FORS2 on the VLT of each of the previously discovered MASH PNe. PN G033.8+01.5 is the first of the POPIPlaN PNe to undergo the analyses presented in this chapter.

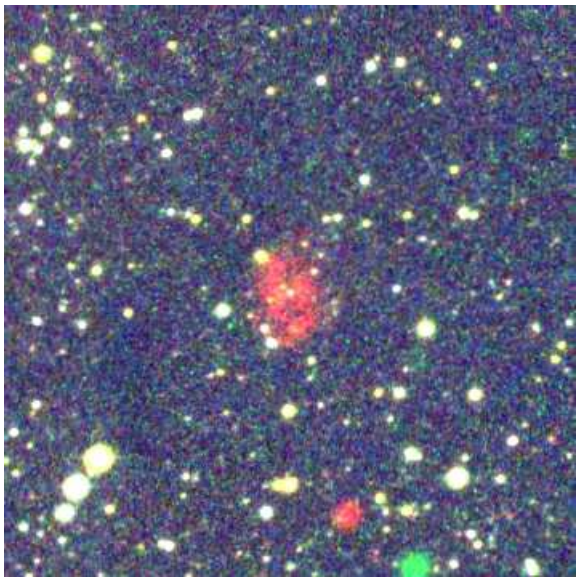

Figure 5.1: Original colour-composite image of PN G033.8+01.5 from the MASH catalogue. North is to the top of the image, east is to the left.

Previously, only three images had been acquired of PN G033.8+01.5; a colour-composite acquired using the 1.9 m Radcliffe telescope based at SAAO on 2000 June 24 (Fig. 5.1), and the other two acquired from the AAO/UKST Hα survey and reproduced in the MASH catalogue (a 3 hr Hα exposure shown in Fig. 5.2a, and a 15 min Short-Red (SR) exposure shown in Fig. 5.2b; Parker et al. 2005). Only two 600 s stellar spectra in the 6000–7000Å wavelength range has been published as part of the online version of the MASH catalogue, along with a J-K colour of 2.5 (with an upper limit of 13.5 for the K-band observation from the 2MASS all-sky survey; Skrutskie et al. 2006). Only described as a 'likely PN', it was shown to possess Hα, [N], and weak [O] emission, but no Hβ.

5.2 Observations and Analysis

5.2.1 Imaging

The Hα+[N] and [O] images shown in Fig. 5.3(a) and (b) were acquired on 2012 June 27 using VLT-FORS2. FORS2 was used in its imaging mode with the mosaic of

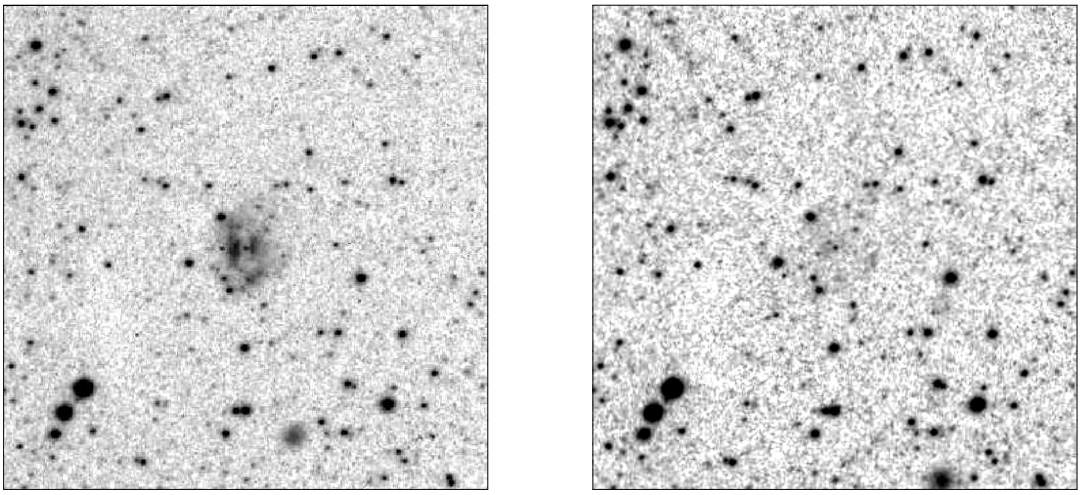

(a) (b)

Figure 5.2: Original (a) Hα and (b) red images of PN G033.8+01.5, from the SHS survey. North is to the top of the image, east is to the left.

two MIT/LL CCDs, 2048×4096 15μm pixels. The exposure time, $t_{\rm exp}$, in each filter was 200 s and the binning set to 2×2 ($\equiv$ 0.25 arcsec pixel^{-1}). The seeing was ∼1.5 arcsec.

The images show PN G033.8+01.5 to have strong Hα emission with an angular size of 51 × 37 arcsec ± 4 arcsec. The Hα emission is strongest in concentrated regions centered at $\alpha = 18^h\ 48^m\ 00.3^s$, $\delta = +01°\ 31'\ 56.0''$ on the western side of the central star, and in two parts centered at $\alpha = 18^h\ 48^m\ 00.9^s$, $\delta = +01°\ 31'\ 56.0''$ and $\alpha = 18^h\ 48^m\ 01.0^s$, $\delta = +01°\ 31'\ 52''$ on the eastern side (see Fig. 5.3a). The overall structure of PN G033.8+01.5 is, at first glance, very asymmetric with several 'wispy' components emanating from the eastern side of the nebula that extend to both the north and south-westerly directions. Another component is seen emanating from the western side of the nebula in a south-south-easterly direction. The nebula appears very diffuse away from these concentrated regions. However, one can be convinced that there is an overall oval shape to the nebula that has perhaps been disrupted. There is only very faint [O] emission, of angular size 14 × 13 arcsec ± 4 arcsec, visible around the central star. The emission appears strongest in two bands of ∼ 12 arcsec in length to the east

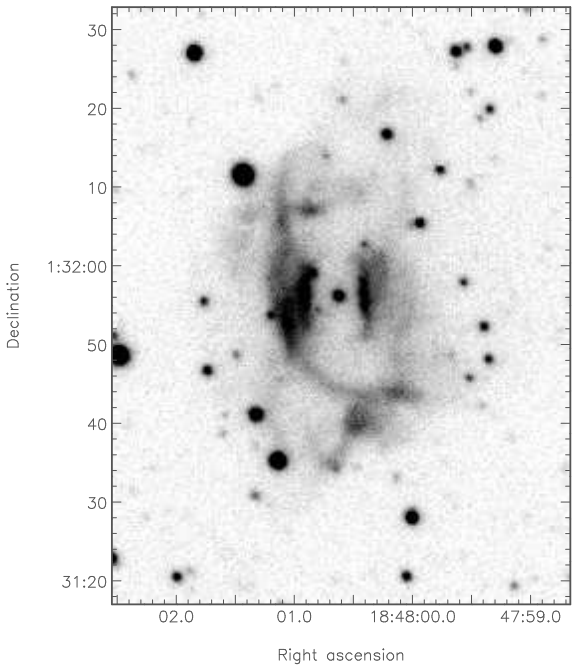

(a)

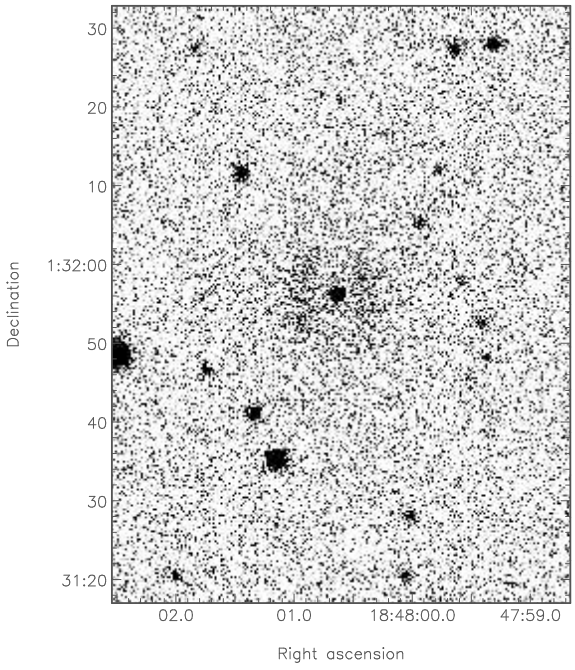

(b)

Figure 5.3: VLT-FORS2 image of PN G033.8+01.5 in (a) Hα+[N], and (b) [O]. North is to the top of the image, east is left. The central star is visible at α = 18:47:48.52, δ = 01:32:46.08. $t_{\rm exp}$ = 200 s for both images.

and west of the central star (see Fig. 5.3b).

PN G033.8+01.5 has perhaps the closest morphological resemblance to another PN known to contain a central binary system: Hen 2-11 (α = 08:37:07.98, δ = -39:25:05.4), shown here in Fig. 5.4. As with PN G033.8+01.5, Hen 2-11 possesses a dense (brighter) core with more diffuse emission emanating to the north-west and south-east directions that traces a possible bi lobed morphology. Jones et al. (2014; in press) classifies this more diffuse emission as low-ionisation filamentary structures and shows that, similarly to PN G033.8+01.5, there is little emission in [O] away from the central region but shows evidence of potential bipolar extensions in the [S] and Hα+N] imagery.

PN G033.8+01.5 also displays morphological similarities to two other members of the MASH catalogue. The first, PN G001.4+06.3 (α = 17:24:53.8, δ = -24:19:21.0), is an object of similar size at 59 $\times$ 41 arcsec (see Fig. 5.5). Described as a 'faint, striated, highly oval PN' in the MASH catalogue, it was first discovered and categorised as a possible (very reddened) globular cluster by Bica (1994) and subsequently as a SN remnant by Bica et al. (1995). However, its weak [S] and strong [N] emission allow for its current status as a 'likely' PN. Morphologically, PN G001.4+06.3 similarly displays a more dense region around the central star followed by more diffuse emission to the north and south. There is a similar 'wispy' component of emission emanating from the central region and sweeping downwards in an 'L' shape in a south-westerly direction.

The second object, PN G315.9+00.3 (α = 14:37:53.2, δ = -59:49:25.0), is perhaps morphologically less convincing. It is noted as a 'true' PN with a bipolar morphology in the MASH catalogue, of size 103 $\times$ 63 arcsec (see Fig. 5.6). Also determined to be a radio source (Bojičić et al. 2011), it is noted as possessing the Hα, [N] and [O] emission typical of a PN. On first glance of the imagery presented in Fig. 5.6, the nebula emission is similarly enhanced on the western side with an apparent curve towards the east.

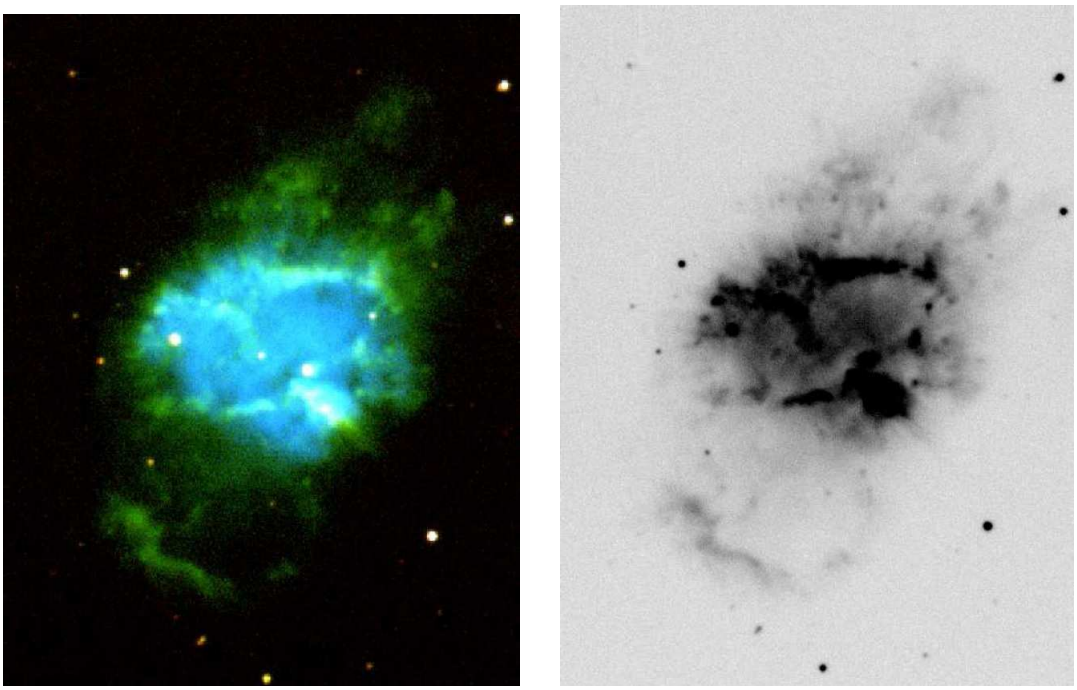

(a) (b)

Figure 5.4: i
mages of Hen 2-11]NTT-EFOSC2 images of Hen 2-11. (a) Colour composite in [S] λ6716+6731Å (red), Hα+[N]λ6584 Å (green) and [O]λ5007 Å (blue), and (b) Hα+[N]λ6584 Å. Images taken from Jones et al. (2014).

5.2.2 Stellar photometry

In the period 2013 June 06–13, the central star of PN G033.8+01.5 was photometrically monitored using NTT-EFOSC2. The data were taken using the Gunn-*i* filter and CCD #40 (2048 × 2048, 15μm pixels), employing 2×2 binning (≡ 0.24 arcsec pixel^{-1}). 94 frames were acquired for the photometry of varying $t_{\rm exp}$: 90 × 90 s, 1 × 30 s, 2 × 120 s, and 1 × 180 s. The seeing varied between 0.47–1.06 arcsec. By taking several observations of the object over different nights, it allowed the potential variability to be investigated as well as accounting for variations in photometric conditions.

The general method of differential photometry used to investigate the central star of PN G033.8+01.5 is described in Ch. 2.2. The photometry of PN G033.8+01.5 was

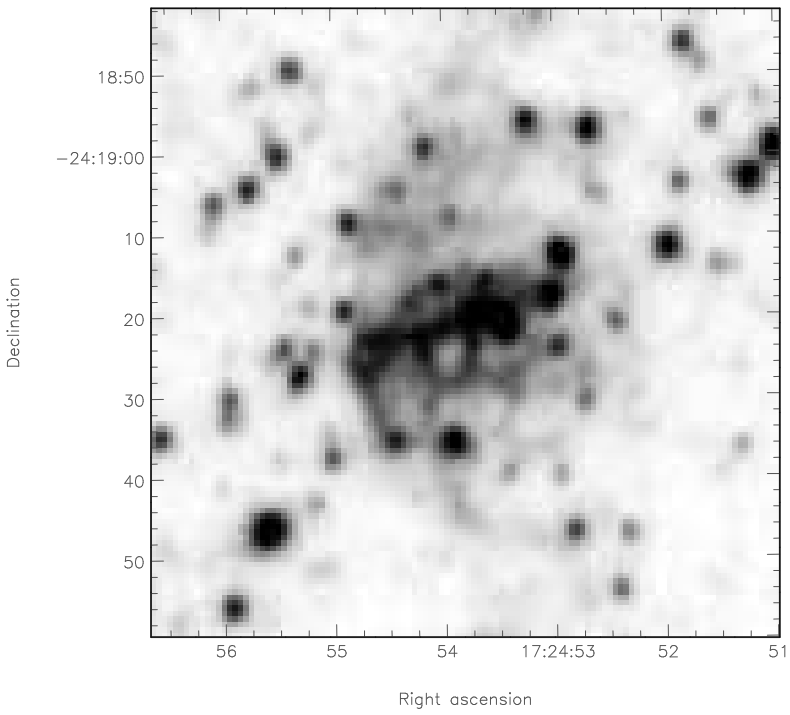

Figure 5.5: Hα image of PN G001.4+06.3 from the SHS survey.

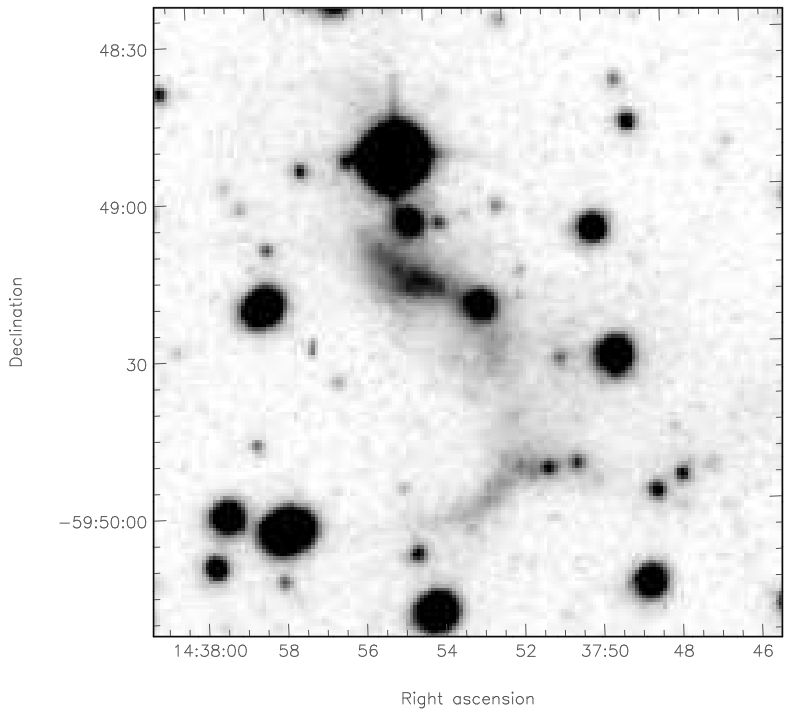

Figure 5.6: Hα image of PN G315.9+00.3 from the SHS survey.

carried out using the DAOPHOT package within IRAF. Due to both the wide variation in seeing between frames and the predicted variability of the target, the stellar aperture, and therefore the sky annulus, could not be taken to be a constant radius, but instead were varied to compliment the FWHM of the star in each individual frame using a code ( ) written by O.A. Gonzalez (private communication). The FWHM of the central star varied between 3–12 pixels across all frames. All 94 *i*-band frames were initially aligned so as not to affect the photometry. The FWHM for the target star and a selection of comparison stars in the same image was measured for all frames using . By compiling a list of 8 different aperture radii (in terms of multiples of the FWHM) and inputting the corresponding sky annulus radii (taken to be 4 × aperture radius for the inner annulus, and 6 × aperture radius for the outer annulus), performs the photometry using each radius at a time, and outputs a list of the raw instrumental magnitudes extracted by the photometry for the target and selection of comparison stars for the desired aperture. By running in this way for each of the eight aperture radii, it is possible to narrow down the optimum aperture size to use for the creation of the lightcurve and subsequent analysis. An aperture radius of 1 × FWHM was eventually decided upon based on a curve of growth of the extracted instrumental magnitude against several smaller and larger radii. It was determined that the selected comparison stars had no intrinsic variability, and so were suitable for use in the differential photometry.

In order to be able to estimate both the colour of the target and its distance, data were also acquired in Bessel *B*, *V* and *R* filters during the same period, as well as Hα and Hβ continuum. The Bessel *B*, Hα and Hβ continuum data were taken under 0.47 arcsec seeing with $t_{\rm exp}$ = 30 s, 60 s and 120 s respectively. The Bessel *V* and *R* data were acquired under 1.06 arcsec seeing and with $t_{\rm exp}$ = 120 s. Appropriate photometric standards were taken in the same filters (Gunn-*i*, Bessel *B* × 6, *V* × 4, *R* × 4, Hα × 7 and Hβ continuum × 6) under 1.06 arcsec seeing and with exposure times between 10–30 s. The extracted instrumental magnitudes and associated zero points are presented in Tab. 5.2.

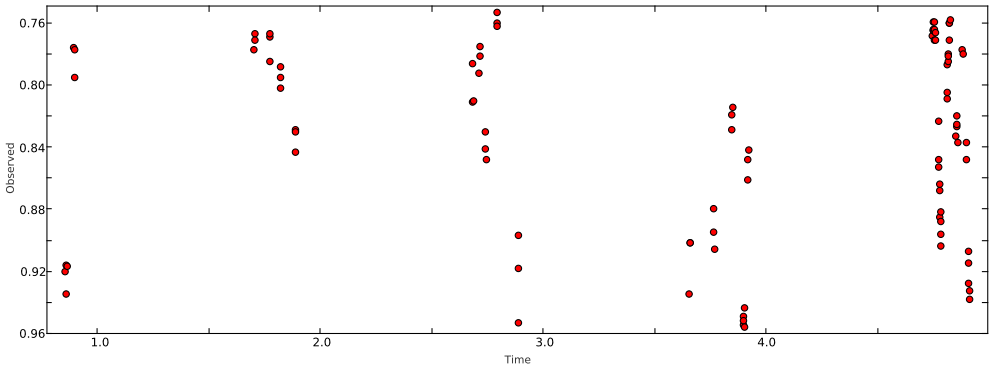

Figure 5.7: Initial plot of time (in days) vs. differential magnitude of PN G033.8+01.5 generated by P 04, showing the first evidence of variability of the central star.

5.2.3 Lightcurve analysis

A period for the variability of the central star of PN G033.8+01.5 was estimated using P 04 (see Ch. 2.2 for details on its operation). Based on the number of input data points and their separation in time, a Nyquist frequency of 338.83 cycles per day was determined. The initial plot from P 04 showing the first evidence of the variable nature of the central star is presented here in Fig.5.7. By performing Fourier analysis on the data and extracting the common frequencies, estimated periods of 1.52, 2.01 and 3.93 hrs were obtained (there were difficulties in distinguishing what were actually common frequencies - see Fig. 5.8 below - and so these periods were taken only as estimates). Due to the physical unfeasibility of the smaller periods, the data were phase-folded using Eq. [2.12] over a range of periods between 2–4 hrs to determine the best fit. This turned out to be a period of 3.04 hrs (0.1268 d), and the associated phase-folded lightcurve is shown in Fig. 5.9.

Once a period was determined, the next step was to create a best fit model to the lightcurve in order to derive the most likely stellar parameters using the modelling program (see Ch. 2.2 for more details). Contrary to usual notation, within the program the primary star refers to that which is *eclipsing* first - in this case the MS star, and so the WD is referred to as the secondary star throughout the

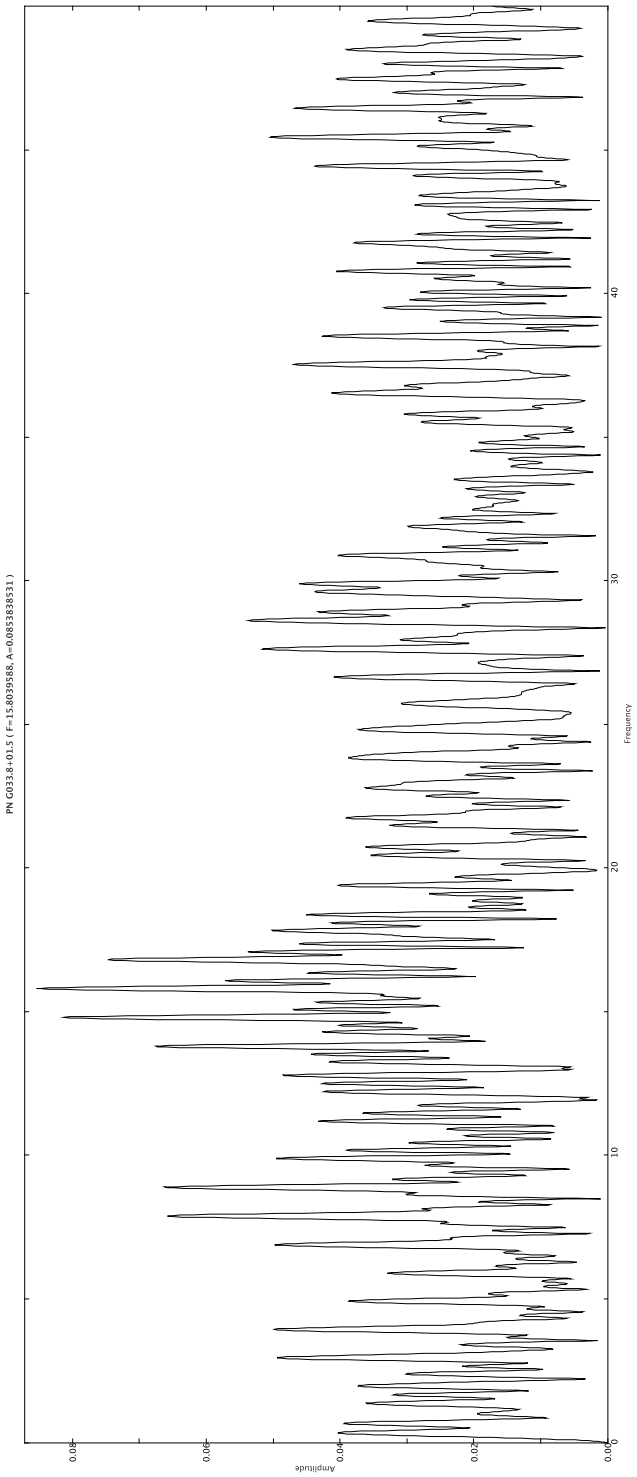

Figure 5.8: Fourier analysis plot for extracted photometry of PN G033.8+01.5, generated by P 04.

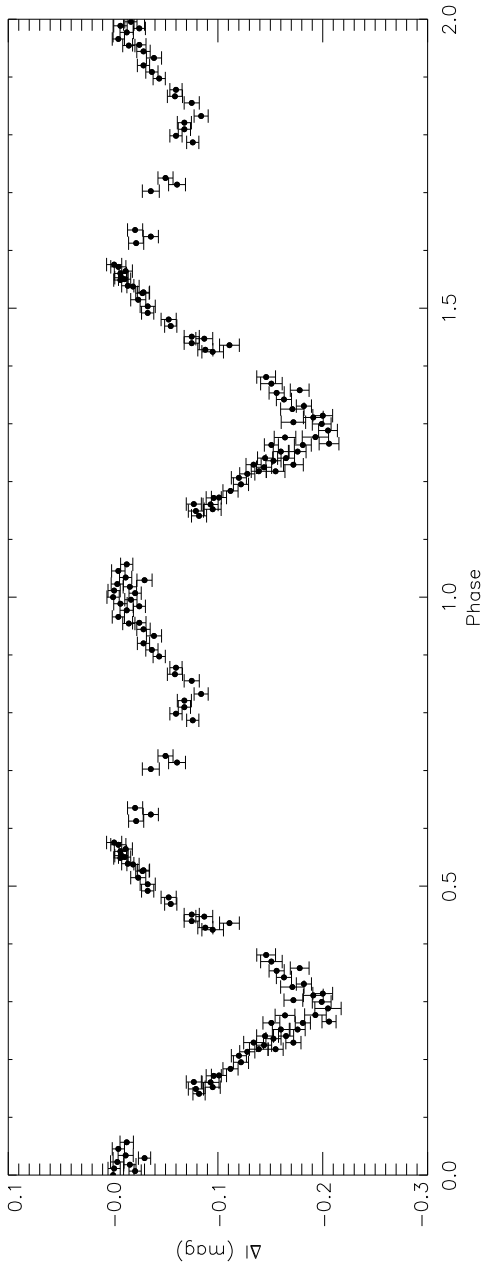

Figure 5.9: Plot showing the phase-folded lightcurve of PN G033.8+01.5. The lightcurve consists of 94 *i*-band data points. The data are phase-folded over a period of 0.1268 d (~ 3 hrs) and plotted over two complete orbital cycles for clarity.

rest of this chapter for continuity. It was assumed that there must be a large luminosity difference between the two stars due to the differing appearance of the two eclipses (a deep primary and shallow secondary). The two best-fitting models had the parameters presented in Tab. 5.1. Although model A, represented in Fig. 5.10, has the lower χ^2 of the two, it was difficult to reconcile the results with a physically viable explanation as it would imply that both stars are filling their Roche lobes (i.e. mass transfer is occurring) which would result in an unstable system. As the initial assumption is that PN G033.8+01.5 is a regular PN (i.e. a stable system), it made sense to carry out the initial analyses with model B. Also, the determined inclination for model A would imply that the two stars are not eclipsing but instead the lightcurve is mainly due to elongation effects. Model B, represented in Fig. 5.11, is therefore a more likely solution with a cool main sequence star filling its Roche lobe and a hot WD that is much smaller than its Roche radius. The inclination of the binary in model B would allow for a partial eclipse. The dip in the primary minima of the model as shown in Fig. 5.11 offers an explanation for the spread in points in the same minima in the true lightcurve of PN G033.8+01.5 that model A does not account for.

Table 5.1: Table showing the best-fit stellar parameters for two models replicating the lightcurve of PN G033.8+01.5. q = mass ratio, $i°$ = system inclination, RLFF = Roche lobe fill factor. The subset numbers refer to the primary (1) and secondary (2) star in the system.

Model	**q**	***i*°**	**RLFF**$_1$	**RLFF**$_2$	$T_{\rm eff\,1}$ **(K)**	$T_{\rm eff\,2}$ **(K)**	χ^2
A	0.80	49.0	1.0	1.000	3990	19 000	1.73
B	0.80	67.7	1.0	0.026	3571	38 270	3.32

5.2.4 Colour determination

Using the routine within the IRAF software package, an aperture radius corresponding to 4 × FWHM of the radial profile of the star was chosen, utilising the

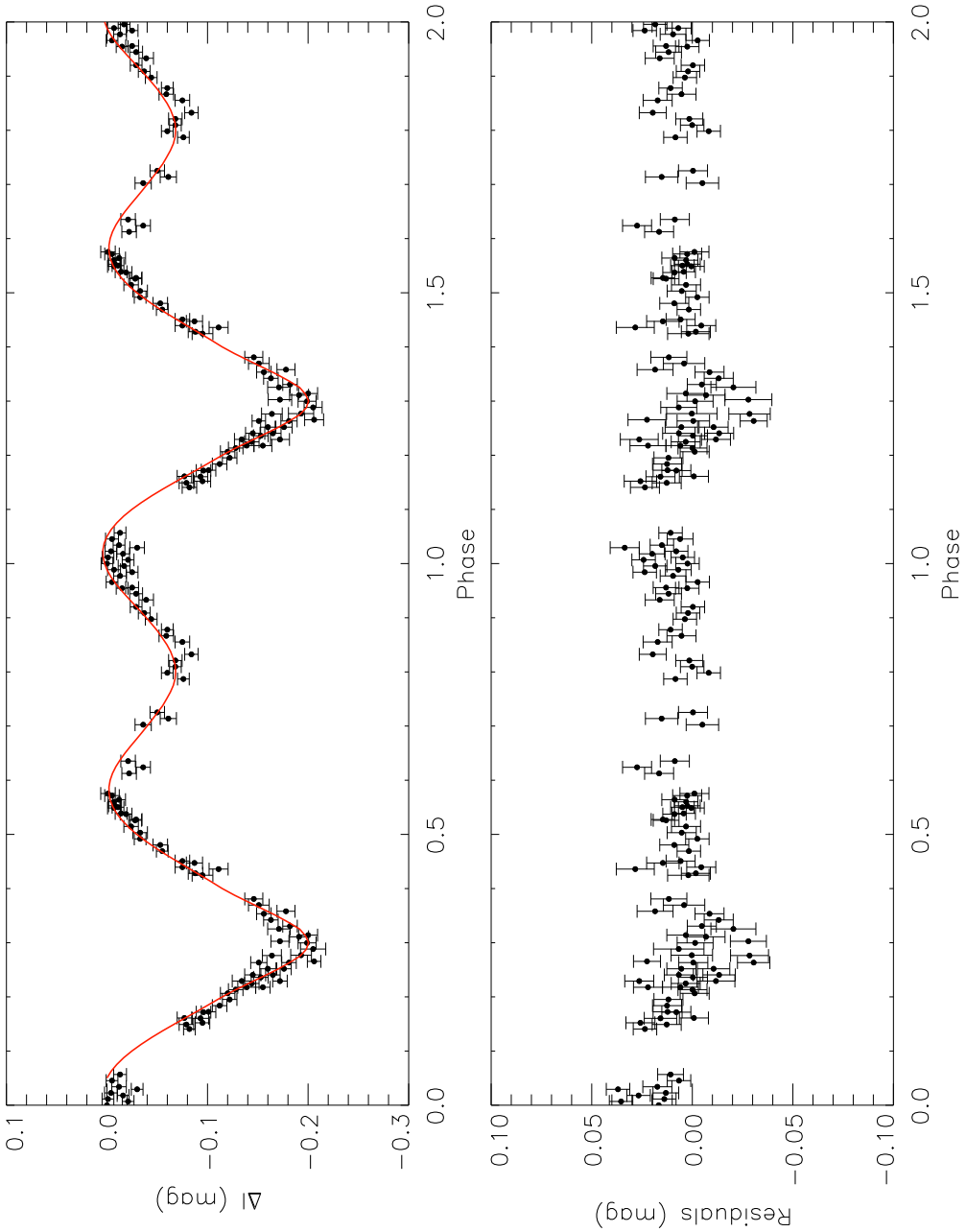

Figure 5.10: N model *A* replicating the lightcurve of PN G033.8+01.5 to determine the stellar parameters.

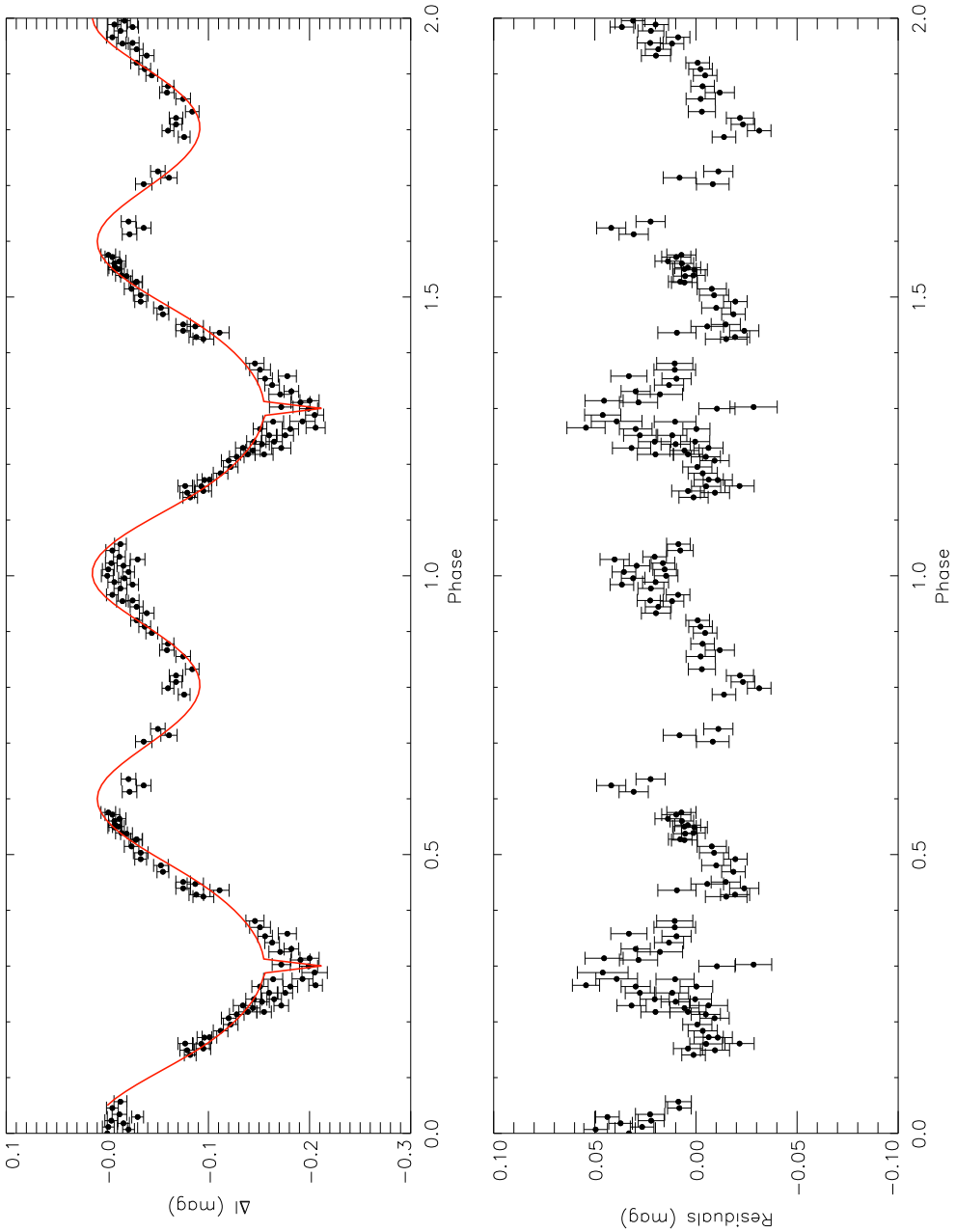

Figure 5.11: N model *B* replicating the lightcurve of PN G033.8+01.5 to determine the stellar parameters.

curve of growth method for selection. Correspondingly, an inner sky annulus radius of 4 × aperture radius and outer sky annulus radius of 6 × aperture radius was used to give the total, sky-subtracted flux of the target and each standard star. By taking the values for the stellar flux (F) from the photometry and $t_{\rm exp}$ for each frame, an instrumental magnitude (m_i) was calculated for the target and all observed standard stars using Eq. [2.11]. This instrumental magnitude was then corrected (again, for both the target and the standard stars) to account for local extinction at the La Silla Observatory and air mass at the time of observation, using Eq. [2.13]

Catalogue magnitudes for each standard star in the fields observed were acquired from a list of EFOSC2 photometric standards from ESO. A zero-point magnitude (ZP, i.e. a correction factor) was determined by taking the difference between the given catalogue magnitude and m_{corr} for each star. Since several images were acquired of each standard field, an average ZP was calculated in each particular filter. This ZP was then applied (by addition) to m_{corr} of the target. Tab. 5.2 shows each value of m_{corr} and the associated ZP for each standard star, and the subsequently derived colour indices are presented in Tab. 5.3.

Once all values of m_{corr} had been determined using Eq. [2.13] for both the target and standards, a colour-correction factor had to be applied. This was determined using the observations of the standard stars and Eq. [2.14].

The colour indices referred to by the 'colour' term used in this analysis are ($B-V$), ($V-R$), and ($B-I$). By using the statistical computing and graphics language R, it was possible to create colour-magnitude diagrams (CMDs) by plotting the calculated colour indices against m_{corr} for each filter used (the residuals of each point were also plotted; see Figs. 5.12 – 5.18). By applying a best-fit to the resultant points, the colour coefficient ϵ and intercept C required for Eq. [2.14] were calculated for each standard field and are shown in Tab. 5.4. The standard errors on each of these terms are generated by the program. The resultant correction factors were then applied to m_{corr} for PN G033.8+01.5 to give the final, corrected instrumental (apparent) magnitude (m_o) of the object, presented in Tab. 5.5. Based on the B, V, R and I colours given in Tab. 5.5, the

binary system is overall more luminous in the red than in the blue.

As can be seen from Tab. 5.2, there is an apparent outlier in the B-band for star #338 in the field of SA 104-334 (16.363 / 0.287). As such, this star was removed from the analyses for all three bands so as not to affect the colour indices or the fit for the CMDs.

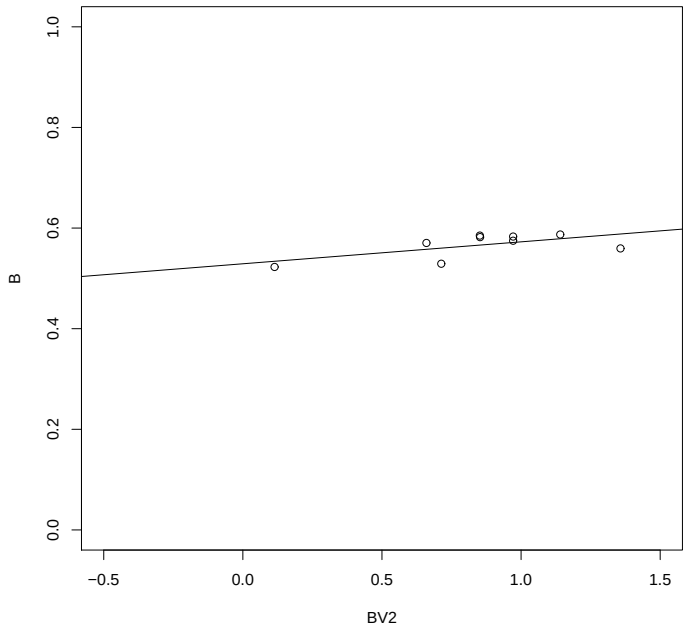

(a)

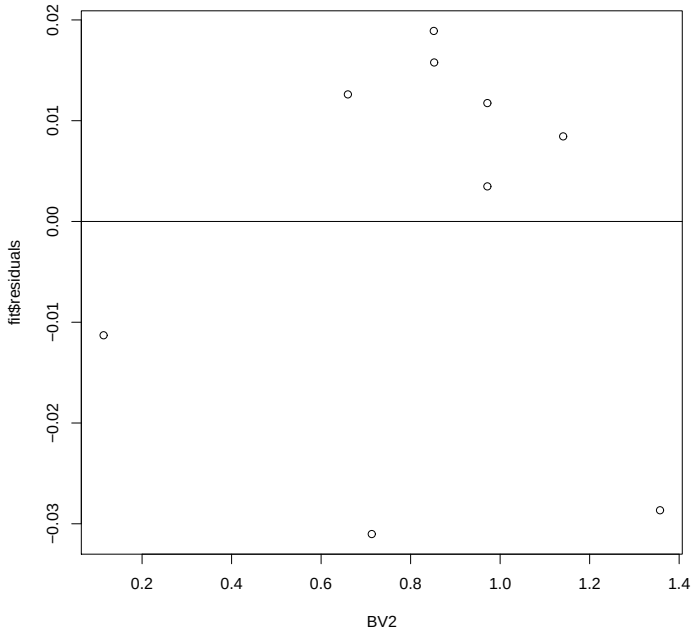

(b)

Figure 5.12: (a) B vs. ($B - V$) colour-magnitude diagram, and (b) the corresponding residuals.

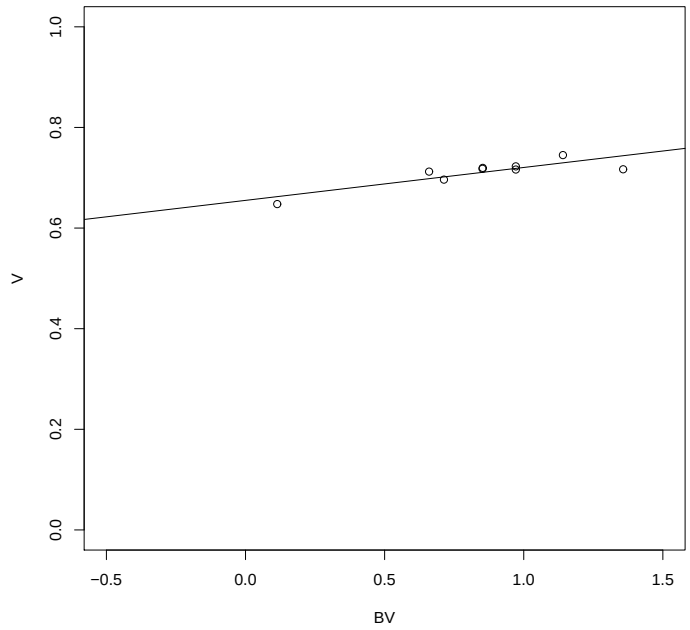

(a)

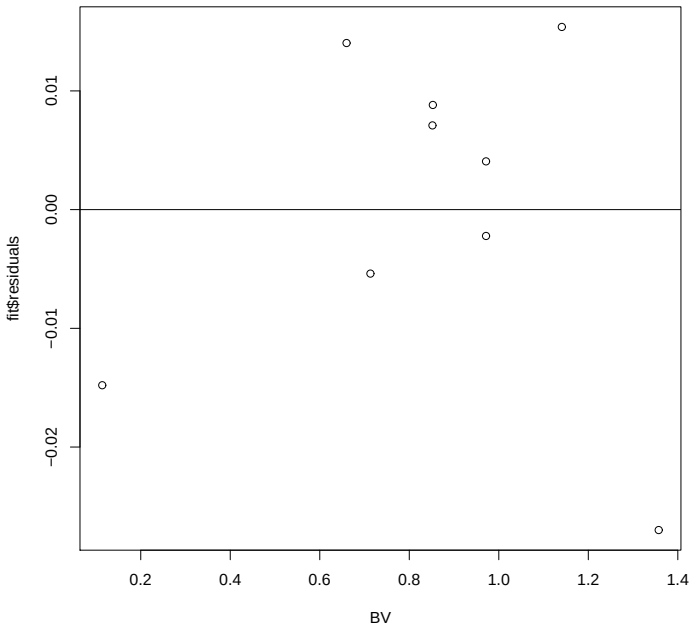

(b)

Figure 5.13: (a) V vs. $(B - V)$ colour-magnitude diagram, and (b) the corresponding residuals.

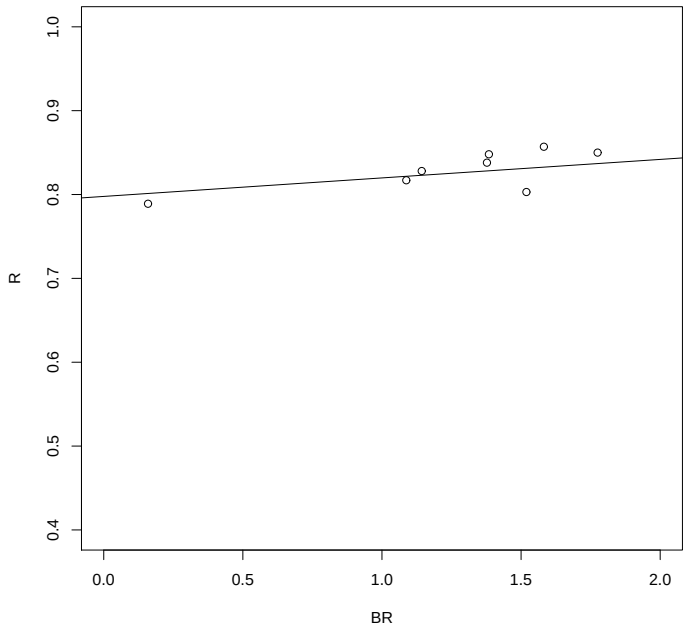

(a)

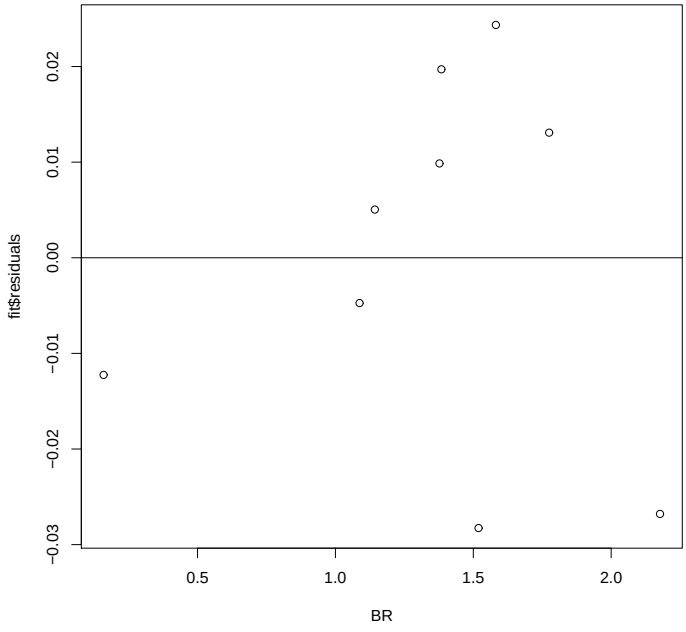

(b)

Figure 5.14: (a) R vs. (B – R) colour-magnitude diagram, and (b) the corresponding residuals.

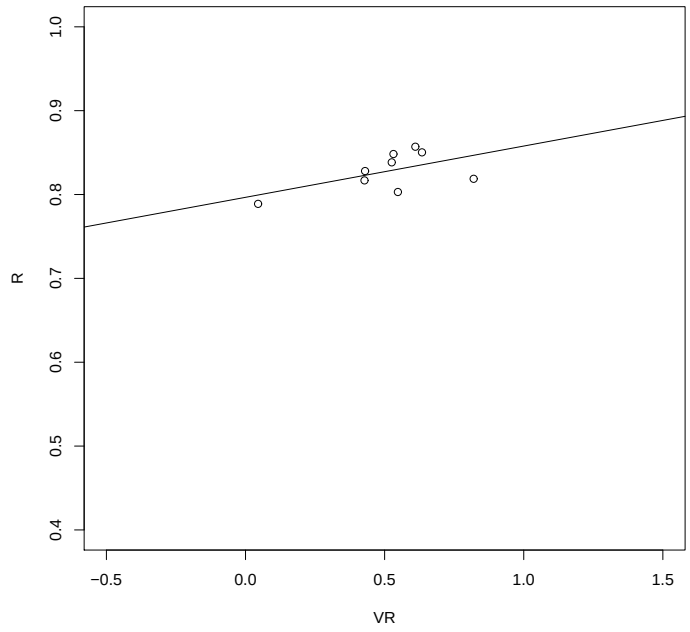

(a)

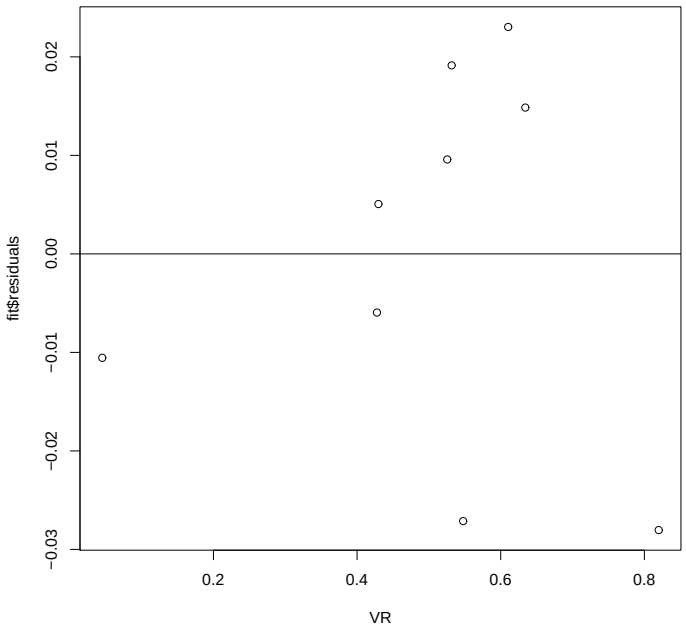

(b)

Figure 5.15: (a) R vs. $(V - R)$ colour-magnitude diagram, and (b) the corresponding residuals.

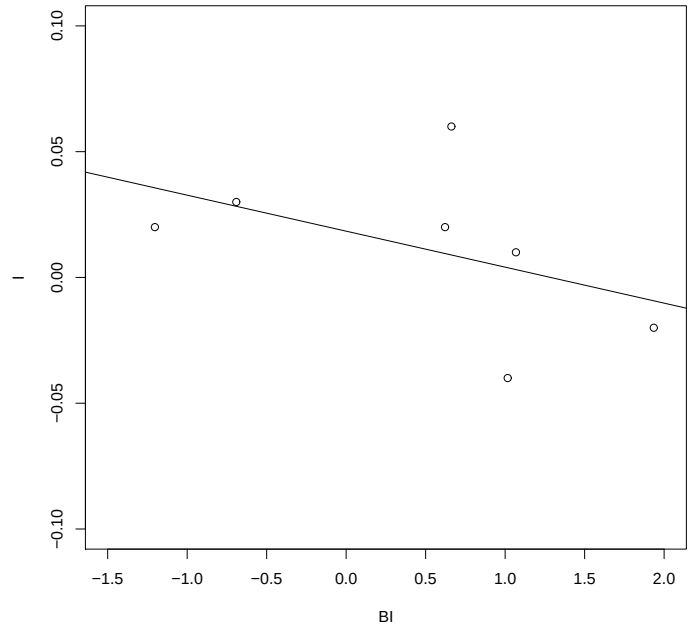

(a)

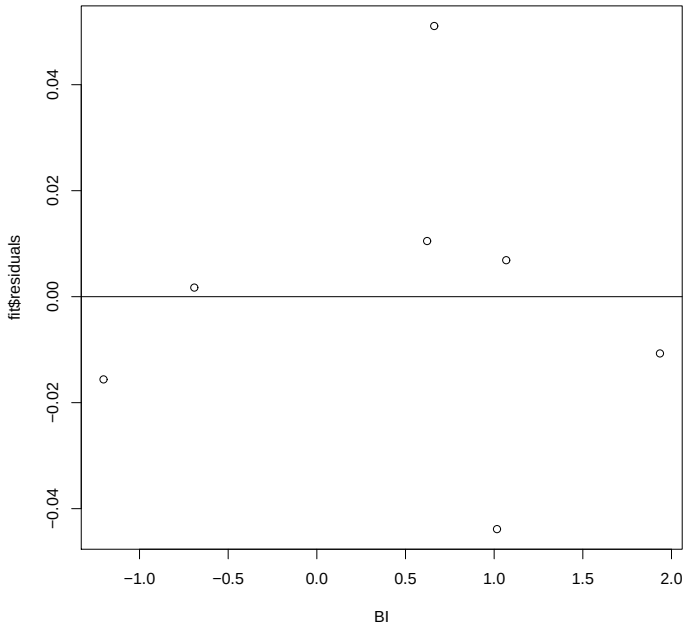

(b)

Figure 5.16: (a) I vs. ($B - I$) colour-magnitude diagram, and (b) the corresponding residuals.

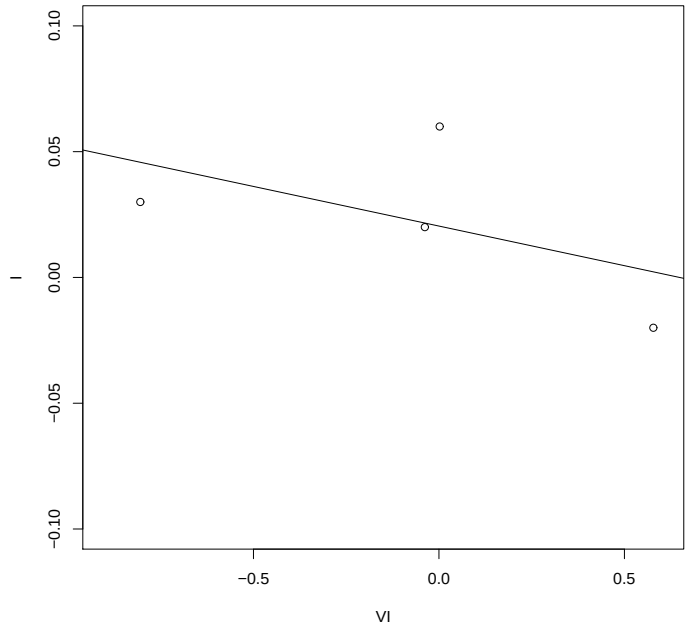

(a)

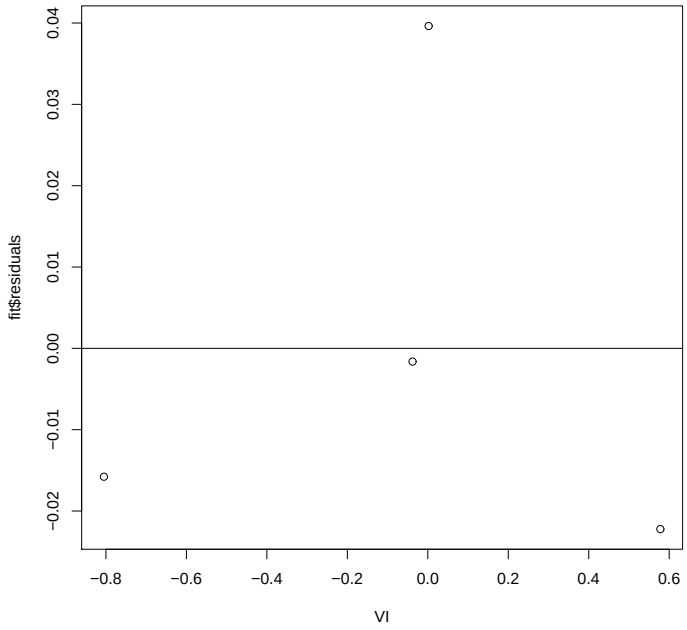

(b)

Figure 5.17: (a) I vs. $(V - I)$ colour-magnitude diagram, and (b) the corresponding residuals.

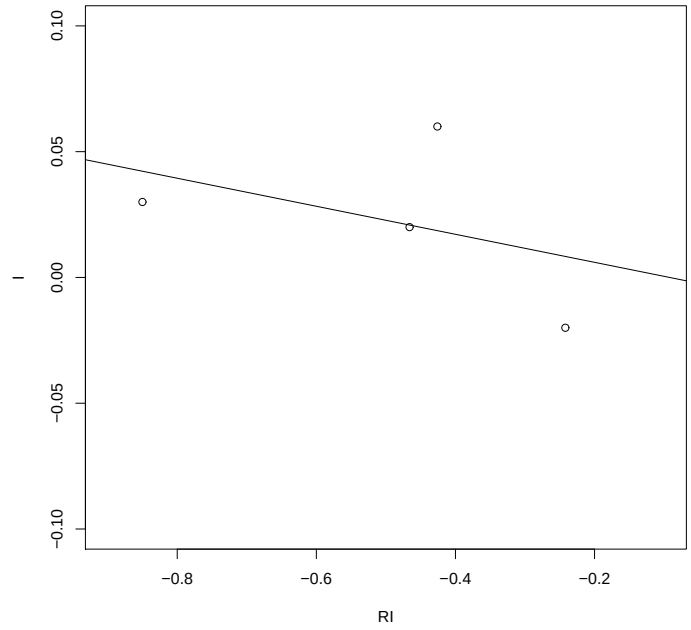

(a)

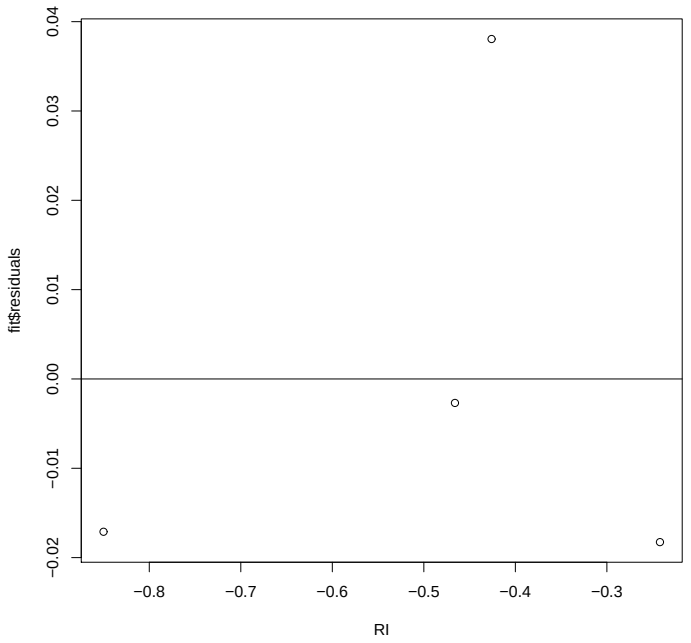

(b)

Figure 5.18: (a) I vs. ($R - I$) colour-magnitude diagram, and (b) the corresponding residuals.

Standard field	**Star #**	m_B **/ ZP**	m_V **/ ZP**	m_R **/ ZP**	m_I **/ ZP**
SA 101-408	413	12.979 ± 0.002 / 0.587	11.838 ± 0.002 / 0.745	11.204 ± 0.002 / 0.850	-
	408	15.425 ± 0.002 / 0.560	14.068 ± 0.002 / 0.717	13.248 ± 0.002 / 0.819	13.49 ± 0.005 / -0.02
	410	13.663 ± 0.002 / 0.529	12.950 ± 0.002 / 0.696	12.520 ± 0.002 / 0.828	-
SA 104-334	338	16.363 ± 0.005 / 0.287	15.367 ± 0.003 / 0.691	14.903 ± 0.004 / 0.808	-
	336	14.659 ± 0.005 / 0.575	13.688 ± 0.003 / 0.716	13.140 ± 0.004 / 0.803	-
	334	13.431 ± 0.005 / 0.570	12.771 ± 0.003 / 0.712	12.344 ± 0.004 / 0.817	12.79 ± 0.005 / 0.04
	339	15.707 ± 0.005 / 0.583	14.736 ± 0.003 / 0.723	14.126 ± 0.004 /0.857	-
G93-48	48	12.209 ± 0.002 / 0.523	12.095 ± 0.003 / 0.648	12.050 ± 0.004 / 0.789	12.90 ± 0.005/ 0.03
	A	12.550 ± 0.002 / 0.585	11.698± 0.003 / 0.718	11.173 ± 0.004 / 0.838	-
	B	12.939 ± 0.002 / 0.582	12.136 ± 0.003 / 0.720	11.605 ± 0.004 / 0.848	-
NGC 7293	-	12.667 ± 0.002 / 0.420	-	-	13.87 ± 0.004 / 0.020

Table 5.2: Table showing corrected instrumental magnitudes and their associated error and zero-point in *B*, *V*, *R*, and *I* for a range of standard stars. Star #338 of standard field SA 104-334 was not included in the analyses for any of the bands.

Standard field	**Star #**	$(B-V)$	$(V-R)$	$(B-I)$	$(V-I)$	$(R-I)$
SA 101-408	413	1.141 ± 0.002	0.634 ± 0.002	-	-	-
	408	1.357 ± 0.002	0.820 ± 0.002	1.935 ± 0.005	0.578 ± 0.005	-0.242 ± 0.005
	410	0.713 ± 0.002	0.430 ± 0.002	-	-	-
SA 104-334	338	0.304 ± 0.007	0.464 ± 0.005	-	-	-
	336	0.971 ± 0.007	0.548 ± 0.005	-	-	-
	334	0.660 ± 0.007	0.428 ± 0.005	0.662 ± ± 0.005	-0.018	-0.446 ± 0.005
	339	0.972 ± 0.007	0.610 ± 0.005	-	-	-
G93-48	48	0.114 ± 0.004	0.045 ± 0.005	-0.691 ± 0.005	-0.805 ± 0.006	-0.850 ± 0.006
	A	0.852 ± 0.004	0.526 ± 0.005	-	-	-
	B	0.853 ± 0.004	0.532 ± 0.005	-	-	-
NGC 7293	-	-	-	-1.204 ± 0.002	-	-

Table 5.3: Table showing derived colour indices and associated error.

Table 5.4: Table showing the extrapolated colour coefficients and associated error. C = intercept, ϵ = colour coefficient.

Bessel filter	C	ϵ
B	0.529 ± 0.019	0.044 ± 0.021
V	0.655 ± 0.014	0.065 ± 0.015
R	0.797 ± 0.019	0.061 ± 0.034
I	0.018 ± 0.013	-0.014 ± 0.012

Table 5.5: Table showing colour-corrected instrumental magnitude, m_o, for the central star of PN G033.8+01.5

Bessel filter	m_o
B	21.52 ± 0.06
V	19.18 ± 0.09
R	17.23 ± 0.05
I	17.87 ± 0.04

5.2.5 Determination of stellar and nebular parameters

Stellar masses, radii and luminosities

Eq. [1.3] can be reduced to:

$$M = \frac{a^3}{P^2} \tag{5.1}$$

where P is in yrs, a is in AU, and M is in units of $M_\odot$. By using the determined total mass of the binary system of 0.4 $M_\odot$ and the previously determined period of 0.1268 d, this gives a value for a of 0.78 $R_\odot$.

Once a has been determined, the RL radius, RL_r, can be calculated using Eq. [1.4] to give a value of 0.46 $R_\odot$. This gives $RL_{r,1} = 0.34\ R_\odot$ and $RL_{r,2} = 0.44\ R_\odot$, when $a = 0.78\ R_\odot$. As determined by the N model and noted in Tab. 5.1, $RLFF_1 = 1$ and $RLFF_2 = 0.026$, meaning $R_1 = 0.34\ R_\odot$ and $R_2 = 0.01\ R_\odot$. The former radius is consistent with an M V -type MS star, also known as a red dwarf (e.g. see Kaltenegger & Traub 2009), whilst the latter falls within the typical range of radii for a WD of 0.008–0.020 $R_\odot$ as stated by Shipman (1979).

The luminosity of each star can subsequently be determined using the luminosity relation for a blackbody:

$$\frac{L_\odot}{L} = \left(\frac{R_\odot}{R}\right)^2 \left(\frac{T_\odot}{T}\right)^4 . \tag{5.2}$$

Given the values for T_{eff} presented in Tab. 5.1 and the previously determined values for R, this allows the derivation of $L_1 = 0.017\ L_\odot$ and $L_2 = 0.188\ L_\odot$.

The mass of the M V star may now be derived using the following equation as given by Joardar, Bhattacharya & Bhattacharya (2008):

$$\frac{L}{L_\odot} = \left(\frac{M}{M_\odot}\right)^{2.3} \tag{5.3}$$

to give a value of 0.17 $M_\odot$. Given the input value $q = 0.8$, the total mass of the binary system of 0.4 $M_\odot$ can be derived as:

$$M_1 + M_2 = 0.17 \times \frac{1}{q+1} \tag{5.4}$$

which in turn would imply a mass for the WD of 0.23 $M_\odot$. Both masses fall within the suitable range of radii values for M V and WD stars.

Using the following equation to calculate the surface gravity of each star:

$$\log\ g = \log\left(\frac{GM}{R^2}\right) \tag{5.5}$$

in CGS units, subsequent values of $\log\ g$ for the primary and secondary stars can be

derived as 4.61 and 7.80 (again, consistent with M V and WD spectral types), respectively.

The derived stellar parameters for both the primary and secondary stars are listed in Tab. 5.6.

Table 5.6: Table showing the derived stellar parameters of the primary and secondary stars of the central binary of PN G033.8+01.5. The binary separation, a, is 0.78 $R_\odot$.

Star	**M (** $M_\odot$**)**	**R (** $R_\odot$**)**	**L (** $L_\odot$**)**	log g
M2V dwarf	0.17	0.34	0.017	4.61
White dwarf	0.23	0.01	0.19	7.80

Distance to the system

To calculate the bolometric magnitude of each star in the system (that is, the magnitude of the object across the entire spectral range), the following equation can be used:

$$M_{bol} = 4.73 - 2.5 \log\left(\frac{L}{L_\odot}\right) \tag{5.6}$$

where 4.73 is the solar bolometric magnitude, $M_{\odot bol}$, as given in Cox (2000)[i]. This gives $M_{1,bol} = 9.15$ for the M V primary, and $M_{2,bol} = 6.53$ for the WD secondary. To obtain the absolute magnitude, M_V, a bolometric correction factor (BC) is required that is mainly dependent on the $T_{\rm eff}$ (and therefore colour) of the object in question ($M_V = M_{bol} - BC$).

Using the equation following given by Reed (1998), a BC value for the M V star

[i]However, there is a lot of discrepancy as to what the standardised value for $M_{\odot bol}$ should be – see Torres (2010).

can be derived:

$$BC = -8.499[\log(T_\odot) - 4)]^4 + 13.42[\log(T_\odot) - 4]^3 - 8.31[\log(T_\odot) - 4]^2 - 3.901[\log(T_\odot) - 4] - 0.438 \quad (5.7)$$

giving a value of BC = -1.90. As a result, a value for $M_{V,1}$ of 11.05 for the M 2V star can be derived.

The apparent magnitude, $m_{V,1}$ of the M V star can be found using the following:

$$\begin{aligned} m_{V,sys} &= -2.5\log(F_{sys}) \\ &= m_{V,1} - 2.5\log(1 + F_2/F_1) \end{aligned} \quad (5.8)$$

where m_V is the apparent visual magnitude, F is the flux, and the subscript 1 and 2 refer to the primary and secondary stars in the system respectively. The value of F_2/F_1 is given by:

$$\frac{F_2}{F_1} = 10^{\,0.4(M_{V,2} - M_{V,1})}. \quad (5.9)$$

Solving Eq. [5.8] for $m_{V,1}$ gives a value for the apparent visual magnitude in the V-band of the primary star of 19.65 mag. Given $M_{V,1}$ = 11.05 for the primary star, an estimate of the distance to PN G033.8+01.5 can be made using the distance modulus equation:

$$m_V - M_V = 5\log d - 5. \quad (5.10)$$

This gives a distance to the system of 525 pc. It should be noted that the Galactic extinction, A_v, has not been accounted for in these calculations. Due to the low declination of the object (+01°), it can be assumed that this value would be fairly large (of order $\sim$ 7 mag).

Given $m_{V,sys}$ and the distance, a value for $M_{V,sys}$ can be calculated as 10.58. To then derive the magnitudes of the WD in the V-band, Eqs. [5.8] – [5.10] can be utilised using the values acquired for $m_{V,sys}$ and $m_{V,1}$ to determine the flux of the WD, which can then be converted back to a magnitude. The resultant magnitudes are $m_{V,2}$ = 20.32

and $M_{V,2}$ = 11.72, at a distance of 525 pc.

It is possible to go back and calculate M and m for each of the stellar components in the other bands using the magnitudes given in Tab. 5.5, the derived distance of 525 pc, mean colour indices from the literature, and Eqs. [5.8] – [5.10]. A typical $(V - I)$ of 2.62 for a M2 V star was taken from Ducati et al. (2001) to calculate M_I and m_I using Eqs. [5.10]. From this, the flux ratio given by Eq. [5.9] can be determined, subsequently allowing the derivation of m_I of the binary system as a whole from Eq. [5.8].

Similarly, an average $(B - V)$ value of 1.503 for an M2 V star was assumed, as given by Erik Mamajek[ii] (2010), in order to calculate M_B and m_B. An average $(V - R)$ value of 1.52 for an M2 V star was also assumed, as given by Wing (1983), to calculate M_r and m_r.

All of the computed values are tabulated in Tab. 5.7.

Table 5.7: Table showing derived and predicted magnitudes of each binary component in the various bands at d = 525 pc.

Magnitude	**B**	**V**	**R**	**I**
M_{sys}	12.92	10.58	8.38	9.05
$M_{M2\,V}$	12.59	11.05	9.53	8.47
M_{WD}	14.04	11.72	9.27	9.43
m_{sys}	21.52	19.18	17.23	17.65
$m_{M2\,V}$	21.19	19.65	18.13	17.03
m_{WD}	22.64	20.32	17.86	18.03

[ii] http://www.pas.rochester.edu/ẽmamajek/memo_M.html

Absolute size and age of the PN

The absolute size of the nebula of PN G033.8+01.5 can be determined using basic trigonometry involving the derived distance and angular size noted from the imagery in Fig. 5.3. At its widest point, the nebula is in the region of 0.13 pc in diameter. Given that the expansion velocity of the nebula is unknown, an average upper limit of 40 km s^{-1} and a lower limit of 20 km s^{-1} were assumed to give an estimate of an age for the nebula of 3180–6359 yrs at a distance of 525 pc. This is comparable to 12 580 yrs for HaTr 4 at a distance of 3 kpc (see Ch. 3.3), 13 400 ± 4700 yrs for A70 (see Ch. 4.2.2), and 11 700 ± 5900 yrs for WeBo 1 (see Ch. 4.2.3).

5.3 Discussion

It is safe to say that the model used in the analysis presented in this chapter does not seem to fit into the classical scheme of PN kinematics, as the derived results contain inconsistencies. The most obvious problem is that the M V star appears more luminous than the system as whole in the *B* and *I* bands, as shown in Tab. 5.7, and the WD appears much less luminous in the *B* band both compared to the M V star and compared to the the other three bands. One possible explanation is that the typical $(V - I)$ and $(B - I)$ indices taken from the literature are inaccurate (or at least possess a fairly large range of potential values) which would in turn have an effect on the other derived magnitudes. The desirable next step would be to re-do the entire analysis based on model *A* presented in Tab. 5.1, in order to compare the results of the two and see if more sense can be made out of the derived magnitudes.

Relating to this, the binary pairing presented here of a WD with a RL-filling, low-mass M2 V companion along with a very short orbital period of ∼ 3 hrs means that PN G033.8+01.5 could be a cataclysmic variable (CV) candidate, or 'pre-CV' on the edge of the so-called 'period gap' (see, for example, Hellier 2001). In a CV scenario, the presence of the WD is usually obscured in the optical and UV by its bright accretion

disc, becoming detectable during periods of quiescence when the disc is smaller and less luminous (Hilditch 2001). The WD sustains a slow, yet continuous, mass accretion that also serves to increase $T_{\rm eff}$, affect the chemical abundance, and supplement angular momentum to the stellar envelope. This slow accretion rate is periodically punctuated every few weeks to months by a more intense accreting period that results in an outburst of gravitational potential energy lasting over a timescale of days to weeks – a dwarf nova. Every few thousand years, a more violent ejection occurs as accreted hydrogen undergoes thermally-unstable fusion on the surface of the WD (Sion 1999). If PN G033.8+01.5 can indeed be classified as a pre-CV candidate, then this also implies a stronger case for model *A* from Tab. 5.1 also being viable, with the WD appearing to fill its RL due to the surrounding accretion disc.

Conversely, a WD of mass 0.23 $M_{\odot}$, as derived here, would in itself imply that we are observing a helium (He) WD and *not* a CSPN. He WDs are formed when the hydrogen envelope is stripped away from the star before helium ignition commences, and such a process can occur through mass transfer within a binary system. However, the detection of such low-mass WDs (< 0.3 $M_{\odot}$) is extremely rare and would by definition mean that we are also not observing a CV as generally a higher mass WD is required (however, there is a good chance that this is due to selection effects; Ritter & Burkert 1986). This truly makes PN G033.8+01.5 an interesting object!

The filamentary / wispy structures seen in the imagery of PN G033.8+01.5 may be indicative of the presence of high velocity outflows, which are potentially features created as a result of mass transfer in a binary system (Jones et al. 2014, in press; Miszalski, Boffin & Corradi 2013; Tocknell, De Marco & Wardle 2013). Although the distance and estimated age of PN G033.8+01.5 fall within typical ranges for PNe, one cannot assume that it is indeed a true PN and not, for example, a nova shell without further investigation. Similarly to above, we can estimate an age for the nebula by assuming expansion velocities typical of a nova rather than a PN. Typical expansion velocities lie between $\sim$ 300–3000 km s^{-1}, which would result in an age of order 40–400 yrs.

It is important to acquire high resolution longslit spectra of the nebula using a similar method utilised with HaTr 4 (see Ch. 3) and LoTr 1 (see Ch. 4) in order to gain a more definitive value for the expansion velocity of the nebulous material, which in turn affects the inferred age of the PN. It would also be possible to examine the emission and absorption lines from such spectra to see if it possesses the features more typical of a PN or a nova remnant. Similarly, the stars themselves require detailed spectra in order to more accurately determine if it is a CV system or not. Currently, only two novae have been found *within* a PN – GK Per (Bode et al. 1987) and V 458 Vul (Wesson et al. 2008). If PN G033.8+01.5 does contain a nova, it would imply that it is undergoing its first outburst as any prior eruptions would act to disperse the PN, else it would simply dissipate during the system's quiescent phase (Hounsell 2012). All in all, PN G033.8+01.5 appears to be a more interesting object than initially thought, and certainly warrants further and more detailed investigation in order to ascertain its true nature.

Notes

[1]The VLT-FORS2 imagery of PN G033.8+01.5 presented in Fig. 5.3 was acquired through the POPI-PlaN project, under ESO programme ID 089.D-0357(A). Photometry of PN G033.8+01.5 from NTT-EFOSC2 was acquired by H.M.J. Boffin and D. Jones under ESO programme ID 091.D-0475(A). The IRAF/IDL code used to perform the stellar photometry (under the name) was provided by O.A. Gonzaléz (private communication).

6

Conclusions

The work presented in this thesis has covered a range of PNe–binary systems; a close binary (HaTr 4), an intermediate period binary (LoTr 1) and a compact binary system (PN G033.8+01.5) were examined with the overall aim of investigating not only how such a central star system affects the formation and morphology of the surrounding PNe, but also what it means for the binary system itself in terms of mass transfer and envelope ejection.

6.1 Summary of results and future work

The main conclusions of each investigation are as follows:

6.1.1 HaTr 4

Presented in Ch. 3 is the first detailed spatio-kinematical analysis and modelling of the planetary nebula HaTr 4, one of few known to contain a post-CE central star system (P = 1.74 d). High spatial and spectral resolution spectroscopy of the [O] nebular line obtained with VLT-UVES were presented alongside deep narrowband Hα+[N] imagery obtained using EMMI-NTT, and together the two were used to derive the 3D

morphology of HaTr 4. The nebula is found to display an extended ovoid morphology in the north-south direction, and not east-west as inferred previously from the original imagery of Hartl & Tritton (1985) and Bond & Livio (1990). As a result, HaTr 4 is in fact *not* a bipolar nebula as initially thought, but appears that way due to inclination effects related to an enhanced equatorial region consistent with a toroidal waist - a feature believed to be typical amongst PNe with post-CE central stars. The nebular symmetry axis is found to lie perpendicular to the orbital plane of the central binary, concordant with the idea that the formation and evolution of HaTr 4 has been strongly influenced by its central binary star, and making it only the seventh close binary PN to have had this alignment observationally shown.

The spatio-kinematical modelling of HaTr 4 revealed fairly typical dynamical properties, with a kinematical age of order 13 550 yrs at a distance of 3 kpc and an equatorial expansion velocity of 13 ± 2 km s^{-1}. The systemic velocity was determined to be -94 ± 4 km s^{-1}, in good agreement with a previous study by Beaulieu, Dopita & Freeman (1999). The inclination of the system was constrained as $75° \pm 5°$ (in agreement with Bodman, Schaub & Hillwig 2012), and the equatorial radius was calculated to be approximately 0.18 pc. These values, as taken from the model, can be compared to those derived by studying the spectra by eye. In this case, the angular size of the nebula was determined to be 23 arcsec, and the physical diameter 0.16 pc. The kinematical age of HaTr 4 at a distance of 3 kpc was therefore estimated to be of order 12 044 yrs - all typical values for a PN.

The other six close binary PNe previously confirmed to show the predicted alignment between the orbital plane of the binary and the nebular symmetry axis are very morphologically different to HaTr 4, which emphasises the variety of mechanisms and influences, both internal and external to the system, that affect the process of the formation and shaping of PNe. An apparent common morphological feature amongst the seven PNe is some form of equatorial ring; future work could involve a deeper study into the exact formation process behind these equatorial rings, and determine why this feature in particular seems to be consistent for those objects that have ejected a CE.

6.1.2 LoTr 1

Using a combination of spectra obtained with VLT-FORS2, AAT-UCLES and NTT-EMMI, as well as SuperWASP photometry, the aim of the investigation presented in Ch. 4 was to show the binary nature of LoTr 1, look for signs of chemical pollution and determine the nebular kinematics, with the intention of relating the results to two other PNe known to possess binary central stars showing an over-abundance of Barium – Abell 70 and WeBo 1. The binarity of the central star of LoTr 1 is confirmed, consisting of a K1 III giant and a hot white dwarf of $T_{\rm eff} \sim 4500$ K and 120 000 K, respectively. The cool giant does not present any evidence of an enhancement of s-process elements but is shown to have a rotation period of 6.4 d, which is a possible sign of mass accretion. LoTr 1 also presents broad double-peaked Hα emission lines, whose origin is still unclear. The nebula of LoTr 1 consists of two slightly elongated shells of ages 17 000 and 35 000 yrs, respectively, and with different orientations. As such, LoTr 1 presents a very different nebular morphology than that of A70 and WeBo 1, which may be an indication of a difference in their mass transfer episodes.

As mentioned in 4.3.2, the fact that a star system such as LoTr 1 can on first glance appear so similar to A70 and WeBo 1, yet lack the predicted chemical pollution, allows us to infer the possibility that the mass was transferred at an earlier stage in the evolution of the primary, i.e. before the TP-AGB phase, and subsequently before the s-process elements are created and dredged up to the surface. This potentially means that the AGB evolution of the primary was cut short by this mass-transfer episode, and evidence of this should be detectable in the properties of the WD. Therefore, follow-up observations of the system would be advantageous in order to confirm this hypothesis. Determination of the orbital period of these systems is also crucial; it is, however, important to note that given the inclination of the LoTr 1 nebula (almost pole-on), any radial velocity variations of the central star system would be very difficult to detect,

particularly for the expected period of ∼1–3 yr. This would require stable instruments with very high spectral resolution.

Two other PNe can be observed as follow-up work to the observations presented in this chapter; further study of K1-6 and LoTr 5 would help to gain a better overall picture of the processes involved with an intermediate period binary system and its affect on the surrounding nebula. Spectroscopy of PN K1-6, with its bow-shocked morphology (Frew et al. 2011), would be advantageous, as it also shows evidence of possessing a G- or K- type giant and a very hot (sub-)WD binary pair. With the spectra, evidence for chemical enrichment can be searched for in a similar way to that employed with LoTr 1, and an orbital period and separation for the binary can also be derived.

LoTr 5 is also worthy of further investigation, as it too lacks an apparent ring-like morphology despite similarly possessing a rapidly rotating, G5 III-type, Ba-rich central star. As mentioned in Ch. 4, Montez et al. (2010) have carried out a study into the X-ray emission emanating from this system and concluded that it is most likely chromospheric in origin, implying the presence of a spun-up companion. This would seem to imply on first glance that it possesses more similarities to A70 and WeBo 1 than to LoTr 1, further emphasising the comparatively unique status of the LoTr 1 system.

6.1.3 PN G033.8+01.5

Presented in Ch. 5 is the first detailed analysis of PN G033.8+01.5, observed as part of the newly formed POPIPlaN project aiming to update the current MASH catalogue of Galactic PNe with deep, narrowband images acquired using FORS2 on the VLT. The binary nature of this PNe has been shown through *i*-band time-series photometry showing a variability period of 3.04 hr (0.1268 d) and a *B*, *V*, *R* and *I* magnitudes of the binary system as a whole of 21.52, 19.18, 17.23 and 17.65, respectively, as derived using observations of standard stars. Using the V-band observations, a distance to the PN of 525 pc was derived. From the imagery, an angular size of the PN of 51 ×

37 arcsec ± 4 arcsec was determined, meaning an absolute diameter of 0.13 pc. Using average values for PNe expansion velocities (20–40 km s^{-1}), an estimated range for the age of PN G033.8+01.5 at a distance of 525 pc stands at the order of 3180–6359 yrs.

It is safe to say that the results presented in Ch. 5 do not seem to fit into that expected of a PN in a classical sense. The inconsistent luminosities in the *B* and *I* band present a challenge to explain, as well as why the WD appears to be very faint in all four bands compared to the M V companion. One possible explanation is that the typical $(V - I)$ and $(B - I)$ indices taken from the literature are inaccurate (or at least possess a fairly large range of potential values) which would in turn have an effect on the other derived magnitudes. The obvious first step to carry on the investigation would be to re-do the entire analysis based on model *A* presented in Tab. 5.1, in order to compare the results of the two and see if it makes more sense to look at the results from a different perspective.

To build up a complete depiction of PN G033.8+01.5, high resolution spectra of the central star system and longslit spectroscopy of the surrounding PN is necessary in order to more accurately determine its morphology and intrinsic kinematics in a similar way to that employed in the studies of HaTr 4 and LoTr 1. A more definitive value for the expansion velocity of the nebulous material can be derived from such spectra, which in turn affects the distance to, and therefore the age of, the PN. The value of this velocity will also help to determine whether PN G033.8+01.5 is a true PN, or is indeed a form of CV (as the short orbital period of $\sim$ 3 hrs would seem to imply). Expansion velocities lie between $\sim$ 300–3000 km s^{-1} for a typical nova remnant, which would result in a detectable age of 40–400 yrs. It would also be possible to examine the emission and absorption lines from such spectra to see if it possesses the features more typical of a PN or a nova remnant which would help strengthen the case either way. If it appears that we are observing a nova *within* a PN, it would only be the third to be discovered as such, along with GK Per (Bode et al. 1987) and V 458 Vul (Wesson et al. 2008).

The 3D morphology of PN G033.8+01.5 can determined from longslit spectra,

again in a similar way to that utilised with HaTr 4, in order to more clearly define what the overall structure is and how this may relate to the central binary system. In particular, it would be interesting to gain spectra of the wispy/filamentary components seen in the imagery to determine what the nature of the emission is - whether it is indeed indicative of a high velocity outflow, or whether the nebula has somehow become disrupted and is undergoing strong ionisation from the central binary.

On top of this, a WD of mass 0.23 $M_{\odot}$ implies that we are dealing with an He WD and therefore *not* a CSPN. Such objects be formed through mass transfer within a binary system, but the detection of such low-mass WDs ($< 0.3\,M_{\odot}$) is extremely rare and would by definition mean that the system is neither a true PN nor a CV. Therefore, deeper follow-up work to that presented in this thesis crucial, in order to more accurately determine the true nature of PN G033.8+01.5.

As a whole, the POPIPlaN project is still very much in its infancy. Should similar studies be carried out on each of the objects observed for the project, it would pave the way for a definitive Galactic PNe catalogue.

6.2 Final comments

It can be argued that the work presented in this thesis has perhaps opened up more questions than it has answered! The results from all three studies ended up being counter to that expected upon first glance, and are all exceedingly interesting for their own reasons: HaTr 4 has helped to solidify the idea that the binary is directly responsible for axisymmetric morphologies in close binary systems, the result from the study of LoTr 1 has served to highlight the large gap in knowledge about intermediate period binary systems to date, and the nature of PN G033.8+01.5 appears to be more complex than initially thought. The effect that these central binary systems have both on each other and the surrounding PN appear to be highly sensitive to the intrinsic stellar parameters, which naturally makes every case truly unique.

References

Acker A., Jasniewicz G., 1990, A&A, 238, 325

Acker A., Stenholm B., 1990, A&A, 223, 21

Afšar M., Bond H. E., 2005, MEMSAI, 76, 608

Appenzeller I. et al., 1998, The Messenger, 94, 1

Bagnulo S., Jehin E., Ledoux C., Cabanac R., Melo C., Gilmozzi R., ESO Paranal Science Operations Team, 2003, The Messenger, 114, 10

Balick B., 1987, AJ, 94, 671

Balick B., Frank A., 2002, ARA&A, 40, 439

Balick B., Rugers M., Terzian Y., Chengalur J. N., 1993, ApJ, 411, 778

Beaulieu S. F., Dopita M. A., Freeman K. C., 1999, ApJ, 515, 610

Bessel F. W., 1844, MNRAS, 6, 136

Bica E., 1994, A&A, 285, 868

Bica E., Claria J. J., Bonatto C., Piatti A. E., Ortolani S., Barbuy B., 1995, A&A, 303, 747

Bidelman W. P., Keenan P. C., 1951, ApJ, 114, 473

Blackman E. G., Frank A., Markiel J. A., Thomas J. H., Van Horn H. M., 2001, Nature, 409, 485

Blocker T., Schonberner D., 1996, in Astronomical Society of the Pacific Conference Series, Vol. 96, Hydrogen Deficient Stars, Jeffery C. S., Heber U., eds., p. 341

Bloecker T., 1995, A&A, 299, 755

Bode M. F., Roberts J. A., Whittet D. C. B., Seaquist E. R., Frail D. A., 1987, Nature, 329, 519

Bodman E. H. L., Schaub S. C., Hillwig T., 2012, JSARA, 5, 91

Boffin H. M. J. et al., 2012a, The Messenger, 148, 25

Boffin H. M. J., Jorissen A., 1988, A&A, 205, 155

Boffin H. M. J., Miszalski B., Rauch T., Jones D., Corradi R. L. M., Napiwotzki R., Day-Jones A. C., Köppen J., 2012b, Science, 338, 773

Boffin H. M. J., Zacs L., 1994, A&A, 291, 811

Bojičić I. S., Parker Q. A., Filipović M. D., Frew D. J., 2011, MNRAS, 412, 223

Bond H. E., 1985, in Astrophysics and Space Science Library, Vol. 113, Cataclysmic Variables and Low-Mass X-ray Binaries, Lamb D. Q., Patterson J., eds., pp. 15–27

Bond H. E., 2000, in Astronomical Society of the Pacific Conference Series, Vol. 199, Asymmetrical Planetary Nebulae II: From Origins to Microstructures, Kastner J. H., Soker N., Rappaport S., eds., p. 115

Bond H. E., Ciardullo R., Meakes M., 1989, Bull. Am. Astron. Soc., 21, 789

Bond H. E., Ciardullo R., Meakes M. G., 1993, in IAU Symposium, Vol. 155, Planetary Nebulae, Weinberger R., Acker A., eds., p. 397

Bond H. E., Liller W., Mannery E. J., 1978, ApJ, 223, 252

Bond H. E., Livio M., 1990, ApJ, 335, 568

Bond H. E., O'Brien M. S., Sion E. M., Mullan D. J., Exter K., Pollacco D. L., Webbink R. F., 2002, in Astronomical Society of the Pacific Conference Series, Vol. 279, Exotic Stars as Challenges to Evolution, Tout C. A., van Hamme W., eds., p. 239

Bond H. E., Pollacco D. L., Webbink R. F., 2003, AJ, 125, 260

Bowen I. S., 1928, ApJ, 67, 1

Burmeister M., Leedjärv L., 2009, A&A, 504, 171

Butters O. W. et al., 2010, A&A, 520

Calvet N., Peimbert M., 1983, RMXAA, 5, 319

Castelli F., Kurucz R. L., 2003, in IAU Symposium, Vol. 210, Modelling of Stellar Atmospheres, Piskunov N., Weiss W. W., Gray D. F., eds., p. 20P

Chu Y. H., Jacoby G. H., Arendt R., 1987, ApJS, 64, 529

Ciardullo R., Bond H. E., Sipior M. S., Fullton L. K., Zhang C.-Y., Schaefer K. G., 1999, ApJ, 118, 488

Corradi R. L. M., Gonçalves D. R., Villaver E., Mampaso A., Perinotto M., Schwarz H. E., Zanin C., 2000, ApJ, 535, 823

Corradi R. L. M. et al., 2011, MNRAS, 410, 1349

Corradi R. L. M., Sánchez-Blázquez P., Mellema G., Giammanco C., Schwarz H. E., 2004, A&A, 417, 637

Corradi R. L. M., Schönberner D., Steffen M., Perinotto M., 2003, MNRAS, 340, 417

Cox A. N., 2000, Allen's astrophysical quantities. New York: AIP Press; Springer

De Marco O., 2006, in IAU Symposium, Vol. 234, Planetary Nebulae in our Galaxy and Beyond, Barlow M. J., Méndez R. H., eds., pp. 111–118

De Marco O., 2009, PASP, 121, 316

De Marco O., Bond H. E., Harmer D., Fleming A. J., 2004, ApJ, 602, 93

De Marco O., Hillwig T. C., Smith A. J., 2008, AJ, 136, 323

De Marco O., Passy J.-C., Frew D. J., Moe M., Jacoby G. H., 2013, MNRAS, 428, 2118

Dekker H., Delabre B., Dodorico S., 1986, in Society of Photo-Optical Instrumentation Engineers (SPIE) Conference Series, Vol. 627, Society of Photo-Optical Instrumentation Engineers (SPIE) Conference Series, Crawford D. L., ed., pp. 339–348

Dekker H., D'Odorico S., Kaufer A., Delabre B., Kotzlowski H., 2000, in Society of Photo-Optical Instrumentation Engineers (SPIE) Conference Series, Vol. 4008, Society of Photo-Optical Instrumentation Engineers (SPIE) Conference Series, M. Iye & A. F. Moorwood, ed., pp. 534–545

Douchin D., De Marco O., Jacoby G. H., Hillwig T. C., Frew D. J., Bojičić I., Jasniewicz G., Parker Q. A., 2013, Central European Astrophysical Bulletin, 37, 391

Drew J. E. et al., 2005, MNRAS, 362, 753

Drilling J. S., 1985, ApJL, 294, L107

Ducati J. R., Bevilacqua C. M., Rembold S. B., Ribeiro D., 2001, ApJ, 558, 309

Duquennoy A., Mayor M., 1991, in Lecture Notes in Physics, Berlin Springer Verlag, Vol. 390, Bioastronomy: The Search for Extraterrestial Life – The Exploration Broadens, Heidmann J., Klein M. J., eds., pp. 39–43

Eggleton P. P., 1983, ApJ, 268, 368

Etoka S., Diamond P., 2004, MNRAS, 348, 34

Exter K. M., Pollacco D., Bell S. A., 2003, MNRAS, 341, 1349

Exter K. M., Pollacco D. L., Maxted P. F. L., Napiwotzki R., Bell S. A., 2005, MNRAS, 359, 315

Faulkner D. J., 1970, ApJ, 162, 513

Ferguson D. H., Liebert J., Haas S., Napiwotzki R., James T. A., 1999, ApJ, 518, 866

Finzi A., Wolf R. A., 1971, A&A, 11, 418

Frank A., Balick B., Icke V., Mellema G., 1993, ApJL, 404, L25

Frew D. J., 2008, PhD thesis, Department of Physics, Macquarie University, NSW 2109, Australia

Frew D. J., Parker Q. A., 2007, in Asymmetrical Planetary Nebulae IV

Frew D. J., Parker Q. A., 2010, PASA, 27, 129

Frew D. J. et al., 2011, PASA, 28, 83

Friend D. B., Abbott D. C., 1986, ApJ, 311, 701

García-Díaz M. T., Clark D. M., López J. A., Steffen W., Richer M. G., 2009, ApJ, 699, 1633

García-Segura G., López J. A., Franco J., 2001, ApJ, 560, 928

Gonçalves D. R., Corradi R. L. M., Mampaso A., 2001, ApJ, 547, 302

Graham M. F., Meaburn J., López J. A., Harman D. J., Holloway A. J., 2004, MNRAS, 347, 1370

Grauer A. D., Bond H. E., 1983, ApJ, 271, 259

Grauer A. D., Bond H. E., Ciardullo R., Fleming T. A., 1987, Bull. Am. Astron. Soc., 19, 643

Griffin R. F., 2006, The Observatory, 126, 1

Guerrero M. A., Miranda L. F., 2012, A&A, 539, A47

Habing H. J., 1996, AAPR, 7, 97

Hajduk M., Zijlstra A. A., Gesicki K., 2010, MNRAS, 406, 626

Harris H. C. et al., 2007, ApJ, 133, 631

Hartl H., Tritton S. B., 1985, A&A, 145, 41

Hellier C., 2001, Cataclysmic Variable Stars-how and why they vary. Springer

Herschel W., 1791, Royal Society of London Philosophical Transactions Series I, 81, 71

Herschel W., 1802, Royal Society of London Philosophical Transactions Series I, 92, 477

Herschel W., 1803, Philosophical Transactions of the Royal Society of London, 93, 339

Hilditch R. W., 2001, An Introduction to Close Binary Stars. Cambridge University Press

Hillwig T. C., 2004, in Astronomical Society of the Pacific Conference Series, Vol.

313, Asymmetrical Planetary Nebulae III: Winds, Structure and the Thunderbird, Meixner M., Kastner J. H., Balick B., Soker N., eds., pp. 529–+

Hillwig T. C., Bond H. E., Afşar M., De Marco O., 2010, AJ, 140, 319

Hodgkin S. T., Jameson R. F., Steele I. A., 1995, MNRAS, 274, 869

Horne K., 1986, PASP, 98, 609

Hounsell R., 2012, PhD thesis, Liverpool John Moores University

Howarth I. D., Heber U., 1990, PASP, 102, 912

Howell S. B., 2006, Handbook of CCD Astronomy. Cambridge University Press, ISBN 0-521-61762-6

Huckvale L. et al., 2013, MNRAS

Huggins W., Miller W. A., 1864, Royal Society of London Philosophical Transactions Series I, 154, 437

Iben I., Livio M., 1993, PASP, 105, 1373

Icke V., 1988, A&A, 202, 177

Ireland M. J., Kraus A., Martinache F., Lloyd J. P., Tuthill P. G., 2008, ApJ, 678, 463

Jacoby G. H. et al., 2010, PASP, 27, 156

Jasniewicz G., Acker A., Freire Ferrero R., Burnet M., 1992, A&A, 261, 314

Jasniewicz G., Acker A., Mauron N., Duquennoy A., Cuypers J., 1994, A&A, 286, 211

Jasniewicz G., Thevenin F., Monier R., Skiff B. A., 1996, A&A, 307, 200

Jeffries R. D., Stevens I. R., 1996, MNRAS, 279, 180

Joardar S., Bhattacharya A. B., Bhattacharya R., 2008, Astronomy & Astrophysics W/CD (R). Jones & Bartlett Learning

Jones D., Boffin H. M. J., Miszalski B., Wesson R., Corradi R. L. M., Tyndall A. A., 2014, A&A, 562, A89

Jones D., Lloyd M., Mitchell D. L., Pollacco D. L., O'Brien T. J., Vaytet N. M. H., 2010a, MNRAS, 401, 405

Jones D. et al., 2010b, MNRAS, 408, 2312

Jones D., Mitchell D. L., Lloyd M., Pollacco D., O'Brien T. J., Meaburn J., Vaytet N. M. H., 2012a, MNRAS, 420, 2271

Jones D., Pollacco D., Faedi F., Lloyd M., 2011a, in Asymmetric Planetary Nebulae 5

Conference, p. 111P

Jones D., Tyndall A., Huckvale L., Prouse B., Lloyd M., 2011b, Evolution of Compact Binaries. Astron. Soc. Pac., San Fran., 447, 165

Jones D., Tyndall A. A., Lloyd M., Santander-García M., 2012b, in IAU Symposium, Vol. 283, IAU Symposium, pp. 402–403

Jordan S., Werner K., O'Toole S. J., 2005, A&A, 432, 273

Jorissen A., Boffin H. M. J., 1992, in Binaries as Tracers of Star Formation, Duquennoy A., Mayor M., eds., pp. 110–131

Kahn F. D., West K. A., 1985a, MNRAS, 212, 837

Kahn F. D., West K. A., 1985b, MNRAS, 212, 837

Kaltenegger L., Traub W., 2009, ApJ, 698, 519

Kilkenny D., Spencer Jones J. H., Marang F., 1988, The Observatory, 108, 88

Kohoutek L., Schnur G. F. O., 1982, MNRAS, 201, 21

Kutter G. S., Sparks W. M., 1974, ApJ, 192, 447

Kwok S., 2002, in Astronomical Society of the Pacific Conference Series, Vol. 260, Interacting Winds from Massive Stars, Moffat A. F. J., St-Louis N., eds., p. 245

Kwok S., 2010, Publications of Astron. Soc. of Australia, 27, 174

Kwok S., Hrivnak B. J., Zhang C. Y., Langill P. L., 1996, ApJ, 472, 287

Kwok S., Purton C. R., Fitzgerald P. M., 1978, ApJ, 219, 125

Latter W. B., Hora J. L., Kelly D. M., Deutsch L. K., Maloney P. R., 1993, ApJ, 106, 260

Liebert J., Tweedy R. W., Napiwotzki R., Fulbright M. S., 1995, ApJ, 441, 424

Liebert J., Young P. A., Arnett D., Holberg J. B., Williams K. A., 2005, APJL, 630, L69

Little S. J., Little-Marenin I. R., Bauer W. H., 1987, ApJ, 94, 981

Lloyd J. P., Martinache F., Ireland M. J., Monnier J. D., Pravdo S. H., Shaklan S. B., Tuthill P. G., 2006, ApJL, 650, L131

Longmore A. J., Tritton S. B., 1980, MNRAS, 193, 521

López J. A., Richer M. G., García-Díaz M. T., Clark D. M., Meaburn J., Riesgo H., Steffen W., Lloyd M., 2012, RMxAA, 48, 3

Lucy L. B., 1967, AJ, 72, 813

Lutz J., Fraser O., McKeever J., Tugaga D., 2010, PASP, 122, 524

Machida M. N., Tomisaka K., Matsumoto T., Inutsuka S.-i., 2008, ApJ, 677, 327

Massey P., DeVeny J., Jannuzi B., Carder E., 2000, Low-to-Moderate Resolution Optical Spectroscopy Manual for Kitt Peak. Kitt Peak Observatory

Massey P., Hanson M. M., 2013, Astronomical Spectroscopy, Springer Science+Business Media Dordrecht, p. 35

Mastrodemos N., Morris M., 1999, ApJ, 523, 357

McClure R. D., 1983, ApJ, 268, 264

McClure R. D., Woodsworth A. W., 1990, ApJ, 352, 709

Meaburn J., López J. A., Gutiérrez L., Quiróz F., Murillo J. M., Valdéz J., Pedrayez M., 2003, Revista Mexicana de Astronomia y Astrofisica, 39, 185

Meaburn J., Walsh J. R., Clegg R. E. S., Walton N. A., Taylor D., Berry D. S., 1992, MNRAS, 255, 177

Meatheringham S. J., Wood P. R., Faulkner D. J., 1988, ApJ, 334, 862

Mellema G., Frank A., 1995, MNRAS, 273, 401

Melnick J., Mendes de Oliveira C., 1995, EFOSC2 Operating Manual. ESO

Méndez R. H., Kudritzki R. P., Herrero A., Husfeld D., Groth H. G., 1988, A&A, 190, 113

Méndez R. H., Niemela V. S., 1981, ApJ, 250, 240

Michell J., 1767, Philosophical Transactions (1683-1775), 57, 234

Miszalski B., Acker A., Moffat A. F. J., Parker Q. A., Udalski A., 2008a, A&A, 488, L79

Miszalski B., Acker A., Moffat A. F. J., Parker Q. A., Udalski A., 2009a, A&A, 496, 813

Miszalski B., Acker A., Parker Q. A., Moffat A. F. J., 2009b, A&A, 505, 249

Miszalski B., Boffin H. M. J., Corradi R. L. M., 2013, MNRAS, 428, L39

Miszalski B., Boffin H. M. J., Frew D. J., Acker A., Köppen J., Moffat A. F. J., Parker Q. A., 2012, MNRAS, 419, 39

Miszalski B. et al., 2013, MNRAS

Miszalski B., Corradi R. L. M., Boffin H. M. J., Jones D., Sabin L., Santander-García M., Rodríguez-Gil P., Rubio-Díez M. M., 2011a, MNRAS, 413, 1264

Miszalski B., Corradi R. L. M., Jones D., Santander-García M., Rodríguez-Gil P., Rubio-Díez M. M., 2011b, in Asymmetric Planetary Nebulae 5 Conference

Miszalski B., Jones D., Rodríguez-Gil P., Boffin H. M. J., Corradi R. L. M., Santander-García M., 2011c, A&A, 531, A158

Miszalski B., Parker Q. A., Acker A., Birkby J. L., Frew D. J., Kovacevic A., 2008b, MNRAS, 384, 525

Mitchell D. L., Pollacco D., O'Brien T. J., Bryce M., López J. A., Meaburn J., Vaytet N. M. H., 2007, MNRAS, 374, 1404

Moe M., De Marco O., 2006, ApJ, 650, 916

Montez J. R., De Marco O., Kastner J. H., Chu Y.-H., 2010, ApJ, 721, 1820

Nordhaus J., Blackman E. G., 2006, MNRAS, 370, 2004

Osterbrock D. E., 1989, Astrophysics of gaseous nebulae and active galactic nuclei. University Science Books

Paczyński B., 1971, Astrophysics Letters, 9, 33

Palmer C., Loewen E. G., Thermo R., 1994, Diffraction Grating Handbook. Milton Roy

Parker Q. A. et al., 2006, MNRAS, 373, 79

Parker Q. A., Acker A., Peyaud A., Frew D. J., MASH Consortium, 2005, in American Institute of Physics Conference Series, Vol. 804, Planetary Nebulae as Astronomical Tools, Szczerba R., Stasińska G., Gorny S. K., eds., pp. 3–6

Pijpers F. P., Hearn A. G., 1989, A&A, 209, 198

Pilachowski C. A., 1977, A&A, 54, 465

Poe C. H., Friend D. B., 1986, ApJ, 311, 317

Pollacco D., Bell S. A., 1993, MNRAS, 262, 377

Pollacco D., Bell S. A., 1994, MNRAS, 267, 452

Pollacco D. L. et al., 2006, PASP, 118, 1407

Pravdo S. H., Shaklan S. B., Lloyd J., 2005, ApJ, 630, 528

Raghavan D. et al., 2010, ApJS, 190, 1

Reed B. C., 1998, JRASC, 92, 36

Ritter H., Burkert A., 1986, AAP, 158, 161

Rodríguez-Gil P. et al., 2010, MNRAS, 407, L21

Roxburgh I. W., 1967, Nature, 215, 838

Russell H. N., Dugan R. S., Stewart J., 1927, Ginn & Co., Boston, 909

Ryan S. G., Fish A. C., 1995, The UCL Coude Echelle Spectrographs. Anglo-Australian Observatory

Sahai R., 2009, in Astronomy, Vol. 2010, astro2010: The Astronomy and Astrophysics Decadal Survey, p. 256

Salaris M., Cassisi S., 2005, Evolution of Stars and Stellar Populations. John Wiley & Sons, Ltd

Santander-Garcia M., Rodríguez-Gil P., Jones D., Corradi R. L. M., Miszalski B., Pyrzas S., Rubio-Díez M. M., 2011, in Asymmetric Planetary Nebulae 5 Conference

Schild H., Muerset U., Schmutz W., 1996, A&A, 306, 477

Schlegel D. J., Finkbeiner D. P., Davis M., 1998, ApJ, 500, 525

Schönberner D., Steffen M., Stahlberg J., Kifonidis K., Blöcker T., 1997, in Stellar Ecology: Advances in Stellar Evolution„ Rood R. T., Renzini A., eds., pp. 146–153

Shimansky V. V., Pozdnyakova S. A., Borisov N. V., Bikmaev I. F., Vlasyuk V. V., Spiridonova O. I., Galeev A. I., Mel'Nikov S. S., 2009, Astrophysical Bulletin, 64, 349

Shipman H. L., 1979, ApJ, 228, 240

Siegel M. H., Hoversten E., Bond H. E., Stark M., Breeveld A. A., 2012, AJ, 144, 65

Simis Y. J. W., Icke V., Dominik C., 2001, A&A, 371, 205

Sion E. M., 1999, PASP, 111, 532

Skrutskie M. F. et al., 2006, AJ, 131, 1163

Smith N., Bally J., Walawender J., 2007, AJ, 134, 846

Smith R. L., Rose W. K., 1972, ApJ, 176, 395

Smith V. V., Lambert D. L., 1988, ApJ, 333, 219

Soker N., 1996, ApJ, 468, 774

Soker N., 1997, ApJS, 112, 487

Soker N., 2004, in Astronomical Society of the Pacific Conference Series, Vol. 313, Asymmetrical Planetary Nebulae III: Winds, Structure and the Thunderbird, Meixner M., Kastner J. H., Balick B., Soker N., eds., p. 562

Soker N., 2006, PASP, 118, 260

Soker N., Livio M., 1994, ApJ, 421, 219

Soker N., Rappaport S., 2000, ApJ, 538, 241

Soker N., Regev O., 1998, AJ, 116, 2462

Steffen W., Koning N., Wenger S., Morisset C., Magnor M., 2011, IEEE Transactions on Visualization and Computer Graphics, 17, 454

Steffen W., López J. A., 2006, Revista Mexicana de Astronomia y Astrofisica, 42, 99

Strassmeier K. G., Hubl B., Rice J. B., 1997, A&A, 322, 511

Tajitsu A., Tamura S., Yadoumaru Y., Weinberger R., Köppen J., 1999, PASP, 111, 1157

Tatum J. B., 2008, Celestial Mechanics. Online book

Tatum J. B., 2011, Stellar Atmospheres. Online book

Theuns T., Boffin H. M. J., Jorissen A., 1996, MNRAS, 280, 1264

Thevenin F., Jasniewicz G., 1997, A&A, 320, 913

Tocknell J., De Marco O., Wardle M., 2013, ArXiv e-prints

Torres G., 2010, AJ, 140, 1158

Tovmassian G. et al., 2010, ApJ, 714, 178

Tovmassian G. H., Napiwotzki R., Richer M. G., Stasińska G., Fullerton A. W., Rauch T., 2004, ApJ, 616, 485

Trimble V., Sackmann I.-J., 1978, MNRAS, 182, 97

Tuchman Y., Sack N., Barkat Z., 1979, ApJ, 234, 217

Tylenda R., Siódmiak N., Górny S. K., Corradi R. L. M., Schwarz H. E., 2003, A&A, 405, 627

Tyndall A. A. et al., 2013, MNRAS, 436, 2082

Tyndall A. A., Jones D., Lloyd M., O'Brien T. J., Pollacco D., 2012, MNRAS, 422, 1804

van Albada-van Dien E., 1977, A&AS, 29, 305

Van Horn H. M., Thomas J. H., Frank A., Blackman E. G., 2003, ApJ, 585, 983

van Winckel H., Lloyd Evans T., Briquet M., De Cat P., Degroote P., De Meester W., De Ridder J., et al. et al., 2009, A&A, 505, 1221

Vorontsov S., 2010, Stellar Structure and Evolution. Queen Mary, University of Lon-

don

Wagner R. M., 1992, in Astronomical Society of the Pacific Conference Series, Vol. 23, Astronomical CCD Observing and Reduction Techniques, Howell S. B., ed., p. 160

Walsh, J. R. and Walton, N. A., 1996, A&A, 315, 253

Wareing C. J., Zijlstra A. A., O'Brien T. J., 2007, MNRAS, 382, 1233

Weinberger R., 1989, A&A, 78, 301

Wesson R. et al., 2008, ApJ, 688, L21

Wing R., 1983, in Astrophysics and Space Science Library, Vol. 102, Activity in Red-Dwarf Stars, Byrne P., Rodonò M., eds., Springer Netherlands, pp. 35–38

Woitke P., 2006, A&A, 460, L9

Wood J. H., Robinson E. L., Zhang E. H., 1995, MNRAS, 277, 87

Wood P. R., 1974, ApJ, 190, 609

Yungelson L. R., Tutukov A. V., Livio M., 1993, ApJ, 418, 794

Zhang C. Y., Kwok S., 1998, ApJS, 117, 341

Ziegler M., Rauch T., Werner K., Koeppen J., Kruk J. W., 2012, A&A

Zijlstra A. A., 2007, Baltic Astronomy, 16, 79

Zijlstra A. A., Bedding T. R., Mattei J. A., 2002, MNRAS, 334, 498

Zuckerman B., Gatley I., 1988, ApJ, 324, 501